공학박사 학위논문

kinetic Monte Carlo (kMC) Simulation of Charged Nanoparticles and Thin Film Microstructure Based on Electrostatic Energy Calculation

정전기적 에너지 계산 기반의 하전된 나노입자와 박막 미세구조 키네틱 몬테 카를로 시뮬레이션

2023년 02월

서울대학교 대학원

재료공학부

변 민 교

kinetic Monte Carlo (kMC) Simulation of Charged Nanoparticles and Thin Film Microstructure Based on Electrostatic Energy Calculation

지도 교수 황 농 문

이 논문을 공학박사 학위논문으로 제출함
2023년 02월

서울대학교 대학원
재료공학부
변 민 교

변민교의 공학박사 학위논문을 인준함
2023년 01월

위 원 장 김 미 영 (인)

부위원장 황 농 문 (인)

위 원 한 승 우 (인)

위 원 유 병 덕 (인)

위 원 김 근 수 (인)

Abstract

kinetic Monte Carlo (kMC) Simulation of Charged Nanoparticles and Thin Film Microstructure Based on Electrostatic Energy Calculation

Mingyo Byeon

Department of Materials Science and Engineering

The Graduate School

Seoul National University

To study the dynamics of non-classical crystallization system comprising charged nanoparticles (CNPs), the electrostatic potential energy between CNPs was calculated and kinetic Monte Carlo (kMC) simulations were performed based on the calculated electrostatic potential energy. For the calculation of the potential energy, both numerical and analytical calculation methods were used for comparison and as occasion demands. The numerical method is finite element method (FEM) and the analytical calculation is performed using the capacitance coefficients of conductor systems.

Firstly, the evolution of a particle depletion zone around the large CNP during the low-temperature chemical vapor deposition (CVD) of Si was investigated. The calculation results showed that small and large CNPs having like charges attracted each other when they were in close proximity, because opposite charges were induced on the surfaces of particles adjacent to each other. The kMC simulation results showed that this attraction resulted in a relatively small particle depletion zone around the large CNP. During the formation of the depletion zone, charges accumulated on the large CNP. The accumulated charge resulted in repulsion between the small and large CNPs, and a gradual expansion of the particle depletion zone. Further analysis indicated that the imbalance between the numbers of positively and negatively charged CNPs influenced the structural evolution of the particle depletion zone.

Secondly, abnormal coarsening phenomenon of Si particles during CVD of Si were numerically studied through the simulation as another peculiar microstructure. The kMC simulation results showed that the abnormal growth occurred by electrostatic attraction with both positively and negatively CNPs under the condition that the charge signs of CNPs are balanced. During the growth of the deposited CNPs, sufficient CNP density in the gas phase was also found to be an important factor for the abnormal growth of deposited

CNPs. Further analysis indicated that gas flow velocity influenced the growth of deposited CNPs. Fast gas flow velocity caused abnormal growth even in the slightly unbalanced charge signs of CNPs.

Thirdly, the growth behaviors and rates of deposited CNPs were investigated through the simulation by varying the electrical property of the substrates: grounded conductor, floating conductor and insulator. When the CNPs are balanced, the results showed that the growth rates were accelerated when the substrate is floating conductor or insulator compared to the grounded conductor. When the CNPs are imbalanced, the long-term growth rate on the grounded substrate was the fastest. On the floating conductor and the insulator substrate, the growth was restricted by charge accumulation after a certain period of time where growth proceeded. Especially, in the particle etching conditions, the deposited CNPs did not grow but were etched away by repelling with the CNPs in the gas phase after charge accumulation.

Finally, the electrostatic potential energy was calculated for the CNP-charged nanowire systems and how it affected to the anisotropic growth of the charged nanowires under the CNP-existing system was investigated using FEM. The calculation results showed that the electrostatic interaction favors the anisotropic growth when the CNP in the gas phase and deposited

charged nanowire have like-charge: CNPs approaching in the tip direction have weaker repulsive interaction than those approaching in the side direction. Comparing the energy barrier difference when CNP approaches to the charge nanowire in each direction, higher charge ratios of charged nanowire to CNP tend to favor anisotropic growth. In the case of the length of nanowires, there appears to be an appropriate length at which anisotropic growth is most favorable. For the anisotropic growth of the charged nanowires by electrostatic interaction, the charge sign of the CNPs should be imbalanced, which makes interactions between the charged nanowires and CNPs with the same sign mainly exist.

Overall, it was found that the most important factor in determining the microstructure in non-classical crystallization, in which CNPs in the gas phase are the growth unit of thin film deposition, is the CNP charge sign ratio.

Keyword : Non-classical crystallization, Charged nanoparticles, Electrostatic potential energy, kinetic Monte Carlo (kMC) simulation, Thin film, Chemical Vapor Deposition (CVD)

Student Number : 2017-23401

Table of Contents

List of Figures

Figure 3.8 FEM error (%) as a function of surface distance (s) for all combinations of $r = 5,\ 10\ \text{nm}$ and $Q = +10e,\ +50e$. The other parameters are $R = 250\ \text{nm}$ and $q = +e$.

Figure 4.1 Field-emission scanning electron microscopy images of Si microstructures after the 24 h chemical vapor deposition of charged Si nanoparticles on a glass substrate located in a low-temperature zone of 500℃. For the first 5 mins, an AC bias of ±50V at 1 Hz was applied to the glass substrate holder. The flow rates of He-diluted SiH_4 (10% SiH_4 - 90% He), H_2 and N_2 were 11, 50, and 300 sccm, respectively. (b) A higher-magnification image of (a); the scale bar is 100 nm.

Figure 4.2 (a) kMC simulation results: Snapshots and trajectories of three small particles interacting with a large particle of the same charge at three simulation times (τ_0). The centered black circle represents the large particle, while the green dots and black lines represent the positions of small unit particles and their trajectories at each simulation time, respectively. (b) Final discrimination of the three small particles after a kMC sweep. The red dot and blue cross represent the initial positions of small particles attracted and not attracted to the large particle, respectively. The dashed circle represents the domain boundary of the kMC simulation. The simulation parameters are $R = 250\ \text{nm},\ r = 10\ \text{nm},\ Q = +5e,\ q = +e$, and $T = 773\ \text{K}$, and the dimensions of each box are $1500\ \text{nm} \times 1500\ \text{nm}$.

Figure 4.3 kMC simulation results: Charge-dependent variation in the final discrimination results of 10^4 small particles interacting with a large particle of the same charge, for $Q =$ (a) $+e$, (b) $+50e$, and (c) $+100e$. The centered black circle represents the large particle; the red dot and blue cross represent the initial positions of small particles attracted and not attracted to the large particle, respectively; the inner dashed circle denotes the discrimination boundary between the small particles attracted and not attracted to the large particle; the numbers denote the thickness of the discrimination boundary (nm); and the outer dashed circle represents the domain boundary of kMC simulation. The simulation parameters are $R = 250\ \text{nm},\ q = +e,\ r = 10\ \text{nm}$, and $T = 773\ \text{K}$, and the dimensions of each box are $1500\ \text{nm} \times 1500\ \text{nm}$.

Figure 4.4 kMC simulation results: Snapshots of systems with small CNPs and a large CNP at different simulation times (τ_0). Positively

and negatively charged small particles coexist. Three values of γ_+were considered: (a) 0.5, (b) 0.7, and (c) 0.9. Five thousand small CNPs were randomly positioned in a square of $1500\ \text{nm} \times 1500\ \text{nm}$ and outside the large CNP without any overlap. The white circles represent the position and size of the CNPs. The initial parameters for the simulation are $Q_0 = +5e, q_0 = \pm 5e, R = 250\ \text{nm}$, $r_0 = 3\ \text{nm}$, and $T = 773\ \text{K}$, and the dimensions of each box are $2000\ \text{nm} \times 2000\ \text{nm}$.

Figure 4.5 Charge ratio ($Q/|q_0|$) as a function of t (τ_0), obtained from the kMC simulation results in Figure 4.4, for γ_+ = 0.5–0.9.

Figure 4.6 Particle size distributions in a higher−magnification image of Figure 4.1(a). In (a), the particle zones are divided into two parts (Part 1 and Part 2). In (b), the particle size distribution results are normalized to represent the probability.

Figure 5.1 Scanning electron microscopy (SEM) images of Si−deposited surfaces at three deposition times. $4 \times 4\ \mu\text{m}^2$ specimens of SiN_x (x = 0.56) are placed on an SiO_2 surface. The images show magnifications of one of the SiN_x specimens presented below. (a) At 480 s, many fine nanoparticles are selectively deposited on all SiN_x specimens. (b) At 720 s, very large nanoparticle is evident among the fine nanoparticles on a few SiN_x specimens. (c) At 960 s, most SiN_x specimens are covered with single large nanoparticles, although some lack nanoparticles.

Figure 5.2 kMC simulation results: Snapshots of systems with CNPs in the gas phase and deposited CNPs at different simulation times (τ_0). Three values of the charge sign ratio γ_+ were explored: (a) 0.5, (b) 0.6, and (c) 0.7. Blue and black spheres represent the positions and sizes of CNPs in the gas phase and deposited CNPs, respectively. The initial parameters for simulation were $r_0 = 20\ \text{nm}$, $q_0 = \pm e$, $\eta = 0.03$, $T = 1223\ \text{K}$, $k_{\text{etch}} = 0.05\ \text{nm}/\tau_0$, and $v_{\text{flow}} = 5\ \text{nm}/\tau_0$. The dimensions of each domain were $1000 \times 1000 \times 1000\ \text{nm}^3$.

Figure 5.3 (a) The radius R_{max} and (b) the charge Q_{max} of the largest deposited particle as a function of t (τ_0), as indicated by the kMC simulation results of Figure 5.2, for $\gamma_+ = 0.5 - 0.9$.

Figure 5.4 kMC simulation results: Snapshots of systems with CNPs in the gas phase and deposited CNPs at different simulation times (τ_0). Three values of the volume fraction η were explored: (a)

0.005, (b) 0.02, and (c) 0.03. The blue and black spheres represent the positions and sizes of CNPs in the gas phase and deposited CNPs, respectively. The initial parameters for simulation were $r_0 = 20\ \text{nm}$, $q_0 = \pm e$, $\gamma_+ = 0.5$, $T = 1223\ \text{K}$, $k_{\text{etch}} = 0.05\ \text{nm}/\tau_0$, and $v_{\text{flow}} = 5\ \text{nm}/\tau_0$. The dimensions of each domain were $1000 \times 1000 \times 1000\ \text{nm}^3$.

Figure 5.5 The radius R_{max} of the largest deposited particle as a function of t (τ_0), obtained from the kMC simulation results in Figure 5.4, for $\eta = 0.005 - 0.05$.

Figure 5.6 kMC simulation results: Snapshots of systems with CNPs in the gas phase and deposited CNPs at different simulation times (τ_0.). Three gas flow velocities v_{flow} were explored: (a) 0 (no flow), (b) 10, and (c) 15 nm/τ_0. The blue and black spheres represent the positions and sizes of CNPs in the gas phase and deposited CNPs, respectively. The initial parameters for simulation were $r_0 = 20\ \text{nm}$, $q_0 = \pm e$, $\gamma_+ = 0.6, \eta = 0.03$, $T = 1223\ \text{K}$, and $k_{\text{etch}} = 0.05\ \text{nm}/\tau_0$. The dimensions of each domain were $1000 \times 1000 \times 1000\ \text{nm}^3$.

Figure 5.7 The radius R_{max} of the largest deposited particle as a function of t (τ_0), obtained from the kMC simulation results in Figure 5.6, for $v_{\text{flow}} = 0 - 20\ \text{nm}/\tau_0$.

Figure 6.1 Time evolution of deposition behavior of Si on the (a) Mo and (b) SiO_2 substrate with the SiH_4 : HCl : H_2 gas ratio of 1 : 2 : 97 under a reactor pressure of 100 Torr at a substrate temperature of 950 ℃.

Figure 6.2 A schematic of system with a spherical CNP and substrate. The substrate is (a) grounded conductor (b) floating conductor. The green circle denotes a CNP in the gas phase with a radius r and a charge q. The blue rectangular parallelepiped and black circle denote the substrate and deposited CNP on the substrate, respectively.

Figure 6.3 W, excluding self-energy of CNP, divided by q^2 as a function of s for the CNP-grounded conductive substrate system. The radius of CNP r varies from 5 nm to 20 nm. For comparison, the value of W for point charge is also plotted.

Figure 6.4 W, excluding self-energy of CNP as a function of s for

the CNP−floating conductive substrate system ($r = 5\ \text{nm}, q = +e, s_0 = 100\ \text{nm}$). The surface charge density of the substrate σ varies from $-2 * 10^{-4} e/\text{nm}^2$ to $+2 * 10^{-4} e/\text{nm}^2$. For the positive σ, the values of transition separation distance s^* are expressed for each σ.

Figure 6.5 kMC simulation results: Snapshots of systems with CNPs in the gas phase and deposited CNPs at different simulation times (τ_0). Three types of the substrates were explored: (a) grounded conductor, (b) floating conductor, and (c) insulator. Red and black spheres represent the positions and sizes of CNPs in the gas phase and deposited CNPs, respectively. The initial parameters for simulation were $r_0 = 5\ \text{nm}$, $q_0 = \pm e$, $\gamma_+ = 0.5$, $\eta = 0.001$, $T = 773\ \text{K}$, $k_{\text{etch}} = 0\ \text{nm}/\tau_0$, and $v_{\text{flow}} = 5\ \text{nm}/\tau_0$. The dimensions of each displayed domain were $1000 \times 1000 \times 200\ \text{nm}^3$.

Figure 6.6 kMC simulation results: Snapshots of systems with CNPs in the gas phase and deposited CNPs at different simulation times (τ_0). Three types of the substrates were explored: (a) grounded conductor, (b) floating conductor, and (c) insulator. The simulation parameters are same with those of Figure 6.5 except for $\gamma_+ = 0.7$.

Figure 6.7 kMC simulation results: Snapshots of systems with CNPs in the gas phase and deposited CNPs at different simulation times (τ_0). Three types of the substrates were explored: (a) grounded conductor, (b) floating conductor, and (c) insulator. The simulation parameters are same with those of Figure 6.5 except for $\gamma_+ = 0.9$.

Figure 6.8 The film thickness d as a function of t (τ_0), as indicated by the kMC simulation results of (a) Figure 6.5 ($\gamma_+ = 0.5$), (b) Figure 6.6 ($\gamma_+ = 0.7$), and (c) Figure 6.7 ($\gamma_+ = 0.9$). The solid, dashed and dotted line denotes the thickness on the grounded conductor, floating conductor, and insulator substrate, respectively. (d) The surface charge density σ of the floating substrate for $\gamma_+ = 0.5 - 0.9$.

Figure 6.9 Etching rate of particle as a function of its radius r from Equation (51) using $\gamma = 1.23\ J/m^2$, $V_m = 1.206 \times 10^{-5}\ m^3/\text{mol}$ and $T = 773\ \text{K}$.

Figure 6.10 kMC simulation results: Snapshots of systems with CNPs in the gas phase and deposited CNPs at different simulation times (τ_0). Three types of the substrates were explored: (a)

grounded conductor, (b) floating conductor, and (c) insulator. Red and black spheres represent the positions and sizes of CNPs in the gas phase and deposited CNPs, respectively. The initial parameters for simulation were $r_0 = 5\,\mathrm{nm}$, $q_0 = \pm e$, $\gamma_+ = 0.5$, $\eta = 0.01$, $T = 773\,\mathrm{K}$, $k_{\mathrm{etch}}^{\mathrm{flat}} = 0.01\,\mathrm{nm}/\tau_0$, and $v_{\mathrm{flow}} = 5\,\mathrm{nm}/\tau_0$. The dimensions of each displayed domain were $1000 \times 1000 \times 200\,\mathrm{nm}^3$.

Figure 6.11 kMC simulation results: Snapshots of systems with CNPs in the gas phase and deposited CNPs at different simulation times (τ_0). Three types of the substrates were explored: (a) grounded conductor, (b) floating conductor, and (c) insulator. The simulation parameters are same with those of Figure 6.10 except for $\gamma_+ = 0.7$.

Figure 6.12 kMC simulation results: Snapshots of systems with CNPs in the gas phase and deposited CNPs at different simulation times (τ_0). Three types of the substrates were explored: (a) grounded conductor, (b) floating conductor, and (c) insulator. The simulation parameters are same with those of Figure 6.10 except for $\gamma_+ = 0.9$.

Figure 6.13 The film thickness d as a function of t (τ_0), as indicated by the kMC simulation results of (a) Figure 6.10 ($\gamma_+ = 0.5$), (b) Figure 6.11 ($\gamma_+ = 0.7$), and (c) Figure 6.12 ($\gamma_+ = 0.9$). The solid, dashed and dotted line denotes the thickness on the grounded conductor, floating conductor, and insulator substrate, respectively. (d) The surface charge density σ of the floating substrate for $\gamma_+ = 0.5 - 0.9$.

Figure 7.1 Microstructures evolution on (a) Mo, (b) Si, (c) SiO_2, (d) Si_3N_4 substrates after 3 min deposition under 10 Torr of reactor pressure and 950 ℃ of temperature substrate with a gas ratio of SiH_4 : HCl : H_2 = 3 : 1 : 96.

Figure 7.2 A system of a charged nanowire and a CNP. The separation distance s is varied in (a) the side direction and (b) the tip direction of the charged nanowire.

Figure 7.3 Contour of electrostatic potential energy W when the center of charged nanowire with $Q = +5e, N = 30, r = 10\,\mathrm{nm}$ is fixed at the origin. The color at each position means the W value of the system when the CNP with $q = +e, r = 10\,\mathrm{nm}$ is located there.

Figure 7.4 W, excluding self−energy, as a function of s in the side and tip directions for the charge nanowire and CNP system, with $r = 3\,\mathrm{nm},\ N = 10, Q = +5e,$ and (a) $q = +e$; (b) $q = -e$.

Figure 7.5 W, excluding self−energy, divided by q^2 as a function of s in the side (dashed lines) and tip (solid lines) directions for the charged nanowire and CNP system ($r = 3\,\mathrm{nm}$). (a) $N = 10,\ Q/q : 1 - 50$; (b) $Q/q = 5,\ N : 5 - 50$.

Figure 7.6 $(\Delta W_{\mathrm{side}} - \Delta W_{\mathrm{tip}})/q^2$ as multivariate function of Q/q and N for the charged nanowire and CNP system ($r = 3\,\mathrm{nm}$). The blue dots represent the calculated values and the surface to which the values are fitted is displayed using piecewise cubic interpolation.

Figure 7.7 Induced surface charge densities of the charged nanowire and CNP system ($r = 3\,\mathrm{nm},\ s = 5\,\mathrm{nm},\ q = +e$, (a)−(b) $Q = +10e,\ N = 10$; (c)−(d) $Q = +5e, N = 10$; (e)−(f) $Q = +10e, N = 50$. The CNP is positioned at (a), (c), (e) side direction; (b), (d), (f) tip direction of the charged nanowire.

List of Tables

Chapter 1. Introduction

1.1. Non-classical crystallization and theory of charged nanoparticles

According to the classical crystallization, individual atoms, ions and molecules are the building blocks for crystal growth. [1-3] However, various studies on the mechanism of crystal growth have shown that the building blocks for the growth of several crystals are nanoparticles, not individual atoms. This newly discovered mechanism is named "non-classical crystallization". [4-7] When this mechanism was first suggested, it was difficult to be accepted because there was only indirect evidence for the existence of nanoparticles due to their small size to be observed. However, since the direct observation through in-situ liquid-cell transmission electron microscope (TEM) [8-11], the mechanism has become well established. Figure 1.1 shows that small nanoparticles are formed and coalesced into nanowires, a representative example of the direct observation of non-classical crystallization through in-situ TEM. Not only have several related review papers and books been published, but also symposiums have been held by many academic societies.

Non-classical crystallization has been studied extensively by numerous researchers in the field of crystal growth like in solution, biominerallization, etc. [21-30] showed that most nanoparticle building blocks generated in the gas-phase synthesis of thin films and microstructures through chemical vapor deposition (CVD) are electrically charged, and they played a critical role in non-classical crystallization. By emphasizing the importance of the electric charges contained in the nanoparticles, the underlying theory was named "theory of charged nanoparticles". [22]

As shown in the schematic of 'theory of charged nanoparticles' in Figure 1.2, the charged nanoparticles (CNPs) which are spontaneously generated in the gas phase during most CVD processes act as building blocks in forming the microstructures or nanostructures. Theory of CNPs could well explain paradoxical phenomena which could not be explained by classical crystallization theory. As a representative example and the beginning of suggestion of the theory, there is a phenomenon that occurred during diamond CVD. Figure 1.3 shows that considerably porous and graphitic soot particles grow on an iron substrate while crystalline diamond films grow on the silicon substrate under the equal deposition conditions. [22,31] These different deposition results are originated from the charge transfer rate of substrates, which means that diamond films

in Figure 1.3(a) are deposited on the substrate with a low charge transfer rate while soot is deposited on the substrate with a high charge transfer rate.

Hwang et al. explained that the diamond CNPs in the gas phase remain their original phase and electric charge when they are deposited on the substrate with a low charge transfer rate. [31] Therefore, these diamond CNPs undergo self-assembly caused by their charge and form crystalline diamond film like in Figure 1.3(a). When the diamond CNPs in the gas phase are deposited on the substrate with a high charge transfer rate, however, the electric charges on the CNPs are rapidly transferred to the substrate and nanoparticles that have lost charges change their structure from the original diamond to graphite phase. Figure 1.3(b) shows these neutral graphites having undergone random Brownian coagulation and forming porous soot.

Hwang et al. [31] compared the deposition behavior between grounded and floating iron substrates in order to confirm the assumption that the electric charge stabilized diamond. The grounded iron substrate was set by being placed on a steel and the floating one was placed on a quartz. Herein, after 2h of deposition, graphitic soot grew on the grounded iron substrate whereas diamond was deposited on the floating iron substrate.

Additionally, Hwang et al. [31] and Huh et al. [32] reported that the deposition of diamond or graphitic soot strongly depends on the charge transfer rate of substrates by showing the deposition behavior on a variety of substrates. Graphitic soot was deposited on the substrates with a high charge transfer rate like Pd, Pt, Ni, etc. whereas diamond was deposited on the substrates with a low charge transfer rate like W, Ag, Cu, etc. Thus, these results show that the role of electric charge which stabilizes the diamond was confirmed.

The proofs of CNPs existence were reported not only in diamond, but also in CVD processes of various materials. The size distribution of CNPs as well as their generation were measured using a differential mobility analyzer (DMA) coupled with Faraday cup electrometer (FCE). The schematic of experimental set-up of DMA-FCE system is shown in Figure 1.4. Existence of ZnO [33], Carbon [34], Silicon [35,36], Silicon Nitride [37] and GaN [38] CNPs during CVD processes was confirmed using the DMA-FCE system. Similar to the diamond experiment mentioned above, Youn et al. [23] performed experiments to compare the deposition behavior between floating and grounded Si substrates during the atmospheric CVD of Si. At the same time during the experiment, the generation of CNPs was confirmed using the DMA-FCE system shown in Figure 1.4. The generation of CNPs in the gas phase as well as number concentrations

and size distributions were experimentally confirmed as shown in Figure 1.5. While confirming that both positively and negatively CNPs were abundantly generated in the gas phase, different deposition behaviors were observed on the floating and grounded substrates. Figure 1.6 shows the results where Si nanowires with the diameter of 10 ~ 30 nm were deposited on the floating substrates [Figure 1.6(a)] whereas not nanowires but nanoparticles were deposited on the grounded substrates [Figure 1.6(b)] when flow rate of N_2 is 500 sccm.

The proposed nanowire growth mechanisms include the vapor-liquid-solid (VLS) [39] and oxide-assisted growth (OAG) [40] mechanisms. However, since either catalytic metal or seed of silicon oxide is needed for the suggested mechanisms, another mechanism is required for the explanation of the nanowire growth. In the experimental conditions, the only difference is whether the substrate is floating or grounded, which indicates the growth of silicon nanowires must be attributed to charge build-up on the floating substrate. In other words, electrostatic interaction between CNPs and the substrate affected the growth of the Si nanowires. In addition, from the results that the nanowires grow as a single crystal with a smooth surface not pearl necklace-like or chain-like structure, it was shown that the each CNP underwent epitaxial growth and

charges in them enhance the atomic diffusion kinetics. Therefore, these results also support the assumption that the CNPs acted like a "quasi-solid" or "liquid-like" which indicates their atomic diffusion is enhanced that it seems like liquid phase suggested in the charged cluster model [31].

When flow rate of N_2 carrier gas increases to 1000 sccm, not Si nanowires but Si films were deposited on the floating substrates like grounded one as shown in Figure 1.7. Figure 1.7 shows the results of deposited Si films on the floating and grounded Si substrates. Figures 1.7(a) and (b) show top view and cross section view of Si films deposited on the floating Si substrates, respectively. Figures 1.7(c) and (d) also show top and cross section view of Si films, respectively. The difference of the deposition behaviors of Si between floating and grounded Si substrates is obviously observed as shown in Figure 1.7. A dense film with a thickness of ~220nm was deposited on the floating substrate in Figures 1.7(a) and (b) while a porous film with a thickness of ~190nm was deposited on the grounded substrate in Figures 1.7(c) and (d). The thickness difference also appeared to be due to the effect of electrostatic interactions between CNPs by different electrical conductivity of the substrate. The electrostatic interaction between the charge built up film and the CNPs in the gas phase caused more deposition only on

the floating substrate. Charge build-up on the floating substrate also affected the density of deposited films and it seems that a dense film was made by liquid-like property of CNP retaining charge on the floating substrate as mentioned earlier.

As can be seen from the described results, Hwang et al. studied extensively the non-classical crystallization in the CVD process and has proved the theory of CNPs in various ways publishing ~100 SCI papers to date [41-45] including 3 review papers [4,22,27] and 1 textbook [21]. In the past, non-classical crystallization was mainly applied to the crystal growth in the solution. However, he suggested that it can be applied to the gas phase synthesis of thin films and microstructures by chemical vapor deposition (CVD), physical vapor deposition (PVD) and aerosol deposition (AD).

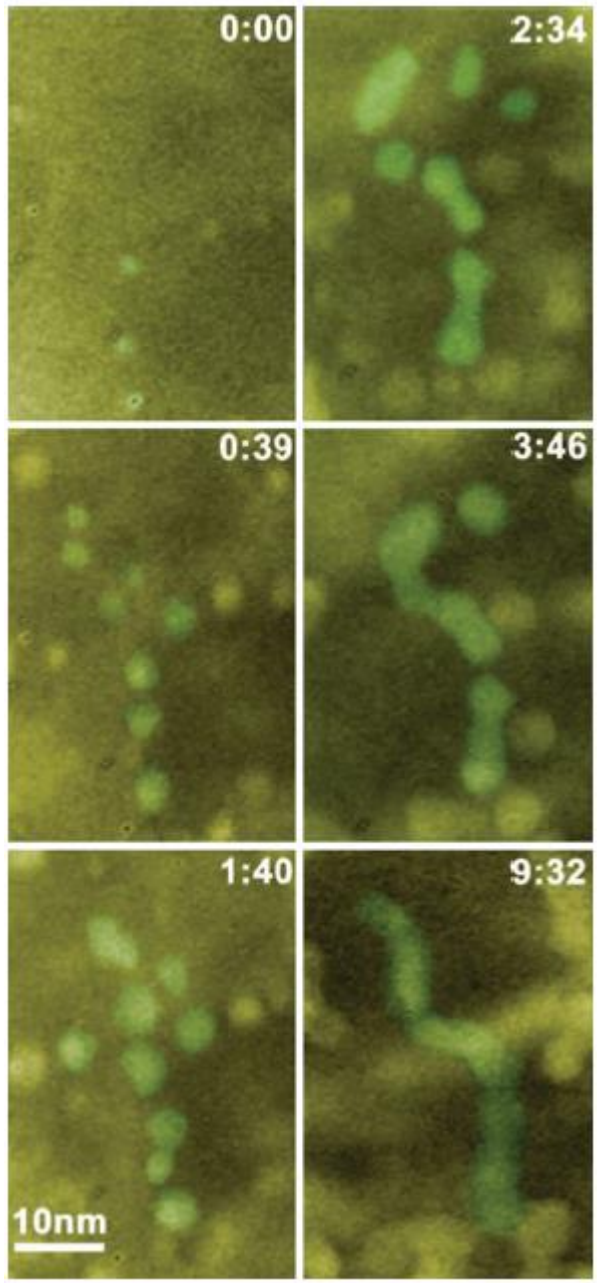

Figure 1.1 Sequential in-situ TEM images showing the initial nucleation and growth of Pt_3Fe nanowires in the molecular precursor solution. Displayed time unit is minutes : seconds. [8]

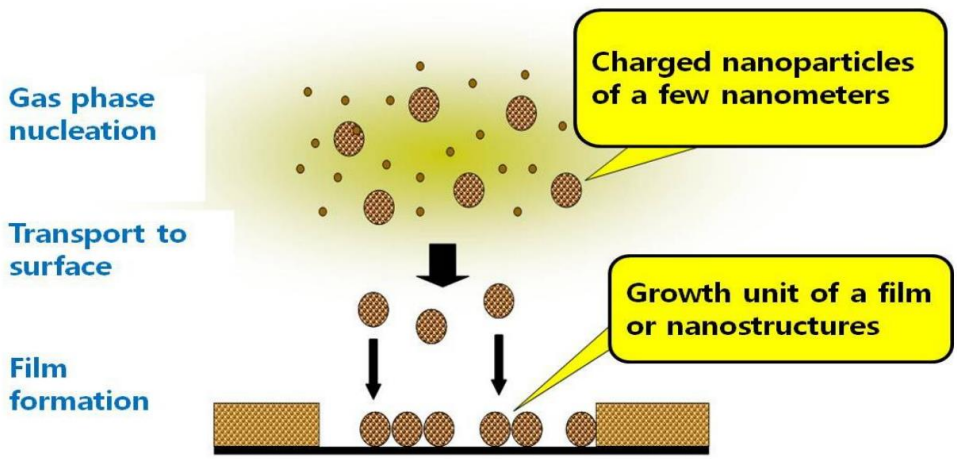

Figure 1.2 Schematic outline of the 'Theory of charged nanoparticles'.

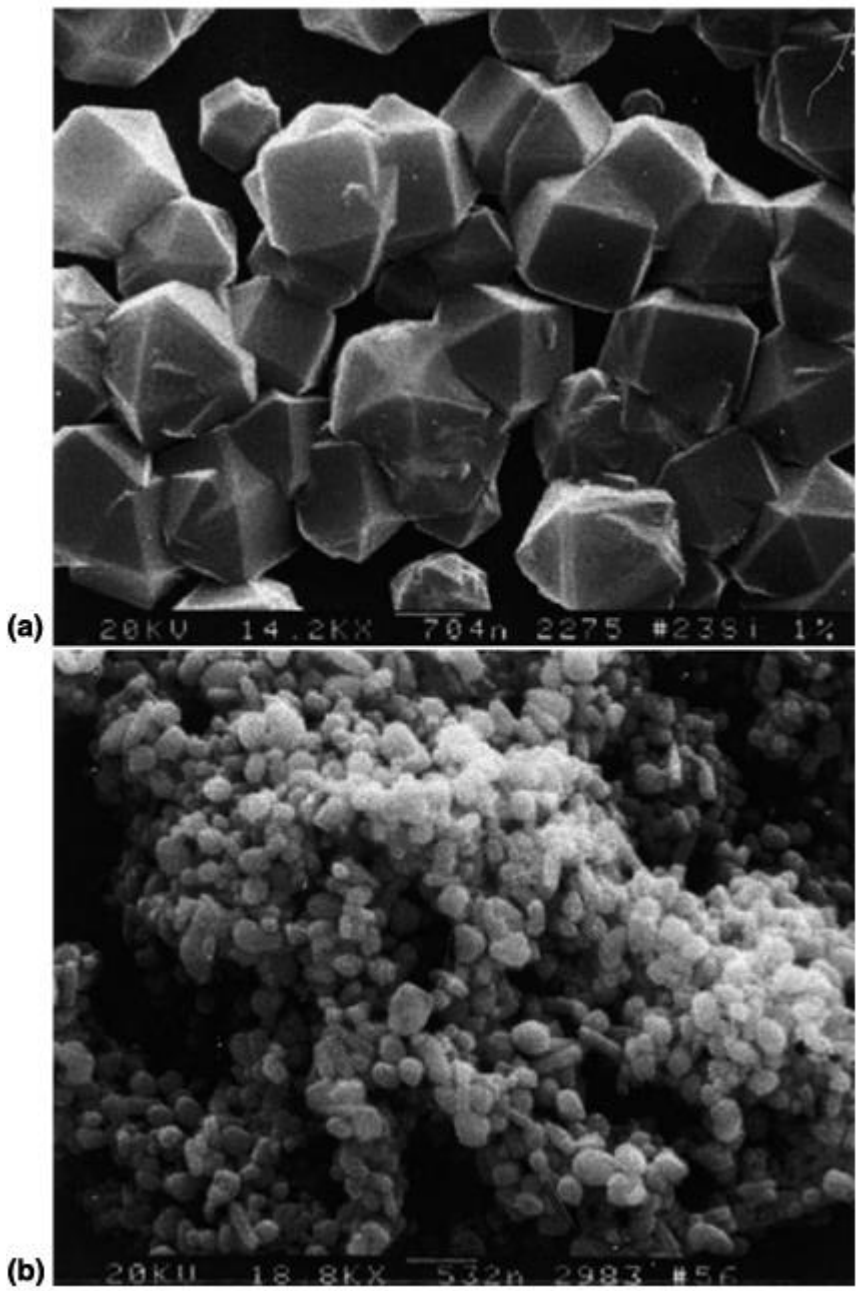

Figure 1.3 (a) Diamond deposited on a silicon substrate and (b) soot deposited on an iron substrate with equal conditions. [22,31]

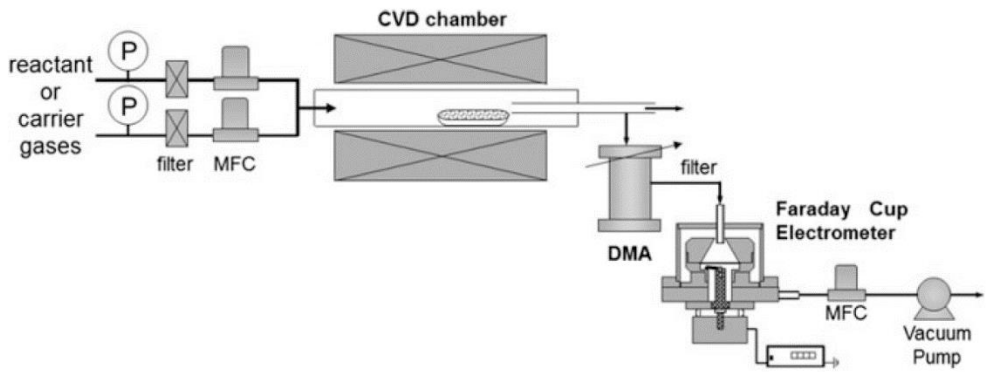

Figure 1.4 Schematic of experimental set-up for the CVD reactor with the DMA-FCE system for measurements of CNPs generated during atmospheric CVD. [21]

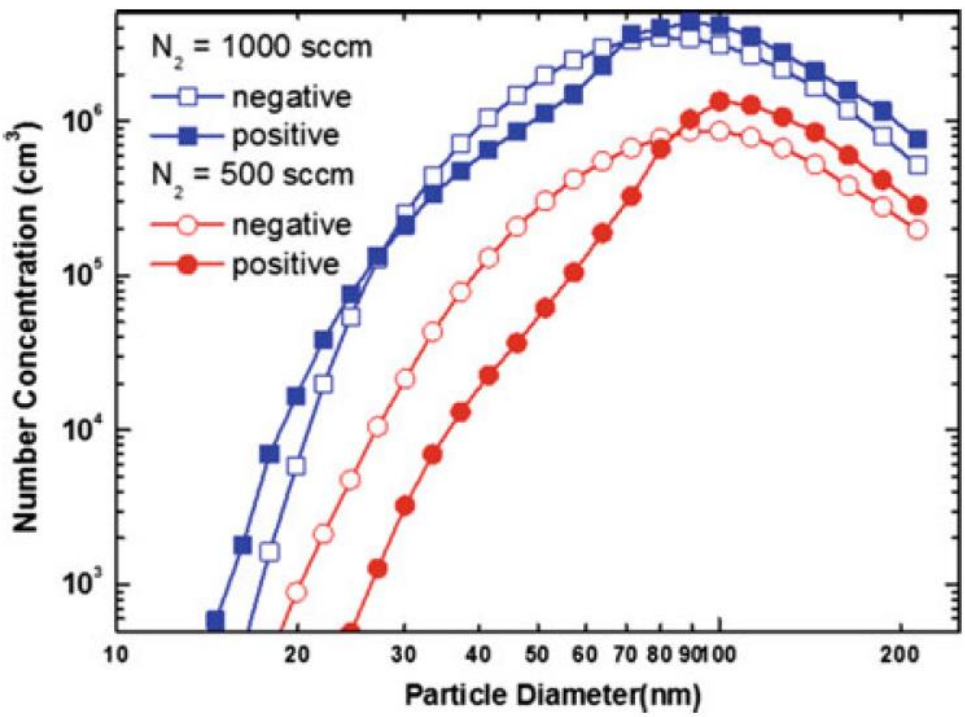

Figure 1.5 Number concentrations and size distributions of negatively (open) and positively (closed)CNPs with N_2 flow rates of 500 and 1000 sccm. [23]

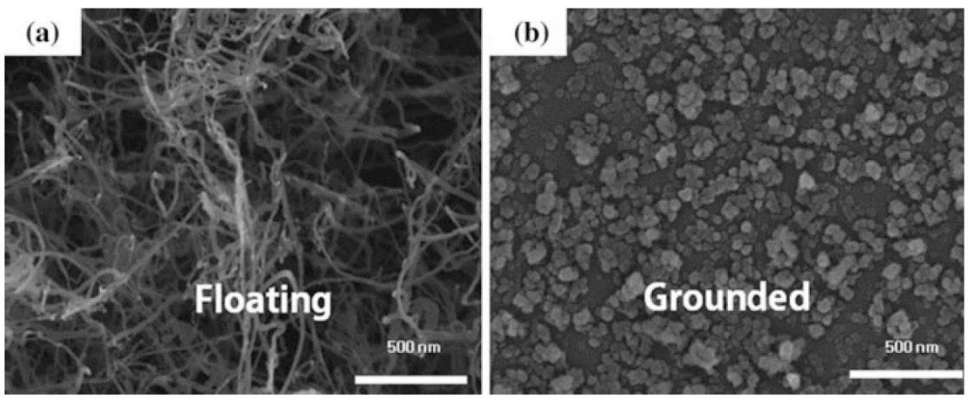

Figure 1.6 Scanning electron microscope (SEM) images of microstructures evolution on (a) floating and (b) grounded Si substrates when N_2 flow rate is 500 sccm. [23]

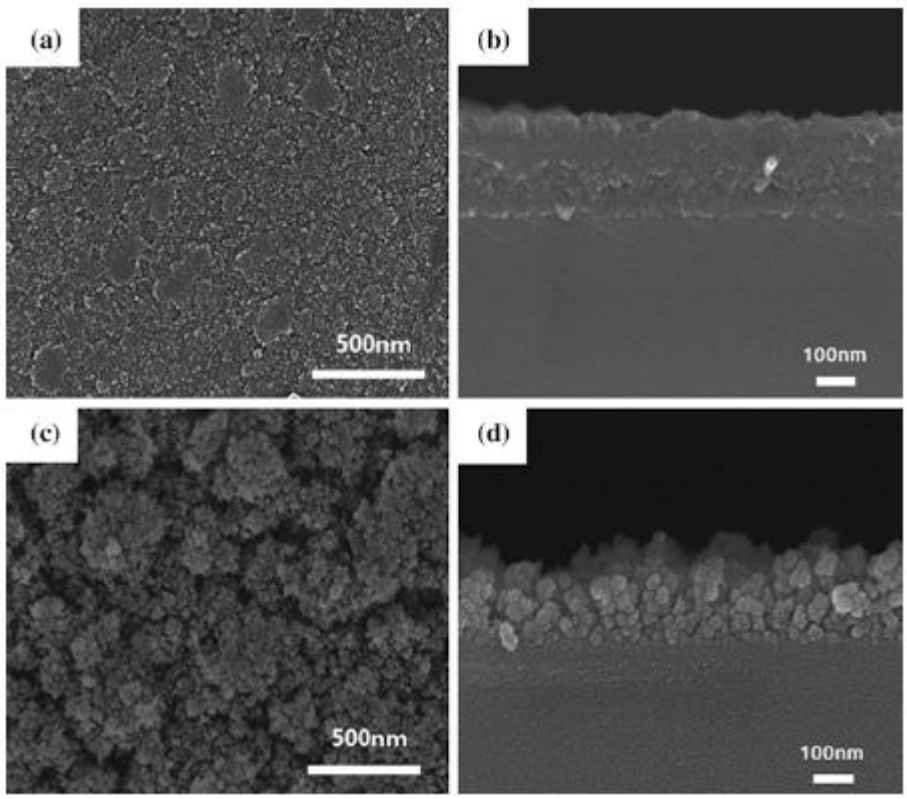

Figure 1.7 SEM images of (a) plane view (b) cross section of films deposited on a floating Si substrate and (c) plane view and (d) cross section of films deposited on a grounded Si substrate at a N_2 flow rate of 1000 sccm. [23]

1.2. Peculiar microstructures by electrostatic interactions

One of the dramatic differences between classical crystal growth theory and theory of CNPs is the effects of electrostatic interactions or potential energy by electrical charges in CNPs. In addition to the results described above in chapter 1.1, a number of peculiar and puzzling microstructures have been reported that cannot be explained by classical crystal growth theory based on the atomic and molecular growth unit, which also does not have electrical charge.

As an example of such peculiar microstructures, Figure 1.8 shows evolution of puzzling structures during Si CVD [21]. Figure 1.8(a) shows three concentric circles with different structures. Starting with a white circle in the center, a dark circle surrounds it, and another white circle surrounds the entire outermost circle. Figure 1.8(b) shows the magnification of Figure 1.8(a) and concentric circles are divided into zones I, II, and III, respectively. Si nanowires grow in both zones I and II [Figures 1.8(c) and (d)] but the number density is higher in zone I than zone II. In zone III, nanoparticles rather than nanowires were mainly and densely deposited as can be seen in Figure 1.8(e). This evolution of microstructure is too difficult and complicated to explain precisely. However, considering such

peculiar structures are evolved on insulating substrates where electric charges would be retained and built up after CNPs are deposited, electrostatic interactions between CNPs in the gas phase and the deposited films on the substrate should be responsible for the puzzling structures.

In studies of ZnO synthesis using thermal evaporation or carbothermal reductions, various peculiar structures with interesting morphologies were also observed such as nanowires [46], nanobelts, nanorings [47,48], nanocoils [49], nanocombs [50] and etc. [51]. Figure 1.9 shows various synthesized ZnO nanostructures [51]. For explaining the growth mechanism of such nanostructures, Kong et al. [47] and Wang [52] suggested that electrostatic interaction played a critical role in the morphological evolution of ZnO and proposed an electrostatic charging model whose origin of the charge is the polar nature of ZnO. Similarly, Cheng et al. suggested that the electric field generation from the decomposition of SiO plays a crucial role in the growth of SiO nanowires. However, the origin of the electrostatic potential energy is still uncertain and unclear. Instead, considering the generation of CNPs were observed during the synthesis of ZnO nanostructures [33], and Si nanowires [35], the electrostatic interactions is most likely originated from the generation of CNPs.

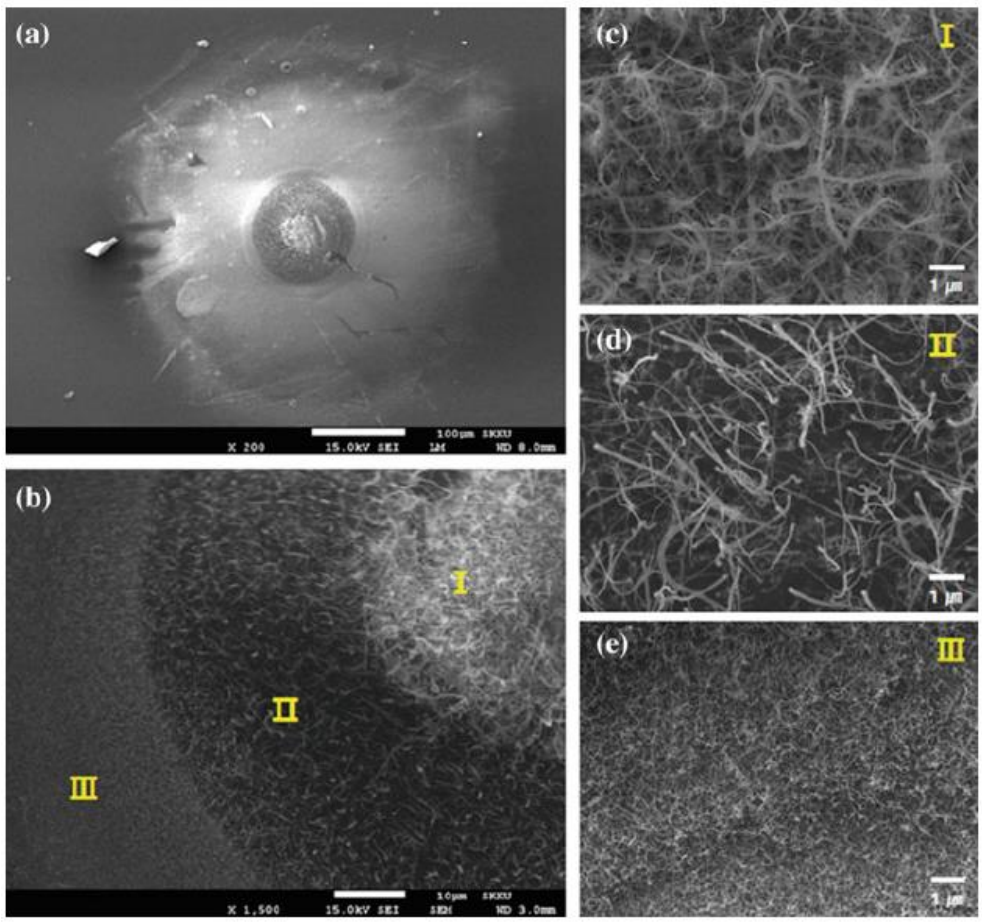

Figure 1.8 Field-emission scanning electron microscope (FESEM) images of microstructures evolution during Si CVD at flow rates of He-diluted SiH_4(10 % SiH_4-90 % He), H_2 and N_2 being respectively 5, 50 and 1000 sccm on glass substrate after 24 h deposition with 5 min of the AC bias of ±50V at 1 Hz treatment. (b) is the enlargement image of (a) and (c), (d) and (e) are the enlargement images of respectively of the zones I, II and III of (b). [21]

Figure 1.9 Various ZnO nanostructures synthesized by thermal evaporation of solid powders except for (c): (a) nanocombs, (b) tetralegs, (c) hexagonal disks/rings (synthesized by solution-based chemical synthesis), (d) nanopropellers, (e) deformation-free nanohelixes, (f) spiral of a nanobelt, (g) nanosprings, (h) single crystal seamless nanoring, (i) a nanoarchitecture composed of a nanorod, nanobow and nanoring, (j) double-side nanocombs, (k) nanobow structure, and (l) rigid helix. [51]

1.3. Purpose of research

According to the theory of CNPs, all the peculiar and puzzling microstructures unexplainable through the classical crystal growth theory where the growth unit is atoms or molecules appear to be affected by electrostatic interactions between CNPs. The effects of electrostatic interactions on several deposition behaviors and microstructures has been successfully elucidated through qualitative analyzes or simple calculations.

Nevertheless, more systematic and quantitative analyzes or calculations are needed to understand the mechanism by which the peculiar microstructures are evolved. Furthermore, it is necessary to investigate the kinetics of CNPs driven by electrostatic potential energy to prove the existence of CNPs.

Therefore, the main purpose of this research is to investigate the underlying physical mechanism of the evolution of peculiar microstructures using CNPs model based on the theory of CNPs through quantitative calculations of electrostatic potential energy between CNPs and kinetic Monte Carlo (kMC) simulations. First, the electrostatic potential energies in two spherical CNP systems were calculated and their physical meaning and origin were also investigated in Chapter 3.

Next, as a relatively simple microstructure among many peculiar ones, the formation of depletion zone around a large particle during low-temperature Si CVD process was first investigated using CNPs model in Chapter 4.

As another puzzling phenomenon, abnormal growth of Si particles selectively deposited on SiN_x patterned on SiO_2 during Si CVD in a Si-Cl-H system reported by Kumomi et al. [53-55] was investigated using three dimensional CNPs model in Chapter 5.

Similarly, in Chapters 6 and 7, the difference in deposition behavior depending on the electrical conductivity of the substrate and the nanowire growth only on the insulator were investigated, respectively, and the effect of the electrostatic interactions among CNPs on the deposition behaviors, which is the ultimate purpose, was studied.

Chapter 2. Theoretical background

2.1. Electrostatic potential energy and capacitance

When a point charge Q_i is brought from infinity to a point $\mathbf{x}_i$ in a region of localized electric fields described by the scalar potential V which converges to zero at infinity, the work done on the charge, i.e. its electrostatic potential energy W_i is

$$W_i = Q_i V(\mathbf{x}_i) \tag{1}$$

The potential V can be expressed as produced by total $(n-1)$ number of charges $Q_j (j = 1,2,\cdots,n-1)$ at positions $\mathbf{x}_j$. Then the potential V is given by

$$V(\mathbf{x}_i) = \frac{1}{4\pi\epsilon_0} \sum_{j=1}^{n-1} \frac{Q_j}{|\mathbf{x}_i - \mathbf{x}_j|} \tag{2}$$

so that the electrostatic potential energy W_i of the charge Q_i is

$$W_i = \frac{Q_i}{4\pi\epsilon_0} \sum_{j=1}^{n-1} \frac{Q_j}{|\mathbf{x}_i - \mathbf{x}_j|} \tag{3}$$

Therefore, the 'total' electrostatic potential energy W of all the charges formed by all the electrostatic forces between them is expressed as follows:

$$W = \frac{1}{4\pi\epsilon_0}\sum_{i=1}^{n}\sum_{j<i}\frac{Q_i Q_j}{|\mathbf{x}_i - \mathbf{x}_j|} \tag{4}$$

As another expression, symmetric form can be expressed by half of summing over i and j without any constraints except for $i = j$ to omit the infinite self-energy of point charges as follows:

$$W = \frac{1}{8\pi\epsilon_0}\sum_{i}\sum_{j}\frac{Q_i Q_j}{|\mathbf{x}_i - \mathbf{x}_j|} \tag{5}$$

For a continuum matter with charge distribution, not a point charge, the total electrostatic potential energy form changes to:

$$W = \frac{1}{8\pi\epsilon_0}\iint\frac{\rho(\mathbf{x})\rho(\mathbf{x}')}{|\mathbf{x} - \mathbf{x}'|}d^3\mathrm{x}d^3\mathrm{x}' \tag{6}$$

where $\rho(\mathbf{x})$ is charge density at position $\mathbf{x}$. Using the relationship between scalar potential V and charge density which is given by

$$V(\mathbf{x}) = \frac{1}{4\pi\epsilon_0}\int\frac{\rho(\mathbf{x}')}{|\mathbf{x} - \mathbf{x}'|}d^3\mathrm{x}' \tag{7}$$

, the total electrostatic potential energy can be written by

$$W = \frac{1}{2}\int\rho(\mathbf{x})V(\mathbf{x})\,d^3\mathrm{x} \tag{8}$$

Additionally, if you want to use the electric field $\mathbf{E}$ to obtain the electrostatic potential energy, the Poisson's equation describing the electric field $\mathbf{E}$ and scalar potential V of a system from charge density ρ can be applied to the electrostatic potential energy equation. It is expressed by

$$\nabla \cdot \mathbf{E} = \frac{\rho}{\epsilon_0} \tag{9}$$

$$\mathbf{E} = -\nabla V \tag{10}$$

where ϵ_0 is the vacuum permittivity. Applying the Poisson's equation to the electrostatic potential energy, it is written by

$$\begin{aligned} W &= -\frac{\epsilon_0}{2}\int V\,\nabla^2 V\,d^3\mathrm{x} \\ &= \frac{\epsilon_0}{2}\int |\nabla V|^2\,d^3\mathrm{x} = \frac{\epsilon_0}{2}\int |\mathbf{E}|^2\,d^3\mathrm{x} \end{aligned} \tag{11}$$

where the integration is over all space. Note that integration by parts is used. Therefore, if the electric field in the system can be calculated, the electrostatic potential energy can also be calculated through the above equation.

In the systems composed of n conductors whose total charges and potentials are Q_i and $V_i\,(i = 1,2,\cdots,n)$, respectively, the total charge of i^{th} conductor relationship can be written by

$$Q_i = \sum_{j=1}^{n} C_{ij} V_j \ (i = 1,2,\cdots,n) \tag{12}$$

Herein the coefficients C_{ii} , $i = j$ are called capacities or capacitances while C_{ij} , $i \neq j$ are called coefficients of induction. Note that $C_{ij} = C_{ji}$. In this study, regardless of the equality of i and j, the name of C_{ij} will be referred to as capacitance coefficients. The total electrostatic potential energy Equation (8) for the system of conductors is written by

$$W = \frac{1}{2} \sum_{i=1}^{n} Q_i V_i \tag{13}$$

When calculating the W between CNPs, since the total charges of each particles are set as the boundary condition, it is necessary to replace the equation potential with total charges and capacitance coefficients. Considering two-conductor system and Equations (12) and (13), total electrostatic potential energy and total charges are written by

$$\begin{aligned} W &= \frac{1}{2}(Q_1 V_1 + Q_2 V_2) \\ Q_1 &= C_{11} V_1 + C_{12} V_2 \\ Q_2 &= C_{12} V_1 + C_{22} V_2 \end{aligned} \tag{14}$$

From the second and third equations in (14), the potentials of conductors are expressed as

$$V_1 = \frac{Q_1 C_{22} - Q_2 C_{12}}{C_{11} C_{22} - C_{12}^2}$$
$$V_2 = \frac{Q_2 C_{11} - Q_1 C_{12}}{C_{11} C_{22} - C_{12}^2} \quad (15)$$

From the first equation in (14) and equations (15), the total electrostatic potential energy is as follows:

$$W = \frac{Q_1^2 C_{22} - 2 Q_1 Q_2 C_{12} + Q_2^2 C_{11}}{2(C_{11} C_{22} - C_{12}^2)} \quad (16)$$

Therefore, we can calculate the total electrostatic potential energy for specified total charges Q_i set as boundary condition, if we know the capacitance coefficients C_{ij}.

Further details are well documented in reference [56,57].

2.2. Finite element method (FEM)

Finite element method is a method for numerically solving partial differential equations widely used in fields of electromagnetism, structural mechanics, fluid flow, and etc. Its basic principle is obtaining approximated solution by subdividing the entire domain into many smaller and simplified elements called ‘finite elements’. The divided elements have node points, and the solution is calculated based on the physical values at the node points called boundary conditions and specified basis (shape) function. [58]

In the case the Lagrange basis function is used, each element is expressed as a polynomial in which the basis function is combined according to the degree. Figure 2.1 shows Lagrange basis functions in one-dimensional elements. The x-axis denotes the normalized element and all points where the value of the basis functions becomes 0 are node points: the node points for linear Lagrange functions in Figure 2.1(a) are η = 0 and 1 while they are η = 0, 0.5 and 1 for quadratic Lagrange functions in Figure 2.1(b).

Since the basis functions used in this study is quadratic Lagrange basis functions, it will be mainly described. Basis functions in Figure 2.1(b) $N_{2n}\ (n = 1,2,3)$ are given by

$$N_{21} = 2(\eta - 1)(\eta - 0.5)$$
$$N_{22} = 4\eta(1 - \eta) \quad (17)$$
$$N_{23} = 2\eta(\eta - 0.5)$$

Note that only the value of n^{th} node points of N_{2n} is 1, and the others are 0. The function of each elements $u(\eta)$ is approximated from this basis functions in the form of a quadratic polynomials as follows:

$$u(\eta) = u_1 N_{21} + u_2 N_{22} + u_3 N_{23} = \sum_{n=1}^{3} u_n N_{2n} \quad (18)$$

These finite elements are assembled into a larger domain of target equations and the FEM then obtain the approximated solution by minimizing an associated error function via the calculus of variations.

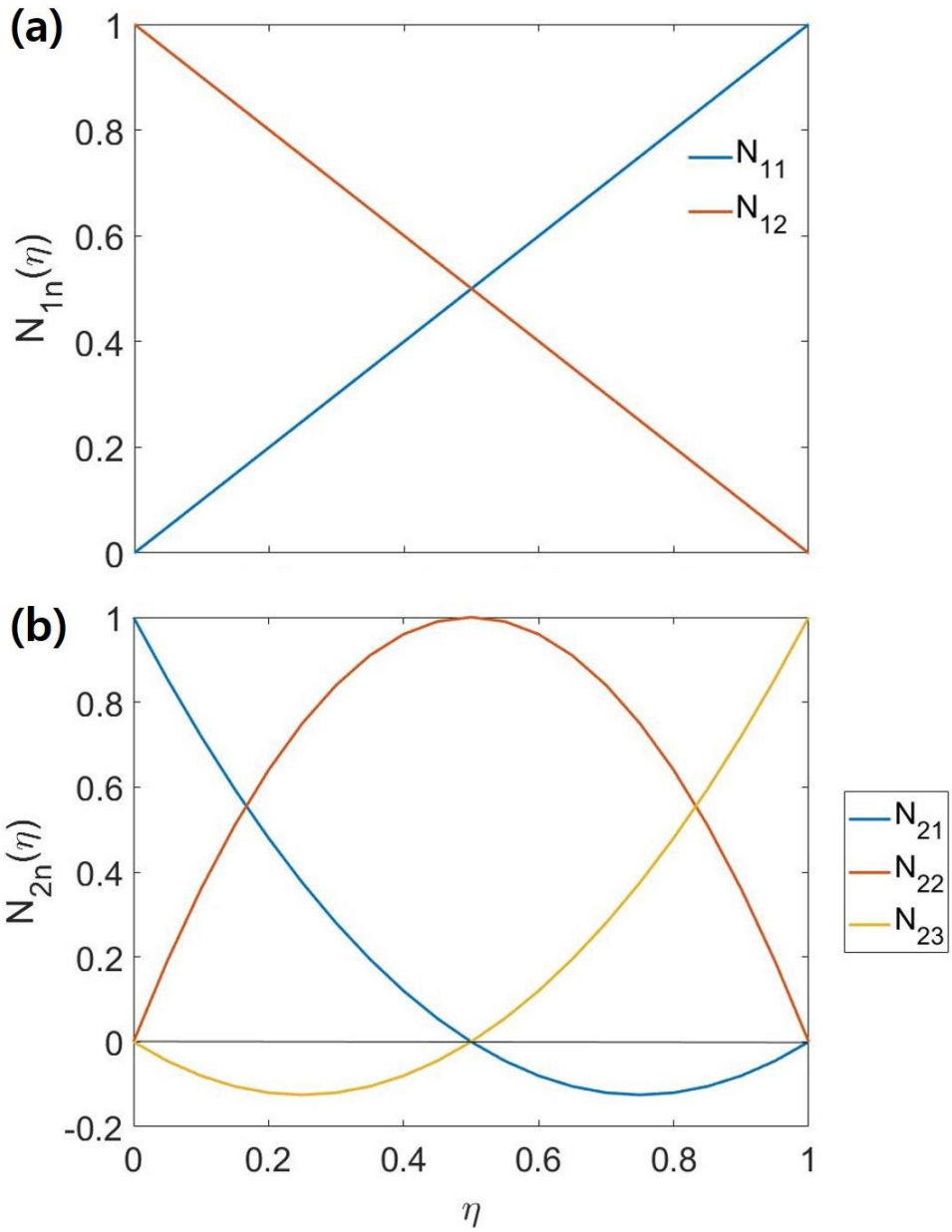

Figure 2.1 (a) Linear (b) Quadratic Lagrange basis functions for one-dimensional elements.

2.3. kinetic Monte Carlo(kMC) simulation

kinetic Monte Carlo (kMC) simulation is motivated from Monte Carlo simulation using random numbers for evolving systems dynamically or over time. It is widely used in the field of diffusion and growth, radiation, surface adsorption, dislocation mobility, etc. In this study it was applied to examine the aggregation dynamics or growth dynamics of the CNP system including their diffusion. The fundamental idea and method of kMC simulation for the nanoparticle diffusion was proposed by Jha et al. [59] for studying the dynamic self-assembly of nanoparticles in solutions.

The method is based on Smoluchowski diffusion equation which describes the time evolution of the probability density function of the Brownian particle position affected by an external Force $F(r)$. In one-dimension, it is written by

$$\partial_t P(r,t) = \partial_r j(r,t) \tag{19}$$

where $P(r,t)$ is the probability density function for a particle to be located at time t and position r. The flux $j(r,t)$ is expressed as follows:

$$j(r,t) = D[\partial_r P(r,t) - \frac{1}{k_B T} F(r) P(r,t)] \tag{20}$$

where k_B and T are the Boltzmann constant and temperature,

respectively. Assuming space and time discretizations as $r_m = dm$ and $t_n = n\Delta t$, a difference Equation (19) can be rewritten by

$$\frac{(P_m^{n+1} - P_m^n)}{\Delta t} = \frac{1}{d}\int_{r_{m-\frac{1}{2}}}^{r_{m+\frac{1}{2}}} \partial_r j(r) dr = \frac{1}{d}(j_{m+\frac{1}{2}} - j_{m-\frac{1}{2}}) \qquad (21)$$

where P_m^n denotes the probability density of the particle being at location r_m at time t_n in the Forward Euler scheme. Here the simultaneous application of consecutive integral form and discretization form in Equation (20) shows that the total probability stays constant.

Thus, the discretization of partial difference equation form is confirmed. In the next step, to derive the master equation, an auxiliary field is defined as

$$w(r) = P(r)e^{\frac{U(r)}{k_B T}} \qquad (22)$$

where $U(r)$ is the potential energy of particle at location r. Then with the relationship between force and potential energy where $F(r) = -dU(r)/dr$ the Equation (20) can be rewritten by

$$j(r) = De^{-\frac{U(r)}{k_B T}} \frac{dw(r)}{dr} \qquad (23)$$

By rearranging Equation (23) for $\frac{dw(r)}{dr}$ and integrating both sides from r_m to r_{m+1} which is discretized interval, the following equation

is obtained:

$$\int_{r_m}^{r_{m+1}} \frac{dw(r)}{dr} dr = w_{m+1} - w_m = P_{m+1} e^{\frac{U_{m+1}}{k_B T}} - P_m e^{\frac{U_m}{k_B T}} \\ = \frac{1}{D} \int_{r_m}^{r_{m+1}} j(r) e^{\frac{U(r)}{k_B T}} dr \approx \frac{1}{\mathrm{D}} j_{m+\frac{1}{2}} \frac{d}{2} [e^{\frac{U_{m+1}}{k_B T}} + e^{\frac{U_m}{k_B T}}] \tag{24}$$

Here, the approximate equal sign comes from that $e^{\frac{U_m}{k_B T}}$ changes much drastically than the flux $j(r)$. From Equation (24), the master equation is obtained as follows:

$$j_{m+\frac{1}{2}} = \frac{2D}{d} \left[P_{m+1} \frac{e^{-\frac{U_m}{k_B T}}}{e^{-\frac{U_m}{k_B T}} + e^{-\frac{U_{m+1}}{k_B T}}} - P_m \frac{e^{-\frac{U_{m+1}}{k_B T}}}{e^{-\frac{U_m}{k_B T}} + e^{-\frac{U_{m+1}}{k_B T}}} \right] \\ = \frac{2D}{d} [P_{m+1} K(m+1 \to m) - P_m K(m \to m+1)] \tag{25}$$

where $K(m+1 \to m)$ and $K(m \to m+1)$ is the dimensionless transition rates. These rates are identical with the definition of transition probability in Glauber transition probability [60] where for a change in states $s_i \to s_f$ with energies of E_i and E_f, respectively, the transition probability is defined as

$$p(s_i \to s_f) = \frac{1}{1 + \exp\left(\frac{E_f - E_i}{k_B T}\right)} \tag{26}$$

Finally, using the master Equation (25), the numerical solution of the Smoluchowski diffusion Equation (19) can be obtained through the simulation if we know the relation between the time step Δt and

step size in space d. Considering one−dimensional diffusion problem with a constant drift Force F where makes potential energy $U(r) = -Fr$, particle would move from a position r_n to $r_{n+1} \in \{r_n, r_n \pm d\}$ in a Monte Carlo step d. Then, the transition probability for the movement is given from Glauber equation (26) by

$$p(r_n \to r_n \pm d) = \frac{1}{2}\left(\frac{1}{1+e^{\mp\frac{Fd}{k_BT}}}\right) \approx \frac{1}{4}\left(1 \pm \frac{Fd}{k_BT}\right) \tag{27}$$

where the drift force F is sufficiently small. Note that the half term is the selection probability for the either + or – direction. The mean drift is given by

$$\langle r_{n+1} \rangle = \langle r_n \rangle + dp_+ - dp_- \approx r_n + \frac{Fd^2}{4k_BT} \tag{28}$$

and the mobility μ can be expressed by

$$\mu = \frac{\langle r_{n+1} \rangle - \langle r_n \rangle}{F\Delta t} = \frac{d^2}{4k_BT\Delta t} \tag{29}$$

Using Einstein's relation, $D = \mu k_BT$, the time step is defined as $\Delta t = d^2/4D$ and is generalized to an arbitrary dimension m as

$$\Delta t = \frac{d^2}{4mD} \tag{30}$$

Therefore, for three−dimensional systems of $m = 3$, $\Delta t = d^2/12D$. From the results derived above, the numerical solution of diffusion equation can be obtained with time evolution $N\Delta t$ for N Monte−Carlo steps.

Chapter 3. Electrostatic potential energy of two-particle systems

3.1. Introduction

As the first step to investigate the effects of electrostatic interactions between CNPs, the accurate calculation of electrostatic potential energy is needed. Considering CNPs in the gas phase are mainly in the spherical forms, electrostatics between electrically charged spheres was mainly discussed.

Two methods of calculation were used: using capacitance coefficients, an analytical method, and finite element method (FEM), a numerical method. The capacitance coefficients method can only be used for conductors and only when the values of the capacitance coefficients of the system are known, but has the advantage of being fast in calculation rate. On the other hand, the FEM can be used for

both dielectric materials and conductors, but its calculation rate is slow and requires separate software for calculation.

In the previous studies, the capacitance coefficients of the two-particle systems are known [57,61] and electrostatic interaction between two conducting was studied using various ways including capacitance coefficients [57], image charges [62,63], etc.

In this chapter, the electrostatic potential energies of various two-particle systems were calculated and investigated using two methods mentioned above. Furthermore, the physical origin of its property was also investigated through analysis of surface charge density of CNPs: it could be only analyzed using FEM, numerical method. Comparison of two methods was also included.

3.2. Computational Details

3.2.1 Capacitance coefficients method

We used Equation (16) which describes the electrostatic potential energy of systems featuring two conducting CNPs modeled in Figure 3.1. The two CNPs were modeled as spheres with radii of R and r, respectively. For convenience of calculation, let R be the radius of the large CNP and r the radius of the small CNP. Assuming

that the CNPs serve as solid conductors in a continuum, the electrostatic potential energy W is obtained from Equation (16) where Q and q are the charges on each CNPs and $C_{ij}(i = 1,2, C_{12} = C_{21})$ are the capacitance coefficients of the two CNPs. When the CNPs are spherical conductors, the capacitance coefficients are: [57,61]

$$C_{11} = 4\pi\epsilon_0 Rr \sinh U \sum_{n=0}^{\infty} [R \sinh nU + r \sinh(n+1)U]^{-1} \quad (31)$$

$$C_{22} = 4\pi\epsilon_0 Rr \sinh U \sum_{n=0}^{\infty} [r \sinh nU + R \sinh(n+1)U]^{-1} \quad (32)$$

and

$$C_{12} = -4\pi\epsilon_0 \frac{Rr}{c} \sinh U \sum_{n=0}^{\infty} [\sinh nU]^{-1} \quad (33)$$

where ϵ_0 is the vacuum permittivity, $r_i(i = 1,2)$ the radii of the CNPs, $c = R + r + s$ the center-to-center distance between the two spherical CNPs, and a dimensionless parameter U is:

$$U = \cosh^{-1}\left(\frac{c^2 - R^2 - r^2}{2Rr}\right) \quad (34)$$

In this study, we approximated the values of C_{ij} (to an accuracy of 10^{-7}) via finite summation of the infinite series shown in Equations (31)-(33).

3.2.2 FEM calculations

We used Poisson's equation expressed in Equations (9) and (10), which describes the electric field and potential of a system, to calculate the electrostatic potential energy W and surface charge density (conductors) or polarization (dielectrics) of systems composed of both conducting and dielectric CNPs. The W is obtained from Equation (11) and surface charge density σ for conductor and polarization $\mathbf{P}$ for dielectric is obtained as

$$\sigma = \epsilon_0(\mathbf{E} \cdot \hat{\mathbf{n}})$$
$$\mathbf{P} = \epsilon_0(\epsilon_r - 1)\mathbf{E} \tag{35}$$

where $\hat{\mathbf{n}}$ denotes the normal vector to the surface of a CNP and ϵ_r denotes the dielectric constant of the linear, homogeneous and isotropic dielectric CNP.

We numerically solved the equation using FEM and COMSOL Multiphysics AC/DC Module [64]. Large and small CNPs were modeled as spheres with radii of R and r, respectively [see Figure 3.1]. They were considered solid of continuum matter. We used a spherical infinite element domain scheme with a finite radius of R_∞, implemented in COMSOL. The two spheres were placed in a vacuum with a relative permittivity of 1. A fine mesh of approximately 270,000 tetrahedral quadratic Lagrange elements was used. The elements of the boundaries of small particles were manually adjusted

for higher accuracy, while the other elements were automatically generated with the 'finer' mesh setting in COMSOL. The outer surface of the infinite element domain was set to ground, and the surface charges of the particles were set to Q and q, respectively. Here, the 'terminal' physics setting in COMSOL was used for setting the surface charges of conducting particles while the 'surface charge density' physics setting was used for dielectric particles. Note that the dielectric constant ϵ_r should be set for the system with dielectric particles. We varied the separation distance s between the surfaces of the particles to calculate the potential energy and surface charge density of the system [see Figure 3.1].

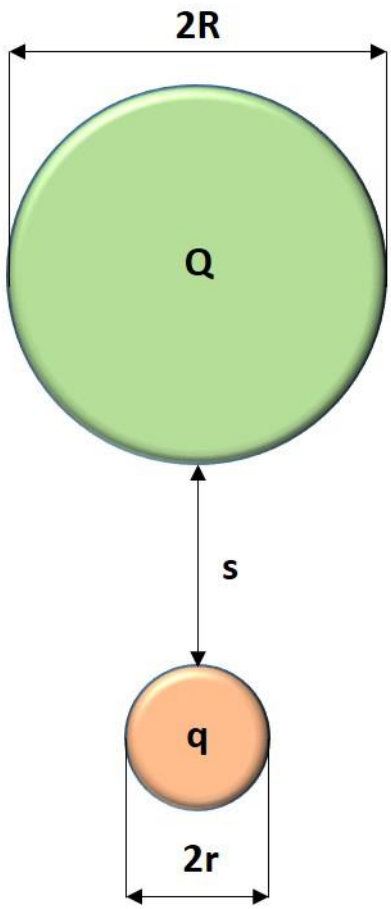

Figure 3.1 A system of two spherical CNPs.

3.3. Results and discussions

3.3.1 Electrostatic potential energy of two-conducting particle systems

First, using the capacitance method and FEM implemented in COMSOL, we calculated the W between two spherical conducting CNPs. From here on, unless otherwise specified, all CNPs are considered as conductors. Figure 3.1 shows the two spherical CNPs, where R and Q denote the radius and charge of the large particle, respectively; r and q denote the radius and charge of the small particle, respectively; and s denotes the separation distance between the surfaces of both particles.

When the large and small CNPs have opposite charges, electrostatic interparticle interaction is always attractive. W, excluding self-energy, more sharply decreases as s decreases compared with the W of a monopole ($W_{monopole}$) of the two oppositely charged point particles. [see Figure 3.2(a)].

In the case the two CNPs have like charges, the electrostatic interparticle interaction looks complex. Figure 3.2(b) shows the electrostatic potential energy W excluding self-energy as a function of s for the two-particle system ($R = 250\,\mathrm{nm}$, $Q = +5e$; $r = 10\,\mathrm{nm}$,

$q = +e$).

With increasing s, W rapidly increases and then slowly decreases; the trend depends on the relationship between s and the transition separation distance s^*. The results indicate that interparticle interaction is attractive when s is less than s^* and repulsive when s is greater than s^*. s^* is 55 nm in Figure 3.2(b). This interesting behavior of particles with like charges contrasts with the repulsive monopole interaction between point particles with like charges.

This attraction between particles with like charges appears to be related to the structural evolution of nanoparticles during CVD. CNPs act as building blocks for the growth of thin films and nanostructures during CVD. Such electrostatic interactions can clarify the deposition behavior and microstructural evolution of thin films and nanostructures in CVD.

For the structural evolution of CNPs, when the particles are farther away from s^*, to attract each other they need to overcome the W^* at s^*. The values of s^* and W^* determine the probability of coalescence between the two particles. To understand the characteristics of s^* and W^*, we examined W as a function of s for different Q/q values. Figure 3.3(a) compares the dependences of W/q^2 on s for different Q/q ratios (1–100). For each value of Q/q,

the values of s^* and W/q^2 are expressed as red points. s^* decreases with increasing Q/q. At a Q/q of 1, 5, 10, 25, 50, and 100, the thickness of the attraction zone of the system, expressed as s^*, is 144.5, 55.0, 34.6, 17.2, 8.9, and 3.4 nm, respectively. W^*/q^2 increases with increasing Q/q. At a Q/q of 1, 5, 10, 25, 50, and 100, W^*/q^2 is 0.003, 0.020, 0.044, 0.120, 0.252, and 0.524 eV/e^2, respectively.

Additionally, to explore the more details of the electrostatic interactions between CNPs with like charges, we investigated the characteristic behavior of s^* by varying large particle radius R. Figure 3.4 plots s^* as a function of Q/q for two CNP systems with charges of q and Q, radii of $r = 20\,\mathrm{nm}$, and $R = 100 - 500\,\mathrm{nm}$. For any given R, s^* commonly decreases when Q/q increases. Thus, the smaller the charge accumulation of deposited CNPs, the longer the attractive interaction range. Figure 3.4 also shows that for any given Q/q, s^* increases as the radius R of a (large) CNP increases. Thus, larger CNPs tend to engage in attractive interactions with more CNPs (with like charges), further increasing R.

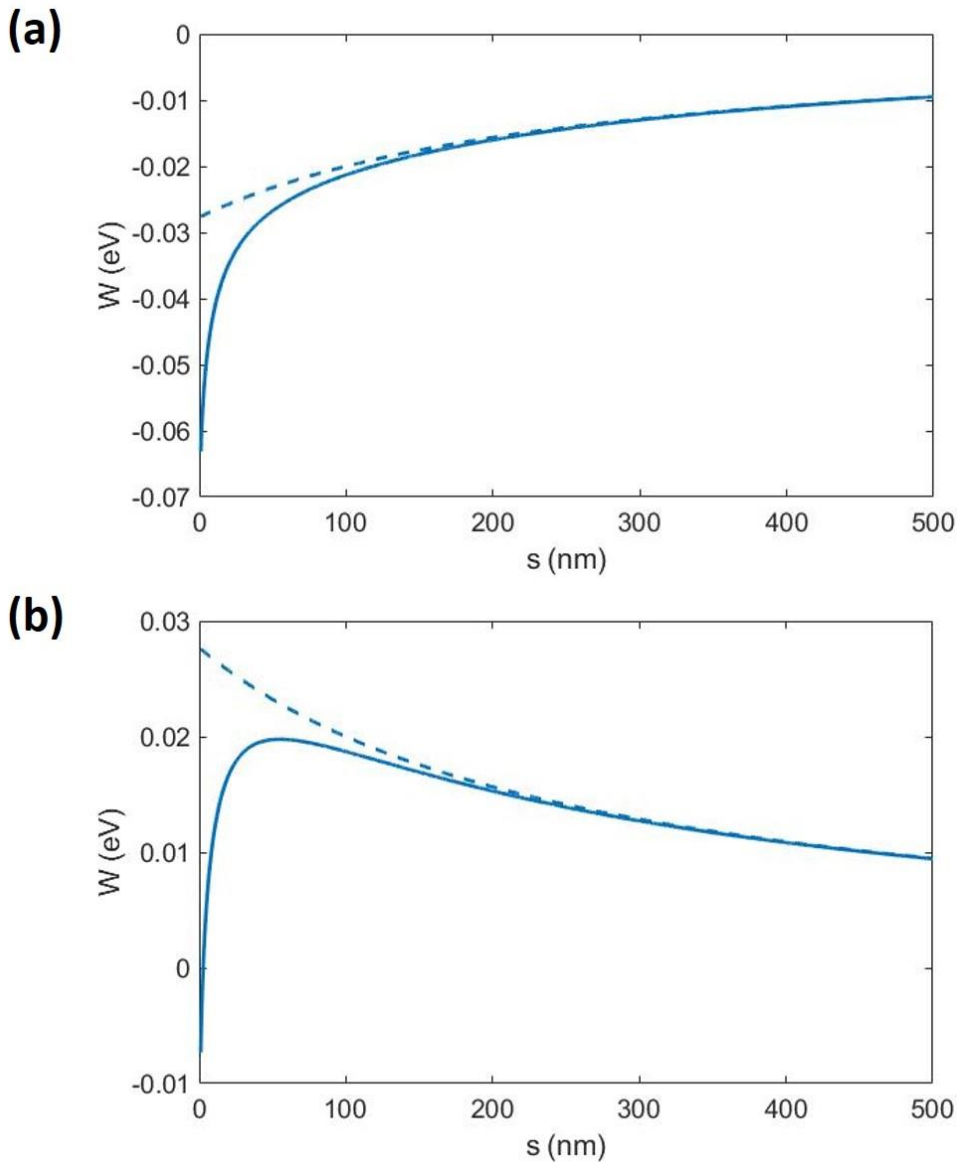

Figure 3.2 W (solid line), excluding self−energy, as a function of s for the two−particle system, with $R = 250$ nm and $r = 10$ nm: (a) $Q = +5e$ and $q = -e$; (b) $Q = +5e$ and $q = +e$. The results of W are compared with the $W_{monopole}$ of the charged two point particles: $W_{monopole} = \frac{1}{4\pi\epsilon_0}\frac{Qq}{R+r+s}$ (dashed line).

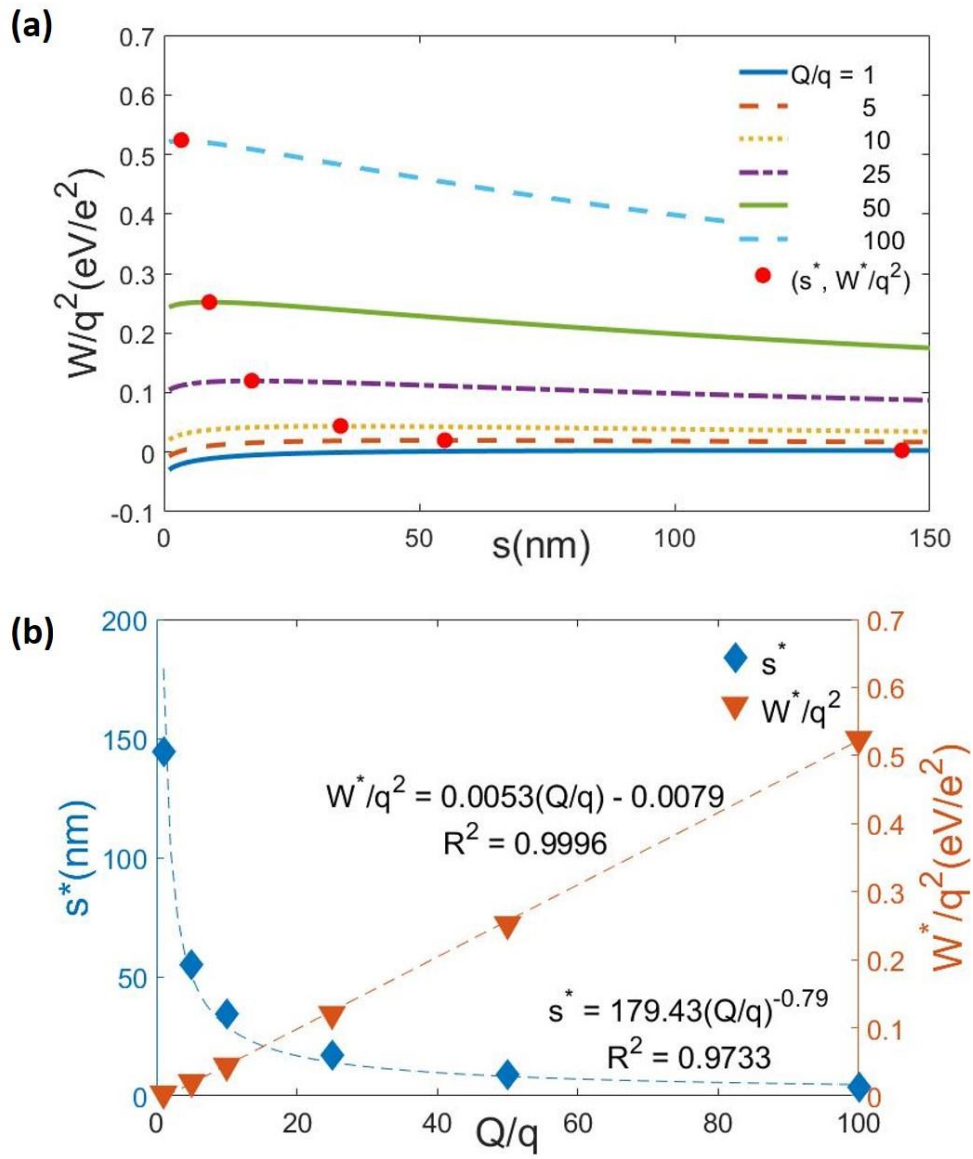

Figure 3.3 (a) W, excluding self-energy, divided by q^2 as a function of s for the two-particle system ($R = 250$ nm, $r = 10$ nm) (charge ratio Q/q: 1–100); the values of s^* and W^*/q^2 are expressed for each Q/q. (b) The values of s^* and W^*/q^2 as a function of Q/q for the same system.

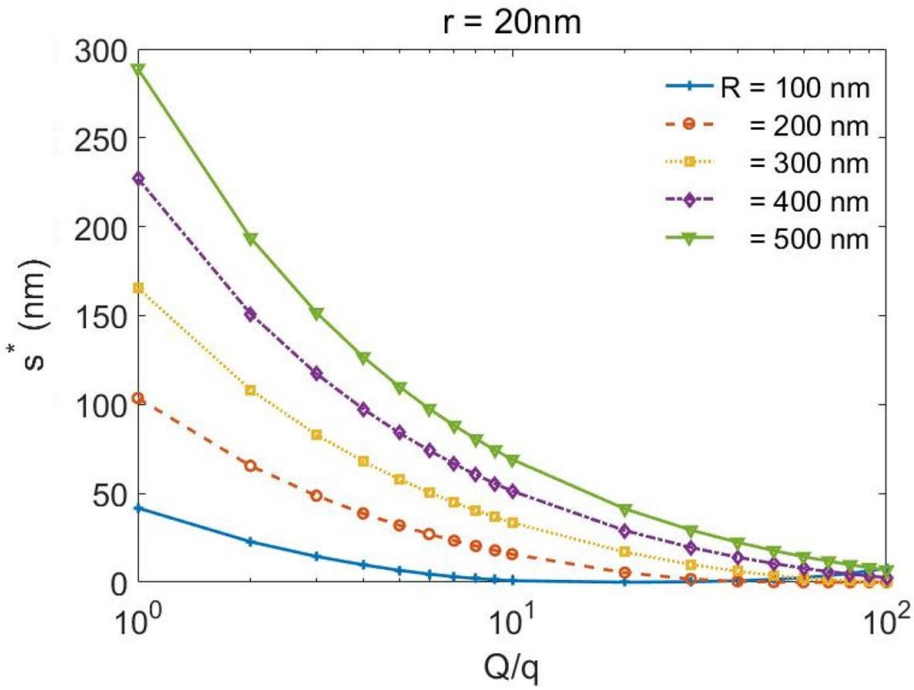

Figure 3.4 s^* as a function of Q/q, as revealed by electrostatic potential energy calculations for a system consisting of two CNPs with charges of q and Q, radii of $r = 20\,\mathrm{nm}$ and $R = 100 - 500\,\mathrm{nm}$.

3.3.2 Physical origin of interparticle electrostatic interactions

To further understand the physical interaction between two conducting spherical CNPs with like charges, we investigated the surface charge redistribution of the two CNPs, which is induced by their mutual polarization, by calculating the surface charge density of the particles. The total surface charge density (σ_{tot}) calculated with COMSOL consists of net charge (σ_{net}) and induced charge (σ_{ind}). We obtained σ_{ind} associated with surface charge redistribution by subtracting σ_{net} from σ_{tot}. The σ_{net} values for the large and small CNPs are $Q/4\pi r^2$ and $q/4\pi r^2$, respectively.

Figure 3.5 shows the results calculated with $Q = +50e$, $q = +e$ $R = 250\ \mathrm{nm}$, and $r = 10\ \mathrm{nm}$ for the three representative s values. In the color scale of Figures 3.5(a)–(c), the reddest and bluest colors represent the most positive and negative values of surface charge density, respectively; the thin blue region on the surface near the right pole of the large particle indicates that a negative charge is induced on the surface of the large CNP adjacent to the small CNP. This region is thickest at $s = 5\ \mathrm{nm}$ (Figure 3.5(a)) and thinnest at $s = 20\ \mathrm{nm}$ (Figure 3.5(c)). This indicates that the induced surface charge density of the large CNP is strongest at $s = 5\ \mathrm{nm}$ and weakest at $s = 20\ \mathrm{nm}$. Figure 3.5(d) plots the W of this system as a function

of s. The W values for the interaction depicted in Figure 3.5(a)–(c) are indicated on the graph of Figure 3.5(d). At $s = 5\,\mathrm{nm}$, the large and small CNPs attract each other (Figure 3.5(a)). At $s = 10\,\mathrm{nm}$ (i.e., s^*; Figure 3.5(b)), the W (i.e., W^*) is the highest (Figure 3.5(b)). At $s = 20\,\mathrm{nm}$, the interparticle interaction is repulsive (Figure 3.5(c)).

Figures 3.5(a)–(c) reveal the s–dependent distribution patterns of the surface charge density of the small CNP. At $s = 5\,\mathrm{nm}$ (the attraction zone), positive charges are induced on the surface area of the small CNP adjacent to the large CNP, while negative charges are induced on the remaining surface area of the small CNP (Figure 3.5(a)). Thus, the adjacent areas of the two CNPs have opposite charges, which will induce interparticle attraction. At $s = 10\,\mathrm{nm}$ (i.e.,s^*), weaker positive charges than those at $s = 5\,\mathrm{nm}$ are induced on the left and right poles of the small CNP, while weaker negative charges are induced on the other areas (Figure 3.5(b)). Consequently, the net force is zero, and the two CNPs are neither attractive nor repulsive. When the small CNP is away from the attraction zone or in the repulsion zone ($s = 20\,\mathrm{nm}$; Figure 3.5(c)), the surface charge distribution is opposite to that at $s = 5\,\mathrm{nm}$. Negative charges are induced on the surface area of the small CNP adjacent to the large CNP, while positive charges are induced on the remaining surface area of the small CNP. Thus, the adjacent areas of

the two CNPs have negative charges, which will induce interparticle repulsion.

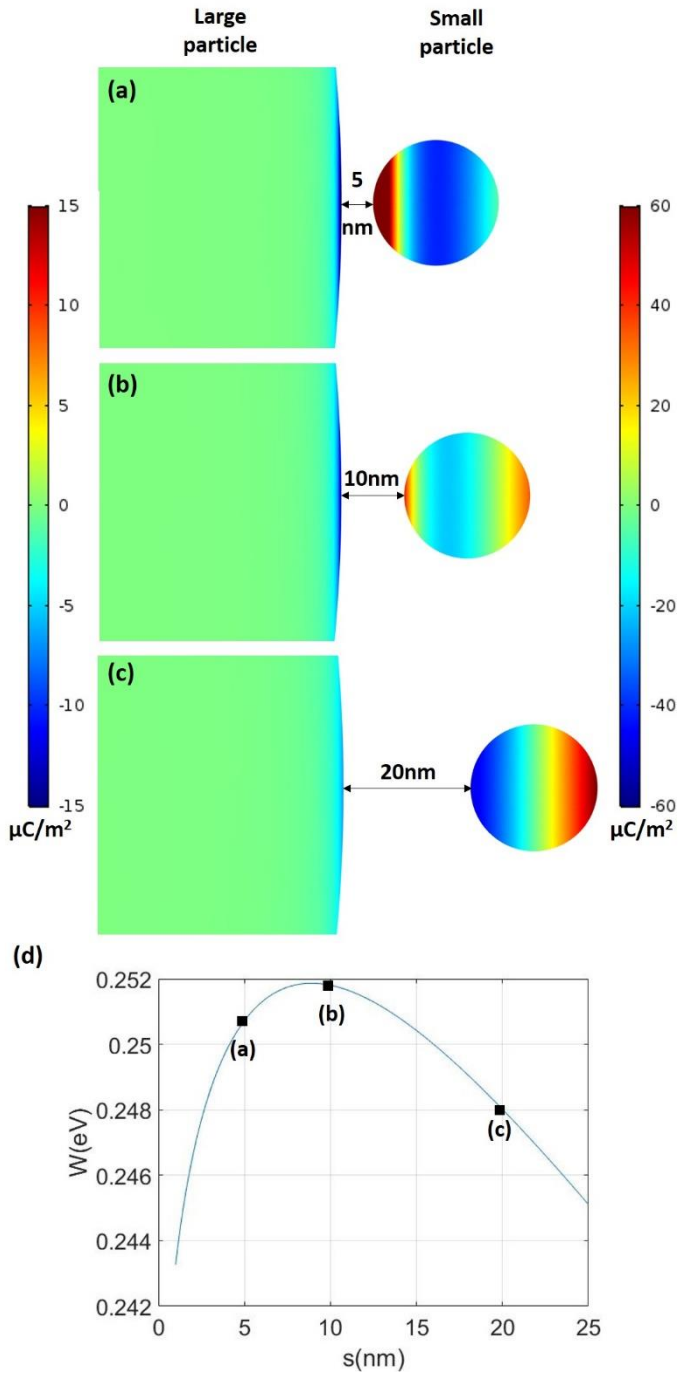

Figure 3.5 Induced surface charge densities of the two-particle system ($R = 250$ nm, $Q = +5e$; $r = 10$ nm, $q = +e$), with representative s of (a) 5, (b) 10, and (c) 20 nm. The left and right color legends are for the large and small particles, respectively. (d) W as a function of s for the system; the figure depicts W values of (a)–(c).

3.3.3 Electrostatic potential energy of two-dielectric particle systems

Since not only conductor particles but also dielectric particles are used a lot in actual deposition, their electrostatic potential energy needs to be investigated as well. Thus, we calculated the electrostatic potential energy W for varying dielectric constants of particles ϵ_r under the system calculated in Figure 3.2(b). Note that the surface bound charge density is assumed to be constant as $Q/4\pi r^2$ and $q/4\pi r^2$, respectively.

Figure 3.6 plots the W as a function of s for two dielectric particle systems with dielectric constant ϵ_r from 1.1 to 1000 including ϵ_r = 11.7 of Si, radii of $R = 250\,\mathrm{nm}$ and $r = 10\,\mathrm{nm}$, and charges of $Q = +5e$ and $q = -e$. The W of two conducting particles shown in Figure 3.2(b) is also plotted for comparison. For any given ϵ_r, W decreases when ϵ_r increases. Note that for conductors, ϵ_r is infinite. As the distance s increases, the W becomes almost the same regardless of the value of ϵ_r. However, as the distance s between the two particles gets closer, the effect of ϵ_r on W increase. The smaller the dielectric constant, the more dominant the interparticle repulsion rather than the interparticle attraction. To further analyze the effect of the dielectric constant ϵ_r on W, we

investigated the polarization $\mathbf{P}$ inside the particles. When the particles are conductors in Figure 3.5, excess charges are distributed over the surface and move freely on the surface, which makes induced surface charge distribution σ_{ind}. However, if the particle is dielectric, instead of the excess charge moving freely, it creates an electric field that opposes the external electric field called polarization $\mathbf{P}$ inside the particle. Considering the spherical symmetry, the distance s was controlled on the basis of the x−axis, and the polarization $\mathbf{P}$ represented a vector in the x−direction, $\mathrm{P_x}$ in the xy−plane.

Figure 3.7 shows the results calculated with $\epsilon_r = 11.7$, $Q = +50e$, $q = +e$ $R = 250\ \mathrm{nm}$, and $r = 10\ \mathrm{nm}$ for the three s values. In the color scale of Figure 3.7, the red and blue colors represent the positive and negative x−direction magnitude of polarization, respectively. Note that the polarization vector denotes a positive charge of electric dipoles at the end of the vector and a negative charge of electric dipoles at the beginning of the vector as shown in Figure 3.7. The blue region near the right pole of the large particle indicates that x−direction polarization $\mathrm{P_x}$ was formed in the negative direction on the large CNP adjacent to the small CNP. This region is the largest at $s = 5\ \mathrm{nm}$ (Figure 3.7(a)) and smallest at $s = 20\ \mathrm{nm}$ (Figure 3.7(c)). This indicates that the $\mathrm{P_x}$ of the large CNP is strongest at $s = 5\ \mathrm{nm}$

and weakest at $s = 20\,\mathrm{nm}$.

Figure 3.7 reveals the s-dependent P_x patterns of the of the small CNP. Since the value of W as a function of s is almost same as Figure 3.5(d), W in Figures 3.7(a)-(c) can also be seen as described in Figure 3.5(d). At $s = 5\,\mathrm{nm}$ (the attraction zone), negative P_x is formed in the the small CNP adjacent to the large CNP, while positive P_x is formed on the remaining surface area of the small CNP (Figure 3.7(a)). Thus, the adjacent areas of the two CNPs have same direction of P_x, which will induce interparticle attraction. At $s = 10\,\mathrm{nm}$ (i.e., s^*), smaller region of negative P_x than those at $s = 5\,\mathrm{nm}$ is formed on the left while larger region of positive P_x is formed on the right of the small CNP (Figure 3.7(b)). Consequently, the net force is zero, and the two CNPs are neither attractive nor repulsive. When the small CNP is away from the attraction zone or in the repulsion zone ($s = 20\,\mathrm{nm}$; Figure 3.7(c)), only positive P_x is formed on the region of the small CNP adjacent to the large CNP. Thus, the adjacent areas of the two CNPs have opposite direction of P_x, which will induce interparticle repulsion.

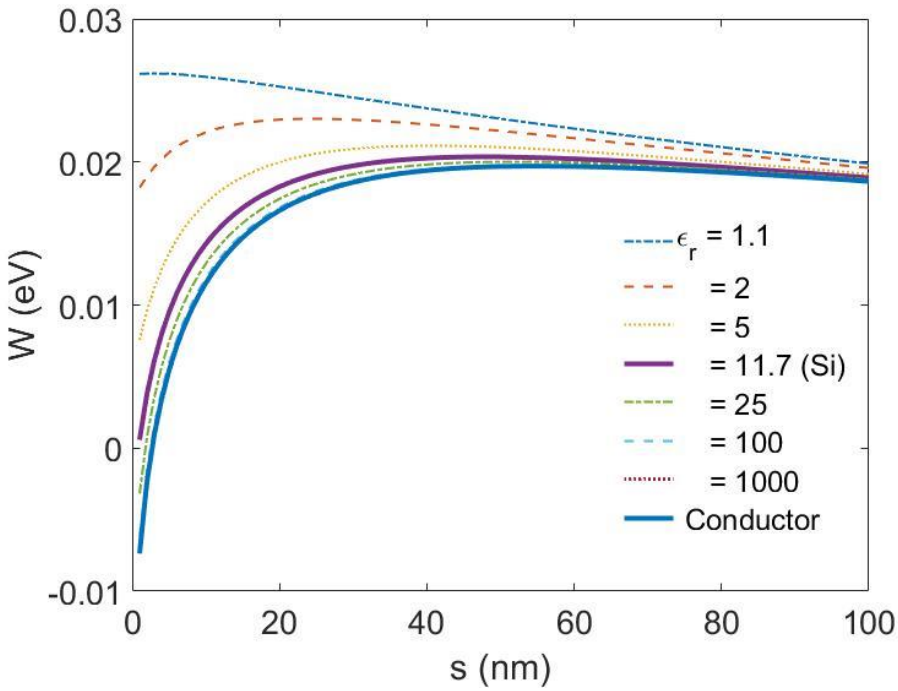

Figure 3.6 W excluding self-energy, as a function of s for the two-dielectric particle system, with $R = 250\,\text{nm}$, $r = 10\,\text{nm}$, $Q = +5e$ and $q = +e$. (dielectric constant ϵ_r : 1.1–1000) The results of W are compared with the W of the charge two conducting particles.

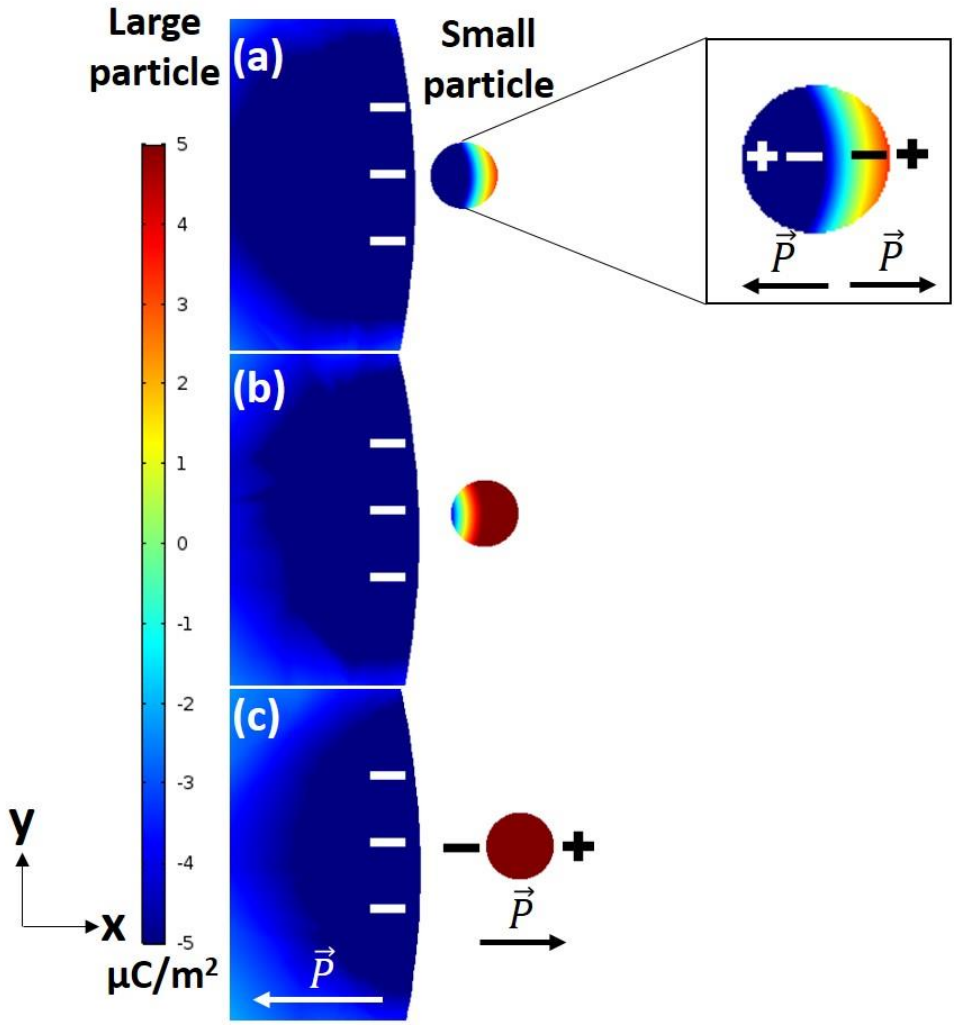

Figure 3.7 x−direction polarization P_x of the two−dielectric particle system ($\epsilon_r = 11.7$, $R = 250$ nm, $Q = +5e$; $r = 10$ nm, $q = +e$), with representative s of (a) 5, (b) 10, and (c) 20 nm. The color legend indicates the magnitude of the polarization. The sign of polarization means the direction relative to the x−direction.

3.3.4 Comparison of analytical and numerical methods

Finally, in order to confirm the validity and accuracy of the numerical method, FEM, the error was investigated from the analytical method, capacitance coefficients method. The error equation used is given by:

$$(error)\ (\%) = \frac{W_{num} - W_{ana}}{W_{ana}} \times 100 \qquad (36)$$

where W_{num} and W_{ana} represent the calculated electrostatic potential energy by numerical method, FEM and analytical method, capacitance coefficients method, respectively. As shown in the Equation (36), the analytical method was used as basis for error calculation.

Figure 3.8 shows the error of calculated W_{num} by FEM as a function of s for various conditions. For all given s and conditions, the error values are located between -0.03% and -0.04% in our FEM settings used: the negative sign means W_{num} is always smaller than W_{ana}. Therefore, the error values appeared to be negligible, and it was confirmed that numerical method FEM setup we used was sufficiently valid and accurate.

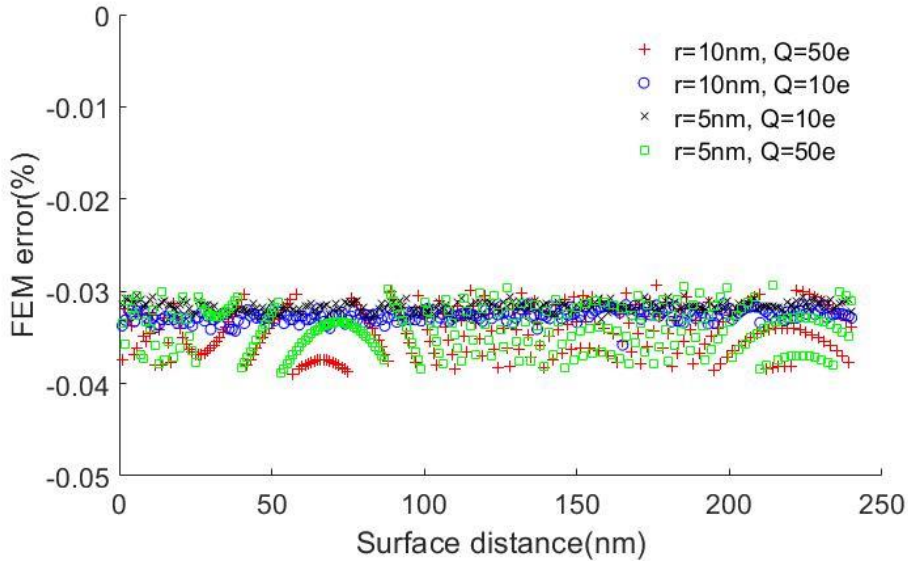

Figure 3.8 FEM error (%) as a function of surface distance (s) for all combinations of $r = 5,\ 10\ \mathrm{nm}$ and $Q = +10e,\ +50e$. The other parameters are $R = 250\ \mathrm{nm}$ and $q = +e$.

3.4. Conclusion

In this chapter, using capacitance coefficients and FEM, we investigated the electrostatic potential energy of two-particle systems and the physical origin of the electrostatic interaction of CNPs. When the large and small CNPs have opposite charges, electrostatic interparticle interaction is always attractive. The electrostatic potential energy, W, more sharply decreases as s decreases compared with the $W_{monopole}$ of the two oppositely charged point particles. In the case the two CNPs have like charges, with increasing s, W rapidly increases and then slowly decreases. Herein, the transition separation distance s^* was newly observed. The s^* indicates that interparticle interaction is attractive when s is less than s^* and repulsive when s is greater than s^*, which contrasts with the repulsive monopole interaction between point particles with like charges.

The value of s^* is determined by many parameters. In this chapter, the results generally show a tendency to increase as the charge ratio Q/q value decreases, the radius of the large particle R increases, and the dielectric constant ϵ_r value increases and approaches the conductor.

The physical origin of these electrostatic interaction is the

surface charge signs (conductors) or direction of polarization vectors (dielectrics) of adjacent areas of particles. When $s < s^*$, so the interparticle interaction is attractive, the adjacent areas have opposite charge signs or the polarization vectors have same direction. When $s > s^*$, so the particles are repulsive, the adjacent areas have same charge signs or the polarization vectors have opposite direction.

Chapter 4. Effects of electrostatic interaction on the formation of a particle depletion zone

4.1. Introduction

A previous study observed the microstructural evolution of charged Si nanoparticles grown via CVD on a glass substrate located in a low−temperature zone of 500℃. [21, pp.245−248] Figure 4.1(a) shows a field−emission scanning electron microscopy (FESEM) image of a large particle and a particle depletion zone; small Si particles occur outside the particle depletion zone. Figure 4.1(b) shows a magnified image of Figure 4.1(a). Electrostatic interactions between CNPs appear to play a crucial role in the structural evolution of the system, which consists of a large CNP and many small CNPs at low temperatures. The physical mechanism underlying the formation of the particle depletion zone around the large CNP during the deposition of numerous small CNPs remains unclear.

The aim of this chapter was to investigate the underlying physical mechanism of the formation and structural evolution of a particle depletion zone around a large CNP during the low-temperature CVD of Si. We used a system consisting of many small CNPs and a large CNP as a particle model. We calculated the electrostatic interactions between CNPs using the methods introduced in Chapter 3. We performed a kinetic Monte Carlo (kMC) simulation to elucidate the dynamics of the multi-CNP system. Through these processes, we examined the role of electrostatic interactions between CNPs in the formation of the particle depletion zone (Figure 4.1) and the structural evolution of the zone.

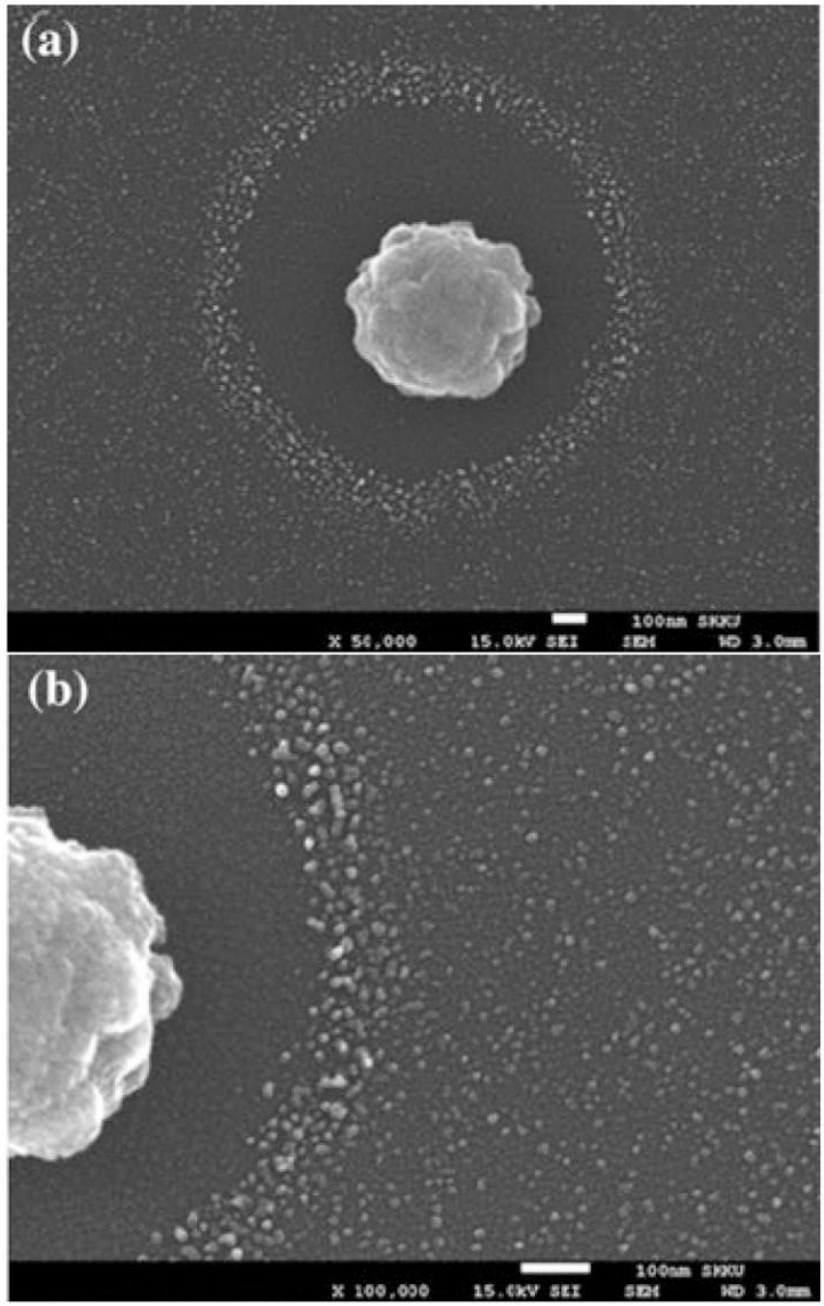

Figure 4.1 Field-emission scanning electron microscopy images of Si microstructures after the 24 h chemical vapor deposition of charged Si nanoparticles on a glass substrate located in a low-temperature zone of 500℃. For the first 5 mins, an AC bias of ±50V at 1 Hz was applied to the glass substrate holder. The flow rates of He-diluted SiH_4 (10% SiH_4 – 90% He), H_2 and N_2 were 11, 50, and 300 sccm, respectively. (b) A higher-magnification image of (a); the scale bar is 100 nm. [21, p. 247]

4.2. Computational Details

4.2.1 kMC simulation

We performed kMC simulations to examine the aggregation dynamics of the CNP system, which consists of a large CNP and many small CNPs. Owing to electrostatic interactions between CNPs, a characteristic microstructure was formed around the large CNP fixed at the origin. The electrostatic energies of the CNPs were obtained through the methods used in chapter 3. The CNPs were modeled as spheres. To improve computational efficiency, we considered the angular symmetry of the distribution of the small CNPs around the large CNP. Simulations were performed in a two-dimensional domain, with the side length of the boundary square as 8R. The kMC simulation procedures were as follows:

1. Small CNPs with radius r_0 and charge $\pm q$ were initially generated at random positions outside the large particle with radius R and charge Q.

2. The trial displacement $\vec{d}$ of a randomly picked small CNP of radius r relative to its center was $\vec{d} = (d\cos\theta, d\sin\theta)$, where

d is the displacement magnitude, and θ is a uniformly distributed random variable between 0 and 2π.

We assumed that when two small CNPs of charges q_i and radii r_i $(i = 1,2)$ were in contact $(s \leq 0)$, they quickly coalesced into a spherical particle; therefore, the charge and radius of the coalesced particle become $q = q_1 + q_2$ and $r = (r_1^3 + r_2^3)^{1/3}$ $(r > r_0)$, respectively.

The trial displacement magnitude d of a particle with radius r is related to the trial time step $\Delta t = d^2/12D$, where D is the diffusion coefficient of the particle from Equation (30). For all particles of spherical compact clusters, the relationship between the diffusion coefficient D and radius r of a particle of size n is $D \sim n^{-1/3} \sim V^{-1/3} \sim r^{-1}$, where V is the particle volume. [65] If Δt is inputted into the above relationship, the trial displacement magnitude d for the particle of radius r is derived as $d = d_0(r_0/r)^{1/2}$ where d_0 is the trial displacement magnitude of a particle with radius r_0. For our kMC simulations, we empirically set d_0 to $0.1r_0$. This value is small enough such that systematic errors generated by a finite step size of d do not considerably

affect the particle behavior, and it is large enough such that simulations are computationally efficient. Moreover, we used a characteristic time scale, $\tau_0 = 4r_0^2/D_0$ as a time unit.

3. Move is accepted or rejected based on the Metropolis transition probability $p = \min[1, \exp\left(-\frac{\Delta E}{k_B T}\right)]$, where ΔE is the change in W with trial displacement, k_B is the Boltzmann constant, and T is the temperature of the system. [66]

In order to perform the kMC simulations, we coded the kMC program using the MATLAB R2021b software. [67] In the simulations, we used parameters containing information on attributes of each particle. The parameters are described by a matrix of size $N \times 4$, where the number of rows, N, is the total number of particles in the system and the four columns represent x and y coordinates, a radius, and charge for each particle. During the kMC simulation, the components in this matrix are updated according to the kMC process described above.

4.2.2 Binary classification

During the kMC simulations of the multi-particle system with only electrostatic interactions between the large and small CNPs, the small-unit CNPs near the large particle were attracted to and coalesced with it. In the final discrimination plot, red dots and blue crosses represent the initial positions of small CNPs attracted and not attracted to the large CNP, respectively. To estimate the final discrimination boundary of the small CNPs around the large CNP, we classified the final discrimination using the binary logistic regression method based on machine learning. This method provided the probability of coalescence between small CNPs and the large CNP. Given that s affects the final discrimination, the method included one predictor s and the response variable $X(s)$, which represented the final discrimination of the small CNPs. The $X(s)$ values are defined as follows:

$$X(s) = \begin{cases} 0, & (if\ a\ small\ CNP\ coalesces \\ & with\ the\ large\ CNP) \\ 1, & (otherwise) \end{cases} \quad (37)$$

A sigmoid function, $S(w_0 + w_1 s)$, was used to express the probability that $X = 1$, which is expressed by

$$P(X=1) = 1 - \mathrm{P}(\mathrm{X}=0) = \frac{1}{1+\exp\left(-(w_0 + w_1 s)\right)} \qquad (38)$$

where w_0 and w_1 are regression intercept and coefficients for s, respectively. To obtain the values of w_0 and w_1 through the binary logistic regression method, we used the sklearn.linear_model.LogisticRegression class in the Scikit-learn module, a machine learning module. [68] The discrimination boundary is estimated as the separation distance $s = -w_0/w_1$, where $P(X=1) = P(X=0) = 0.5$.

4.3. Results and discussions

4.3.1 kMC simulation of two-particle systems with large and small CNPs

To explain the experimental observation of the CNP depletion zone during CVD (Figure 4.1), we need to consider a multi-CNP system consisting of one large CNP and numerous small CNPs. Using the above electrostatic interparticle interaction energies obtained from methods in chapter 3, we simulated the dynamics of the multi-CNP system. All simulations describe the structural

evolution of the system before the small CNPs reside on the substrate.

Before considering complicated systems with numerous small CNPs, we simulated the dynamics of simplified systems with only electrostatic interactions between the large and small CNPs using the kMC method. Figure 4.2(a) shows snapshots of the kMC simulation results at different simulation times (τ_0) for a system with three representative small CNPs. The temperature T was set to 773 K, which corresponds to the temperature around the deposition area. The centered black circle in Figure 4.2 represents the large CNP ($R = 250\ \mathrm{nm}$ and $Q = +5e$). The green dots in Figure 4.2(a) represent the positions of small CNPs ($r = 10\ \mathrm{nm}$ and $q = +e$) at each simulation time. The black lines attached to the green dots in Figure 4.2(a) denote the trajectory of each particle. The outer dashed circle in Figure 4.2 represents the domain boundary of the kMC simulation. A total kMC sweep includes kMC steps of $N = 10^5$, corresponding to $20.8\tau_0$ in the time scale. When the small CNP touches the large CNP or the outer domain boundary, the kMC simulation stops at earlier steps. The small CNP nearest to the large CNP is attracted to the large CNP and coalesces with it; the other two CNPs [Figure 4.2(a)] remain outside the large particle or touch the outer domain boundary. The coalescence features are

presented in the final discrimination result [Figure 4.2(b)], in which the red dot and blue cross represent the initial positions of small CNPs attracted and not attracted to the large CNP, respectively. The results demonstrate that the small CNPs near the large CNP have a strong tendency to coalesce with it.

To examine the coalescence features of systems with a sufficiently large number of small CNPs and their Q-dependent tendencies, we simulated a system with only electrostatic interactions between 10^4 small-unit CNPs and a large CNP at T = 773 K using the kMC method. The charges of the large CNP were set to $Q = +e$ [Figure 4.3(a)], $+50e$ [Figure 4.3(b)], and $+100e$ [Figure 4.3(c)]. The initial positions of CNPs within the circular area were randomly selected; the circular area, with the large black CNP at its center, had a radius of 650 nm. The outer domain boundary, denoted by the outer dashed circle, had a radius of 750 nm. Except for the Q value and number of small particles, the other simulation conditions were the same as those of the simulation depicted in Figure 4.2.

Figure 4.3 shows the Q-dependent final discrimination results of the system with only electrostatic interactions between 10^4 small-unit CNPs and a large CNP; the red dots and blue crosses represent the initial positions of the small CNPs attracted and not

attracted to the large CNP until the end of a kMC sweep, respectively. As shown in Figure 4.3, most of the small CNPs near the large CNP are attracted to it, in contrast to those away from it. From the viewpoint of microstructure evolution, the attracted small-unit CNPs coalesce with the large CNP. Figure 4.3 shows the depletion of small CNPs near the large particle. The small CNPs far from the large CNP appear to be located outside or near the discrimination boundary; this result was obtained from binary logistic regression calculations based on machine learning. The discrimination boundary thickness, defined as the radial difference between the discrimination boundary and surface of the large CNP, decreases with increasing Q. At a Q of $+e$, $+50e$, and $+100e$, the discrimination boundary thickness is 197.6 nm [Figure 4.3(a)], 93.5 nm [Figure 4.3(b)], and 32.3 nm [Figure 4.3(c)], respectively. This trend is consistent with the decrease in s^* with increasing Q (Figure 3.3).

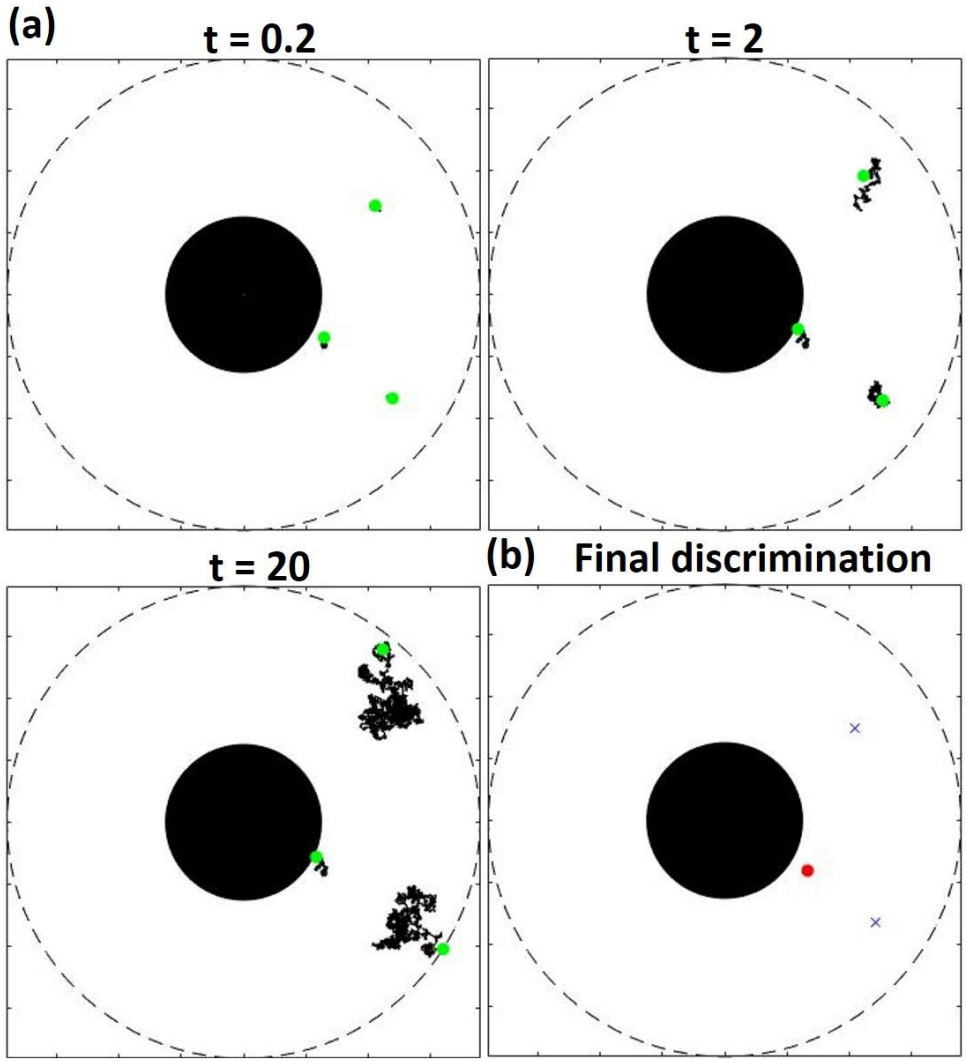

Figure 4.2 (a) kMC simulation results: Snapshots and trajectories of three small particles interacting with a large particle of the same charge at three simulation times (τ_0). The centered black circle represents the large particle, while the green dots and black lines represent the positions of small unit particles and their trajectories at each simulation time, respectively. (b) Final discrimination of the three small particles after a kMC sweep. The red dot and blue cross represent the initial positions of small particles attracted and not attracted to the large particle, respectively. The dashed circle represents the domain boundary of the kMC simulation. The simulation parameters are $R = 250\ \text{nm}$, $r = 10\ \text{nm}$, $Q = +5e$, $q = +e$, and $T = 773\ \text{K}$, and the dimensions of each box are $1500\ \text{nm} \times 1500\ \text{nm}$.

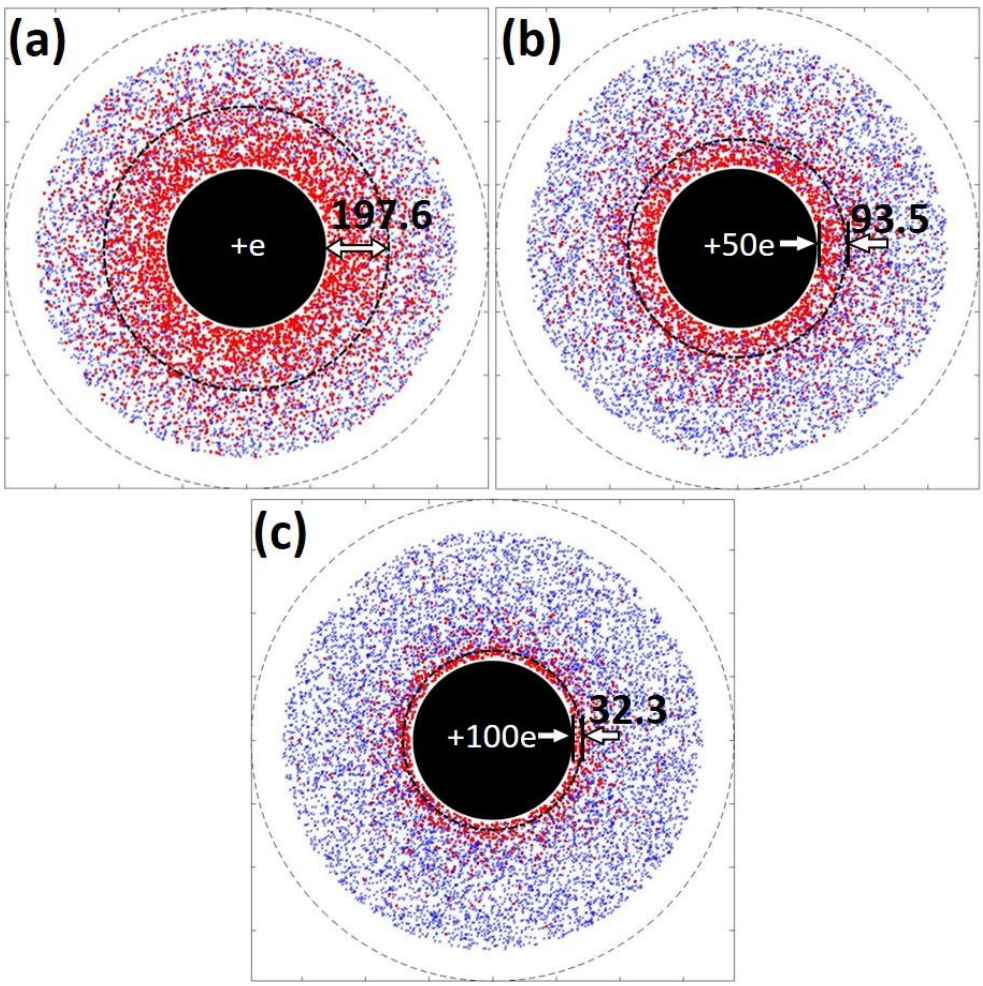

Figure 4.3 kMC simulation results: Charge−dependent variation in the final discrimination results of 10^4 small particles interacting with a large particle of the same charge, for $Q =$ (a) $+e$, (b) $+50e$, and (c) $+100e$. The centered black circle represents the large particle; the red dot and blue cross represent the initial positions of small particles attracted and not attracted to the large particle, respectively; the inner dashed circle denotes the discrimination boundary between the small particles attracted and not attracted to the large particle; the numbers denote the thickness of the discrimination boundary (nm); and the outer dashed circle represents the domain boundary of kMC simulation. The simulation parameters are $R = 250\ \text{nm}$, $q = +e$, $r = 10\ \text{nm}$, and $T = 773\ \text{K}$, and the dimensions of each box are $1500\ \text{nm} \times 1500\ \text{nm}$.

4.3.2 kMC simulation of multi−particle systems with a large CNP and many small CNPs

In the simulations depicted in Figures 4.2 and 4.3, we considered the electrostatic interaction between the small and large CNPs to obtain characteristic features of the dynamics of the two−CNP system. However, the experimental situation was more complicated, and we needed to consider the electrostatic interactions among all CNPs. For this, we simulated systems with one large CNP and numerous small CNPs using the kMC method, considering the electrostatic interactions and coalescence among all particles. A large CNP of $R = 250\ \mathrm{nm}$ was fixed at the center. Five thousand small particles were randomly positioned in a square of $1500\ \mathrm{nm} \times 1500\ \mathrm{nm}$ and outside the large CNP without any overlap. To realistically model the multi−CNP system, we considered the coexistence of positively and negatively charged small−unit nanopaticles. The initial ratio of positively charged small particles to the total small CNPs (γ_+) is expressed as $\gamma_+ = N_0^+/N_0$, where N_0 is the initial value of the total number of small CNPs (N), and N_0^+ is the initial value of the number of the positively charged small particles (N^+). The initial Q_0 and q_0 were $+5e$ and $\pm 5e$, respectively. During the kMC simulations, coalescence of particles

causes a change in Q, q, and r, N, and N^+; however, R is fixed, as the change caused by coalescence is negligible.

Figure 4.4 shows snapshots of kMC simulations at different simulation times for three representative initial values of γ_+. The black area and white circles represent the substrate and particles, respectively. The thickness of the particle depletion zone near the large particle increases with increasing γ_+ (from 0.5 to 0.7 to 0.9). In particular, at $\gamma_+ = 0.5$, the particle depletion zone does not expand over time, whereas at $\gamma_+ = 0.7$ and 0.9, it does expand over time [see Figures 4.4(b) and (c)].

The value of Q/q significantly influences the electrostatic interaction between large and small CNPs and is thus expected to also influence the particle depletion zone depicted in Figure 4.4. Therefore, we investigated the change in $Q/|q_0|$ over simulation time t. Figure 4.5 shows the results of $Q/|q_0|$ for each value of the representative γ_+. The absolute value of the initial $|q_0| = +5e$ was used as the denominator because the q of each small particle varied during the simulation.

At $\gamma_+ = 0.5$ [Figures 4.4(a) and 4.5], the numbers of positively and negatively charged CNPs are balanced. Moreover, small particles with unlike charges continuously coalescence, indicated by the steady increase in the size of small particles over time [Figure

4.4(a)]. The change in value and sign of $Q/|q_0|$ in Figure 4.5 indicates that the large and small CNPs also steadily coalesce. In addition, the large CNP considerably coalesces with nearby small CNPs, as indicated by the fluctuation in the value of $Q/|q_0|$ until $t = 100\tau_0$. The coalescence process continues, and $Q/|q_0|$ reaches a minimum (-10) at $t = 480\tau_0$. The positively charged small particles are more attracted to the large particle because of its accumulated negative charge Q, and the value of $Q/|q_0|$ becomes 0 at $t = 800\tau_0$. Therefore, the accumulation of charges is weakened, and the value of $Q/|q_0|$ becomes near−zero. This results in a weak electrostatic interaction between the large and small CNPs outside the attraction boundary; thus, only the small CNPs within the attraction boundary of the large CNP coalesce with it. This explains the formation of a smaller particle depletion zone at $\gamma_+ = 0.5$ than at $\gamma_+ = 0.7, 0.9$ [see Figure 4.4].

At $\gamma_+ = 0.7$ [Figures 4.4(b) and 4.5], the negatively charged small particles, which account for 30% of the total particles, coalesce with positively charged particles before $t = 100\tau_0$, and only positively charged CNPs are left. After $t = 100\tau_0$, small CNPs hardly coalesce, as indicated by the almost constant size of the small particles over time shown in Figure 4.4(b). As shown in Figure 4.5, the value of $Q/|q_0|$ fluctuates between 20 and 30 before $t = 50\tau_0$

and steadily increases from 21 to 22 after $t = 80\tau_0$. This result indicates that small CNPs actively coalesce with the large CNP in the initial stage, but rarely after $t = 80\tau_0$. It also shows that Q accumulates until $t = 80\tau_0$, and a particle depletion zone simultaneously forms and then gradually expands because of electrostatic repulsion between the positively charged large and small particles.

At γ_+ = 0.9 [Figures 4.4(c) and 4.5], the negatively charged small particles, which account for 10% of the total particles, coalesce with the positively charged particles before $t = 50\tau_0$, earlier than $t = 80\tau_0$ for γ_+ = 0.7, and only positively charged CNPs are left. This behavior is similar to that depicted in Figure 4.4(b). However, the small CNPs are smaller, because fewer of these CNPs coalesce compared with the cases at higher values of γ_+. Figure 4.5 shows that the value of $Q/|q_0|$ increases sharply to 55 before $t = 50\tau_0$ and then remains constant. The formation and expansion processes of the particle depletion zone are similar to those at γ_+ = 0.7. However, the depletion zone at γ_+ = 0.9 is wider than those at γ_+ = 0.5 and 0.7 [Figures 4.4(a) and (b)], even though the t at γ_+ = 0.9 ($600\tau_0$) is lower than that at γ_+ = 0.7 ($t = 1050\tau_0$). Because of a more severe charge imbalance at γ_+ = 0.9, the accumulated positive Q on the large CNP was

approximately three times that at $\gamma_+ = 0.7$, which explains the wider depletion zone at $\gamma_+ = 0.9$.

According to the simulation results, the particle depletion zone is formed over two stages, both of which are attributable to the electrostatic interaction between large and small CNPs. In stage 1, the large CNP coalesces with nearby small CNPs having the same charge, which results in charge accumulation on the large CNP. Q becomes larger, as the charge imbalance among the initial small-unit CNPs is more severe (Figure 4.5). In stage 2, the large CNP with accumulated charge Q repels other small particles with the same charge, which expands the particle depletion zone. Therefore, the farther γ_+ is away from 0.5, the wider the particle depletion zone formed.

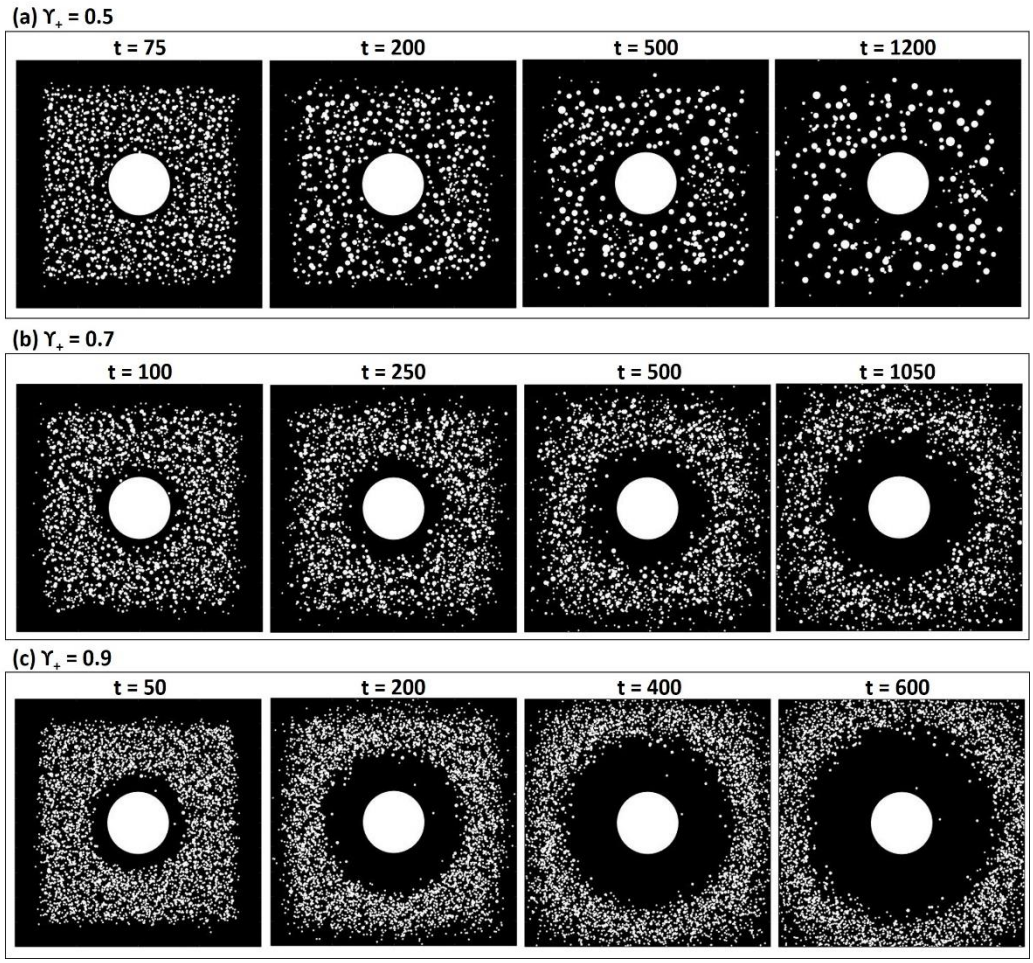

Figure 4.4 kMC simulation results: Snapshots of systems with small CNPs and a large CNP at different simulation times (τ_0). Positively and negatively charged small particles coexist. Three values of γ_+were considered: (a) 0.5, (b) 0.7, and (c) 0.9. Five thousand small CNPs were randomly positioned in a square of $1500\ \text{nm} \times 1500\ \text{nm}$ and outside the large CNP without any overlap. The white circles represent the position and size of the CNPs. The initial parameters for the simulation are $Q_0 = +5e, q_0 = \pm 5e, R = 250\ \text{nm}$, $r_0 = 3\ \text{nm}$, and $T = 773\ \text{K}$, and the dimensions of each box are $2000\ \text{nm} \times 2000\ \text{nm}$.

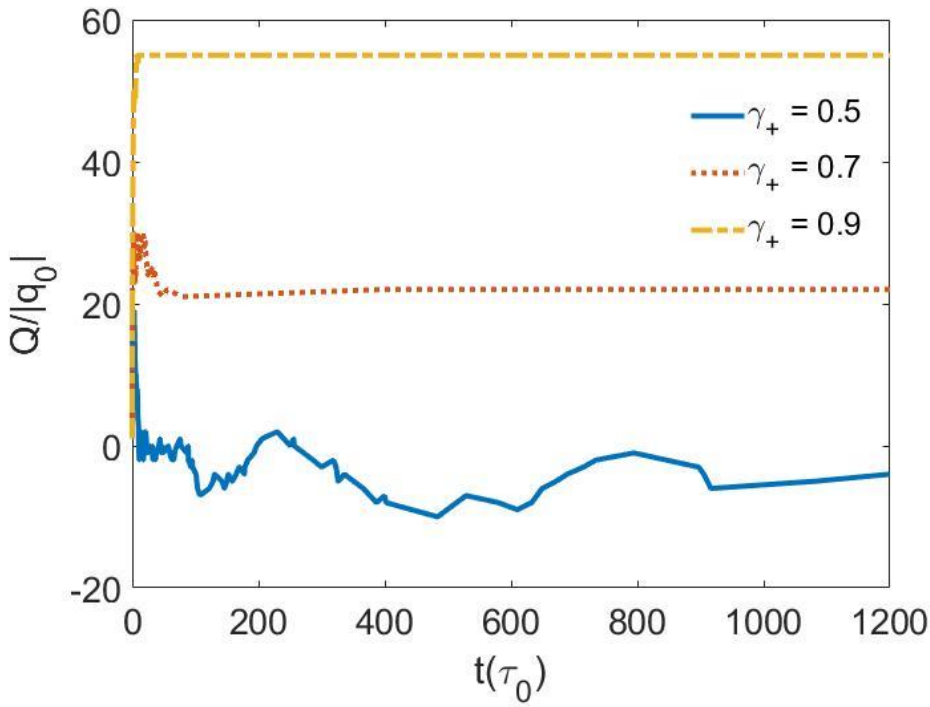

Figure 4.5 Charge ratio ($Q/|q_0|$) as a function of t (τ_0), obtained from the kMC simulation results in Figure 4.4, for γ_+ = 0.5–0.9.

4.3.3 Characteristic time scale and formation of a band near the depletion zone

Herein we discuss the characteristic time scale τ_0 and the diffusion coefficients D_0 in the kMC simulations. Figures 4.4(b) and (c) showed the kMC simulation results similar to the experimental result in Figure 4.1 when $t \sim 10^3\tau_0$. Since the experiment time in Fig. 4.1 was 24 hours, the time scale of τ_0 is estimated to be around 10^2 s. However, considering that the experiment time includes the formation of the large particle which is not considered in the simulations, the time scale of τ_0 is likely to be around 10^1 s. Assuming $\tau_0 = 10$ s, the diffusion coefficient of unit CNP D_0 is $3.6\,\mathrm{nm^2/s}$ from equation $\tau_0 = 4r_0^2/D_0$. For comparison, the theoretical diffusion coefficient is given by $D_{\mathrm{th}} = k_B T/6\pi\mu r$ from the Stokes–Einstein value of the molecular self–diffusion coefficient where μ is the solution viscosity. [69] In our experimental condition, the solution is gaseous phase with He–diluted SiH_4, H_2 and N_2. Thus, assuming the gaseous viscosity $\mu = 10^{-6}\,Pa\cdot s$, theoretical diffusion coefficients $D_{0,\mathrm{th}}$ is calculated by $1.23 \times 10^8 \mathrm{nm^2/s}$, which is 8 orders of magnitude larger than D_0. Note that gaseous viscosity is ranged from $10^{-6} - 10^{-5}$ and liquid viscosity is ranged from $10^{-4} - 10^{0}$. [70,71]

Table 4.1 shows the experimental diffusion coefficients D_{exp} and theoretical diffusion coefficients ($D_{\mathrm{th}} = k_B T/6\pi\mu r$ in experimental studies or D_{th} set in simulation studies) from nanoparticle diffusion studies. [59,65,72−75] It can be seen that D_{exp} is reported to be 5−10 orders of magnitude smaller than D_{th}. This phenomenon is called hindered nanoparticle diffusion or nanoparticle diffusion hinderances. Various hypotheses for the diffusion hinderances were suggested including increased drag force near the window surface, [73,76] surface roughness, [73] highly viscous ordered liquid layers, [73,74] strong NP−window interactions, [73,74,77] and electrostatically−induced surface diffusion. [72] It seems clear that the diffusion hinderance effect is due to close distance to the surface, however, the accurate mechanism causing the decreased mobility of nanoparticle still remains unclear. It is expected that the time scale and diffusion coefficients will be predicted more accurately through more studies.

Additionally, Figures 4.4(b) and (c) also showed the formation of a band near the outer boundary of the depletion zone, where particle sizes are larger in comparison with those in the farther region from the center of the large particle. This feature was also observed in the experimental result of Figure 4.1. In order to explain this behavior, we investigated the final particle size

distribution for the experimental result in Figure 4.1(b) using ImageJ software [79]. Since the particle sizes near the outer boundary of the depletion zone are larger than those in the farther region outside the depletion zone, we divided the region of Figure 4.1(b) into two parts, the one (Part 1) containing the boundary and the other (Part 2) [see Figure 4.6(a)]. Here, the particle size distribution results in Figure 4.6(b) are normalized to represent the probability. As shown in Figure 4.6(b), most of particle sizes range from 5 nm to 20 nm in diameter. Some particle sizes exceeding 20 nm in diameter are also seen in Part 1. Regarding this phenomenon, it is noted that, after charge accumulation on the large CNP, many small CNPs are repelled from the large CNP, with their electrostatic energy decreasing with the inter-particle distance between large and small CNPs, as shown in Figures 4.4(b) and (c). The density of small CNPs near the outer boundary of the depletion zone becomes higher than that in the farther region outside the depletion zone. Thereby, the particle sizes increase by the coalescence of CNPs in the high particle density region near the outer boundary of the depletion zone. This well explains the formation of a band near the outer boundary of the depletion zone, where particle sizes are larger in comparison with those in the farther region from the center of the large particle. (see Figure 4.6)

Table 4.1 Experimental diffusion coefficients D_{exp} and theoretical diffusion coefficients: $D_{\mathrm{th}} = k_B T/6\pi\mu r$ in experimental studies or D_{th} set in simulation studies. The diffusion coefficients are expressed in units of nm^2/s.

	D_{exp}	D_{th}	Ref.
Our study	3.6	1.23×10^8	
Experiment studies	$0.1 - 7$	1.63×10^7	[72]
	0.048	$\sim 10^8$	[73]
	7	4.1×10^5	[74]
	$0.165 - 0.268$	$\sim 10^8$	[75], μ from [78]
Simulation studies	–	4×10^7	[59]
	–	$10^2 - 10^6$	[65]

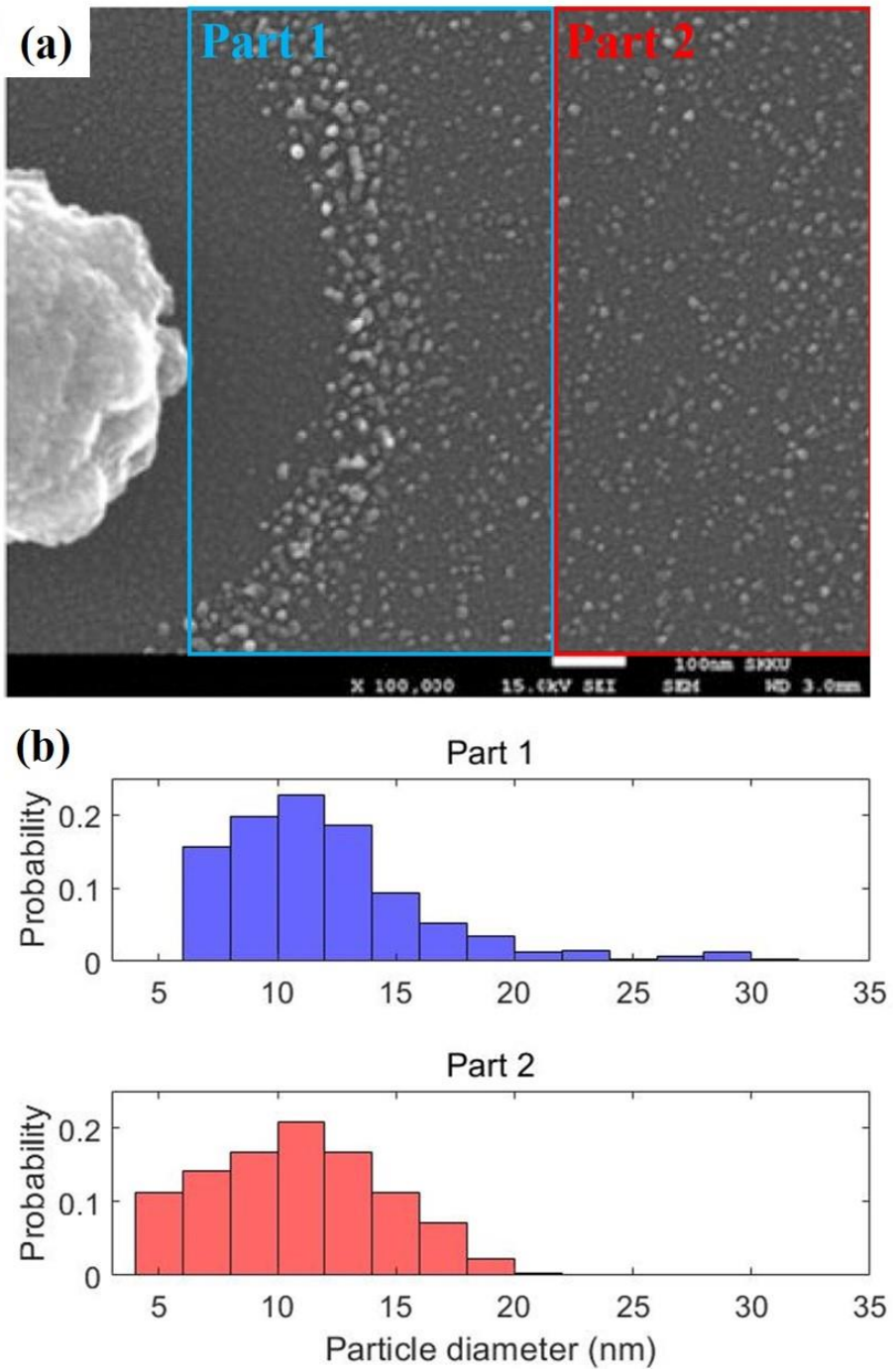

Figure 4.6 Particle size distributions in a higher-magnification image of Figure 4.1(a). In (a), the particle zones are divided into two parts (Part 1 and Part 2). In (b), the particle size distribution results are normalized to represent the probability.

4.4. Conclusion

In this chapter, using kMC simulations, we investigated the dynamics of small CNPs in the presence of a large CNP, respectively. The results of kMC simulation, in which all small particles were assumed to be electrically charged, showed that a particle depletion zone was formed around the large particle in two stages. In the first stage, a relatively small particle depletion zone was formed around the large CNP owing to its attraction and coalescence with nearby small particles having the same charge. Charges were accumulated on the large CNP during this process. In the second stage, the particle depletion zone was expanded owing to the repulsion of distant small particles from the large particle because of the accumulated charge. Further analysis showed that the imbalance between the numbers of positively and negatively charged small particles was the most important factor influencing the formation of the particle depletion zone. The formation and expansion of the zone at a γ_+ close to 1 were more intense than those at other γ_+ values. The results showed that kMC based on the electrostatic potential energy calculation is a powerful tool for studying non-classical crystallization with CNPs as building blocks.

Chapter 5. Effects of electrostatic interaction on abnormal growth of deposited particles

5.1. Introduction

An additional (puzzling) phenomenon is not explained by the classical crystallization theory. Kumomi et al. [53–55] reported an unusual feature during CVD of silicon (Si) in a Si–Cl–H system (Figure 5.1). Si deposition and etching proceeded simultaneously when Si was selectively deposited on SiN_x patterned on SiO_2 [55]. Figure 5.1 shows the microstructural evolution of substrate–deposited Si particles at three deposition times. At 480 s [Figure 5.1(a)], many fine Si particles were selectively deposited on $4 \times 4\ \mu m^2$ square portions of SiN_x (x = 0.56). At 720 s [Figure 5.1(b)], one large particle was apparent; the fine particles had disappeared (because they were etched). Notably, at 960 s [Figure 5.1(c)], abnormal growth of one large particle was observed in most SiN_x specimens; vacancies attributable to complete particle

etch removal were observed in only a few SiN_x specimens. Large particle growth is not a feature of classical crystal growth theory, in which the units of both deposition and etching are atomic. Hwang [21,80] employed a theory involving CNPs to explain such abnormal growth, assuming that CNPs nucleated in the gas phase became the building blocks. In such a case, gaseous atomic Si is depleted by gas-phase nucleation of Si nanoparticles; the depleted gas drives the etching of Si nanoparticles by atomic units. Thereby, the units of deposition are CNPs, but the units of etching are atomic. However, why did only one particle grow abnormally? Hwang [80] suggested that electrostatic interactions among CNPs play crucial roles in abnormal growth. However, the physical mechanism underlying such growth during Si CVD remains unclear.

Here, we theoretically explore that physical mechanism. We consider CNPs generated in the gas phase. We performed kinetic Monte Carlo (kMC) simulations to investigate the growth behaviors of a three-dimensional multi-CNP system based on the electrostatic potential energy among CNPs. We explored the effects of electrostatic interactions and other growth parameters on the abnormal growth of deposited particles.

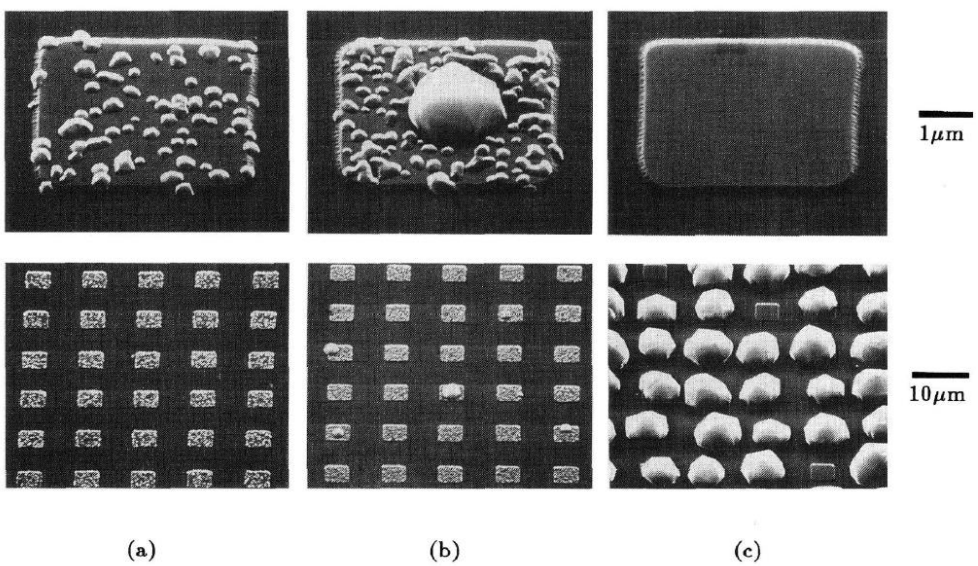

Figure 5.1 Scanning electron microscopy (SEM) images of Si-deposited surfaces at three deposition times. $4 \times 4\ \mu m^2$ specimens of SiN_x (x = 0.56) are placed on an SiO_2 surface. The images show magnifications of one of the SiN_x specimens presented below. (a) At 480 s, many fine nanoparticles are selectively deposited on all SiN_x specimens. (b) At 720 s, very large nanoparticle is evident among the fine nanoparticles on a few SiN_x specimens. (c) At 960 s, most SiN_x specimens are covered with single large nanoparticles, although some lack nanoparticles. (adapted from ref [55])

5.2. Computational Details

We performed kMC simulations to examine the growth dynamics of many−CNP systems. The electrostatic energies of the systems for the simulation were obtained by calculating the capacitance coefficients used in Chapter 3. [see Equations (16), (31)−(34)]. We approximated the values of C_{ij} (to an accuracy of 10^{-7} via finite summation of the infinite series shown in Equations (31)−(33). We used the truncated form of the electrostatic potential energy W to improve computational efficiency as follows:

$$W_{\mathrm{cut}}(c) = \begin{cases} W(c) - W(c_{\mathrm{cut}}) & c \le c_{\mathrm{cut}} \\ 0 & c > c_{\mathrm{cut}} \end{cases} \qquad (39)$$

The cutoff distance c_{cut} was set to $5(r_1 + r_2)$. Thus, only particles that lie closer than $c_{\mathrm{cut}} = 5(r_1 + r_2)$ engage in mutual electrostatic interactions.

The CNPs were modeled as spheres. Simulations were performed in a three−dimensional cubic domain with side lengths of L. The kMC simulation procedures were as follows:

1. CNPs of radius r_0 and charge $\pm q_0$ were initially generated at random positions (without overlaps) within the simulation domain. The initial particle number was $N_0 = \eta L^3 / \frac{4\pi}{3} r_0^3$, and

the particle volume fraction η (this is the fraction of the volume occupied by CNPs in the gas phase). The particle volume fraction η was maintained constant by generating new CNPs with radii r_0 in the gas phase whenever the value assigned to η fell. Note that all particles in contact with the substrate were considered to be deposited (their positions were thus fixed). Only particles in the gas phase moved during simulation.

2. We next selected one random CNP in the gas phase. The trial displacement relative to the center thereof was $\vec{d} = d(\sin\phi\cos\theta, \sin\phi\sin\theta, \cos\phi)$ where d is the displacement magnitude. The polar angle $\phi = \arccos(2u - 1)$ and the azimuthal angle $\theta = 2\pi v$ were selected from the uniformly distributed random variables u and v, respectively; these ranged from 0 to 1.

We assumed that when two CNPs with charges q_i, radii r_i, and center positions $\overrightarrow{R_i}\,(i = 1,2)$ came into contact ($c \le r_1 + r_2$), they quickly coalesced into a spherical particle; the charge and radius of which became $q = q_1 + q_2$ and $r = (r_1^3 + r_2^3)^{1/3}$ respectively. The position $\vec{R}$ of a coalesced

particle is determined by the center of mass of the two CNPs when both are either in the gas phase or deposited: $\vec{R} = \left(\vec{R}_1 \mathrm{r}_1^3 + \vec{R}_2 r_2^3\right)/(r_1^3 + r_2^3)$. When one $(i = 1)$ is deposited and the other $(i = 2)$ is in the gas phase, the position $\vec{R}$ of the coalesced particle is the same as that of the deposited particle: $\vec{R} = \vec{R}_1$.

During a trial time step $\Delta t = d^2/12D$, where D is the diffusion coefficient of a particle of radius r, the trial displacement magnitude d was $d = d_0(r_0/r)^{1/2}$, wherein d_0 is the trial displacement magnitude of a particle of radius r_0. [42] Note that the relationship between the diffusion coefficient D and the radius r of a particle is $D \sim r^{-1}$. [65] d_0 was empirically set to $0.1r_0$ and a characteristic time scale $\tau_0 = 4r_0^2/D_0$ served as the time unit during simulation. [42,59,65,81]

3. Move was accepted or rejected based on the Glauber transition probability $p = \left[1 + \exp\left(\frac{\Delta E}{k_B T}\right)\right]^{-1}$ where ΔE is the change in the potential energy W with the trial

displacement, k_B is the Boltzmann constant, and T is the temperature. [60]

Turning to etching by a gaseous atmosphere depleted of atomic Si, it was necessary to add an etching factor that reduced the particle size. The etching rate is proportional to the surface area $A = 4\pi r^2$ of a CNP of radius r. The rate at which the particle volume decreases is $dV/dt = -k_{etch}A = -k_{etch}(4\pi r^2)$ where k_{etch} is an etching rate constant. Given $V = 4\pi r^3/3$, we obtain an etching equation: $dr/dt = -k_{etch}$. We also considered the gas-flow effect during CVD; we assumed a steady gas flow along the x direction. All particles in the gaseous phase moved with velocity v_{flow} along the x direction. Therefore, the x coordinates of all gaseous CNPs increase by $\Delta x = v_{flow}\Delta t$ at each time step Δt of the simulation.

5.3. Results and Discussions

To explore the experimental observation of the abnormal growth of deposited Si CNPs during CVD, we simulated a system with many CNPs in the gaseous phase. Employing the electrostatic interparticle potential energy obtained from the capacitance coefficients of two conducting spherical CNPs, we used a kMC model to simulate the dynamics of three-dimensional multi-CNP systems. We first considered an important growth parameter, thus the charge sign ratio of the CNPs (γ_+). This was written as $\gamma_+ = N_0^+/N_0$, where N_0 and N_0^+ are the initial numbers of total and positively CNPs. We also considered the volume fraction of CNPs (η) associated with the particle density in the gaseous phase. The particle volume fraction η was written $V_g/(V_s - V_d)$, where V_g, V_s, and V_d are the volumes of the CNPs in the gas phase, the simulation domain and the deposited CNPs respectively. When the value of η became smaller than the initial value (CNPs escaped the domain or engaged in etching), new CNPs of radii r_0 and charges q_0 were generated at random positions in the gas phase. Their charge signs q_0 were positive (negative) with probabilities of γ_+ $(1-\gamma_+)$. In addition, we considered the drift of the gas-phase CNPs with the gas flow velocity v_{flow} along the x-direction.

5.3.1 Effect of the charge−sign CNP ratio

We first performed kMC simulations using CNPs of various charge−sign ratios (γ_+) to investigate γ_+−dependent growth behaviors. Figure 5.2 shows snapshots of the simulations at different times for three values of γ_+, thus = 0.5, 0.6, and 0.7. It is noted that the sign reversal of CNPs does not affect the simulation results due to the charge symmetry of electrostatic energy W including the terms of Q_1^2, Q_1Q_2, and Q_2^2 of the two CNP charges Q_1 and Q_2 [see Equation (16)]. Thereby, the simulation conditions γ_+ and $(1-\gamma_+)$ show the same growth behavior. The $v_{\mathrm{flow}} = 5\,\mathrm{nm}/\tau_0$ for gas drift velocity was held low to accelerate the growth dynamics. The blue and black spheres represent CNPs in the gas phase and deposited CNPs on the substrate (in the xy−plane), respectively. To explore the details, we plotted the radii R_{max} and charges Q_{max} of the largest deposited particles over time. Figure 5.3 shows the R_{max} and Q_{max} for each value of (representative) $\gamma_+ = 0.5 - 0.9$. Although not shown in Figure 5.2, the results for $\gamma_+ = 0.8$ and 0.9 appear in Figure 5.3 (for comparison).

At the $\gamma_+ = 0.5$ of Figure 5.2(a), the numbers of positively and negatively CNPs in the gas phase are balanced. Figure 5.2(a) shows that many small CNPs in the gas phase become deposited on the

substrate around $t = 100\tau_0$ and that one such CNPs grows continuously over time. This mirrors the experimental data; only one CNP grew. Figure 5.3(a) shows the detailed evolution of abnormal deposited CNP growth. The change in $R_{\max}$ at $\gamma_+ = 0.5$ evident in Figure 5.2(a) indicates that a specific CNP grows continuously by coalescing with other CNPs. The drastic increases in γ_+ observed at $t \approx 2500\tau_0$ and $4000\tau_0$ indicate that coalescence with other large deposited CNPs is also in play. When t attains $\sim 9000\tau_0$, $R_{\max}$ becomes saturated near 600 nm, thus the maximum value in the simulation domain. Herein we briefly remark the choice of the cutoff distance c_{cut} set to $5(r_1 + r_2)$. The c_{cut} value was chosen so that the value of $\left(\frac{dW}{dc}\right)_{c=c_{\text{cut}}}$, the electrostatic potential energy gradient at c_{cut}, was small enough not to cause any noticeable simulation errors. To assess the validity of the c_{cut} value set above, we also performed test calculations for the time at which $R_{\max}$ becomes saturated near 600 nm, the maximum value in the simulation domain, for $\gamma_+ = 0.5$ in Figure 5.3(a), using the larger c_{cut} value of $5.5(r_1 + r_2)$. The test calculations showed that the saturation time for $R_{\max}$ changed less than 0.1%. Thus, the c_{cut} value of $5(r_1 + r_2)$ used here is sufficient for the purpose of the present study.

A physical explanation of this abnormal growth becomes apparent on analysis of the $Q_{\max}$ value in Figure 5.3(b) and the electrostatic interactions between the largest deposited CNPs and CNPs in the gas. Figure 5.3(b) shows that the values of $Q_{\max}$ at $\gamma_+ = 0.5$ fluctuate between $-100e$ and $130e$. This indicates that the charges of the deposited CNPs do not accumulate; both positively and negatively CNPs in the gas actively coalesce. In terms of the electrostatic interactions between deposited CNPs and CNPs in the gas phase, we considered two cases: when the charges were unlike and like. In the former case, interactions are always attractive, accelerating the growth of deposited CNPs. Such interactions become stronger as the separation distance s shortens and the numbers of unlike charges increase.

In the latter case (like charges), the electrostatic interactions depend on the separation distance s. CNPs with like charges are attractive when that distance s is smaller than the transition separation distance s^* (which depends on the CNP charges and radii). Chapter 3 and our previous study [42] showed that positive charges are induced on the surface area of the small CNP adjacent to the large CNP, while negative charges are induced on the surface area of the large one adjacent to the small one when they are closer than s^*. Thus, the adjacent areas of the two CNPs have oppositely

induced surface charges, which causes attractive interactions between the two CNPs. Conversely, when the distance exceeds s^*, the CNPs engage in mutual repulsion. Figure 3.4 plots s^* as a function of Q/q for two CNP systems with charges of q and Q, radii of $r = 20$ nm, and $R = 100 - 500$ nm. For any given R, s^* decreases when Q/q increases. Thus, the smaller the charge accumulation of deposited CNPs, the longer the attractive interaction range. Figure 3.4 also shows that for any given Q/q, s^* increases as the radius R of a (large) CNP increases. Thus, larger deposited CNPs tend to engage in attractive interactions with more CNPs (with like charges) in the gas phase, further increasing $R_{\max}$. These interactions of s^* with $Q_{\max}$ and $R_{\max}$ explain the abnormal growth of the largest deposited CNP at $\gamma_+ = 0.5$ well.

At $\gamma_+ = 0.6$ in Figure 5.2(b), the positively CNPs account for 60% of all CNPs; charge is thus imbalanced. Figure 5.2(b) shows that some CNPs from the gas phase become deposited on the substrate around $t = 100\tau_0$, and that further growth of such deposited CNPs is limited, although some do to a certain extent. At the value of $R_{\max}$ at $\gamma_+ = 0.6$ of Figure 5.3(a), the radius of the largest CNP barely exceeds 200 nm. The value of $Q_{\max}$ at $\gamma_+ = 0.6$ of Figure 5.3(b) shows that the charge of the largest deposited CNP gradually increases (with some fluctuations) over time, in contrast

to the behavior noted at $\gamma_+ = 0.5$. Figure 3.4 shows that the values of s^* for systems of two CNPs with $R = 200\ \mathrm{nm}$ and $Q/q = 10^1 - 10^2$ (corresponding to an $R_{\max}$ and a $Q_{\max}$ of the largest deposited CNP at $\gamma_+ = 0.6$ respectively) are much smaller compared to what is apparent at $\gamma_+ = 0.5$. Thus, the largest deposited CNP is associated with a narrower, attractive interaction zone with CNPs of like charge in the gas phase than is the case at $\gamma_+ = 0.5$. Thereby, coalescence of CNPs in the gas phase is activated, at the cost of the growth of a deposited CNP. Figure 5.2(b) shows CNPs with radii of $\sim 100\ \mathrm{nm}$ or larger in the gas phase at $t = 5000\tau_0$ and $15000\tau_0$. Notably, such aggregated gaseous CNPs always appear during the time over which $R_{\max}$ decreases markedly. Representative examples of such time ranges include $t = 2300 - 4700\tau_0$, $5500 - 7500\tau_0$, and $11500 - 13300\tau_0$. Aggregated CNPs move slowly in gas because their radii $\tilde{r}$ are large ($\mathrm{D} \sim 1/\tilde{r}$); residence time in the gas phase is long. The slow diffusion/long residence time in the gas prevent rapid growth of deposited CNPs. These features of CNPs limit the supply of small gaseous CNPs to deposited CNPs. Thus, abnormal growth of deposited CNPs is reduced compared to that at $\gamma_+ = 0.5$.

At $\gamma_+ = 0.7$, positively CNPs account for 70% of all CNPs; sign imbalance is more severe than that at $\gamma_+ = 0.6$. Figure 5.2(c) shows

that the sizes of deposited CNPs are smaller than those at $\gamma_+ = 0.6$ [Figure 5.2(b)]. Similar behaviors are observed at $\gamma_+ = 0.8$ and 0.9. In Figure 5.3(a), the values of $R_{\max}$ at $\gamma_+ = 0.7$, 0.8, and 0.9 all remain within 100−150 nm, which is smaller than that at $\gamma_+ = 0.6$. Figure 5.3(b) shows the faster charge accumulation on the deposited CNPs at $\gamma_+ = 0.7 - 0.9$, as compared with that at $\gamma_+ = 0.6$. Thereby, the largest deposited CNP at $\gamma_+ = 0.7 - 0.9$ has a narrow attractive interaction zone of smaller s^* with CNPs of like−charge in the gas phase, as compared with that at $\gamma_+ = 0.6$. Similar to what is noted at $\gamma_+ = 0.6$, deposited CNPs do not grow; rather, gaseous CNPs coalesce. Figure 5.2(c) ($\gamma_+ = 0.7$) reveals CNPs of radii $\sim$ $100\ \text{nm}$ or greater in the gas at $t = 6000$ and $15000\tau_0$. The slow diffusion/long residence time of large CNPs in the gas phase limits the supply of small CNPs to deposited CNPs. Abnormal growth of deposited CNPs at $\gamma_+ = 0.7 - 0.9$ with a high charge sign imbalance was reduced, as was also apparent at $\gamma_+ = 0.6$.

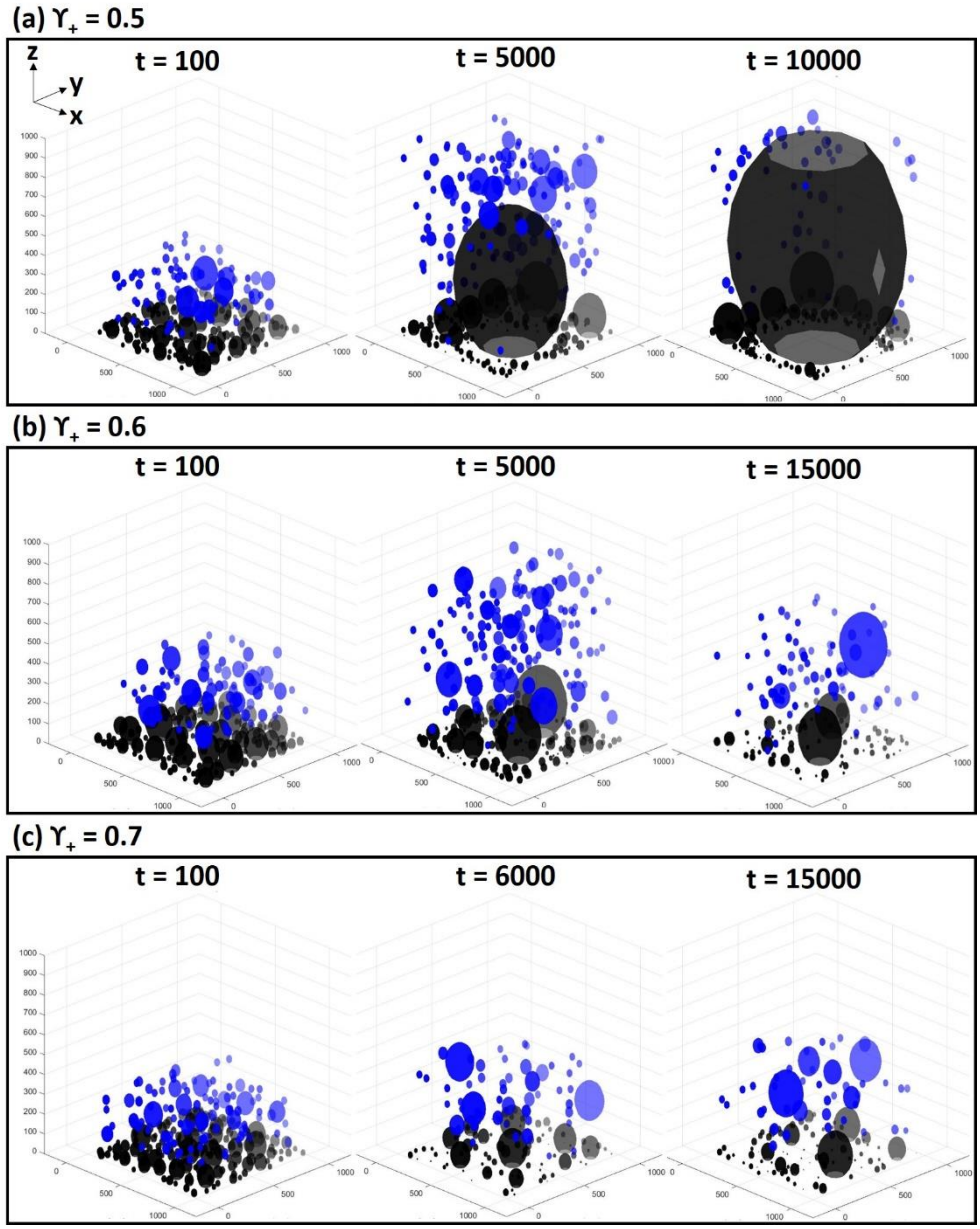

Figure 5.2 kMC simulation results: Snapshots of systems with CNPs in the gas phase and deposited CNPs at different simulation times (τ_0). Three values of the charge sign ratio γ_+ were explored: (a) 0.5, (b) 0.6, and (c) 0.7. Blue and black spheres represent the positions and sizes of CNPs in the gas phase and deposited CNPs, respectively. The initial parameters for simulation were $r_0 = 20$ nm, $q_0 = \pm e$, $\eta = 0.03$, $T = 1223$ K, $k_{\text{etch}} = 0.05$ nm/τ_0, and $v_{\text{flow}} = 5$ nm/τ_0. The dimensions of each domain were $1000 \times 1000 \times 1000$ nm^3.

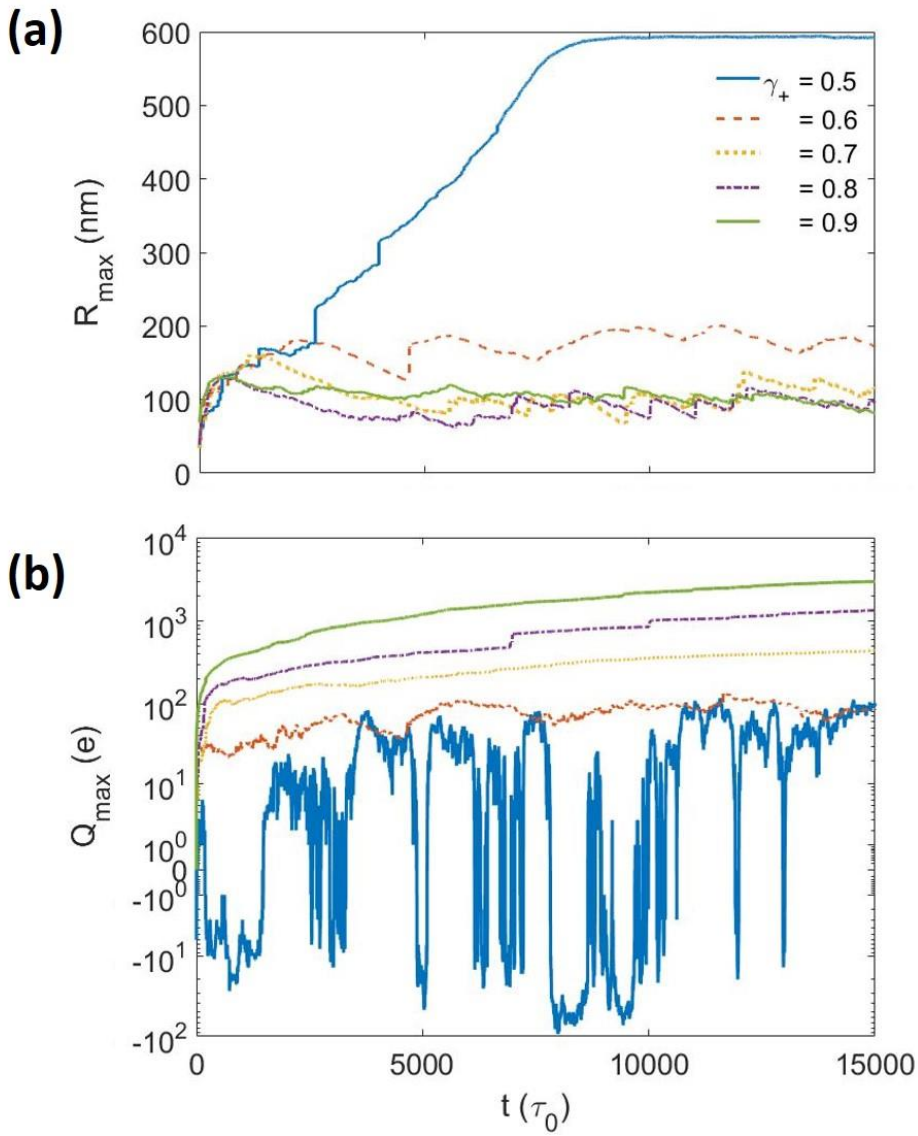

Figure 5.3 (a) The radius $R_{\max}$ and (b) the charge $Q_{\max}$ of the largest deposited particle as a function of t (τ_0), as indicated by the kMC simulation results of Figure 5.2, for $\gamma_+ = 0.5 - 0.9$.

5.3.2 Effect of volume fraction of CNPs

We next investigated the growth behaviors of deposited CNPs when the volume fraction η of CNPs in the gas phase varied. Note that η is similar to the number density of CNPs in the gas phase under experimental conditions. We used $\gamma_+ = 0.5$ to balance charges of CNPs in the gas phase and $v_{\mathrm{flow}} = 5\ \mathrm{nm}/\tau_0$ to accelerate the growth dynamics.

Figure 5.4 shows snapshots of kMC simulations at different times for three values of η (0.005, 0.02, and 0.03). To obtain the details, we plotted the radius (R_{max}) of the largest deposited CNP over time. Figure 5.5 shows the R_{max} values for representative $\eta = 0.005 - 0.05$. Although not shown in Figure 5.4, the results for $\eta = 0.01, 0.04$ and 0.05 are shown in Figure 5.5 (for comparison).

At $\eta = 0.005$ in Figure 5.4(a), some CNPs are deposited; however, they barely grow. The value of R_{max} at $\eta = 0.005$ in Figure 5.4 remains less than 70 nm during the entire simulation. This implies that the growth rate of deposited CNPs is even smaller than the etching rate afforded by the low CNP number density in the gas phase. At $\eta = 0.01$ in Figure 5.5, the value of R_{max} is always less than 120 nm during the simulation. Although R_{max} is larger than that at $\eta = 0.005$ (because there are more CNPs in the gas

phase), the CNP density at $\eta = 0.01$ does not allow the growth rate to exceed the etching rate.

At $\eta = 0.02$ in Figure 5.4(b), several CNPs of similar radii (about 150 nm) are deposited at $t = 10000\tau_0$; grow steadily; and coalesce into one large CNP before $t = 20000\tau_0$. Thereafter, the large CNP continuously grows (as shown at $t = 30000\tau_0$). The $R_{\max}$ at $\eta = 0.02$ of Figure 5.5 shows that growth of the largest deposited CNP stagnates around $R_{\max} = 175\ \text{nm}$ until $t \approx 15500\tau_0$. A drastic increase in $R_{\max}$ occurs at $t \approx 15500\tau_0$, attributable to coalescence with adjacent, large deposited CNPs. After $t \approx 15500\tau_0$, the largest deposited CNP grows even further. At $t \approx 24000\tau_0$, $R_{\max}$ attains about 600 nm, thus the maximum radius of the simulation domain.

At the $\eta = 0.03$ of Figure 5.4(c), the growth rate of deposited CNPs is faster than that at the $\eta = 0.02$ of Figure 5.4(b). The value of $R_{\max}$ of Figure 5.5 shows that the largest deposited CNP at $\eta = 0.03$ grows faster than that at $\eta = 0.02$. $R_{\max}$ attains about 600 nm at $t \approx 9000\tau_0$. At the $\eta = 0.04,\ 0.05$ of Figure 5.5, the times taken to attain $R_{\max} \approx 600\ \text{nm}$ are $t \approx 4700\tau_0$ and $2800\tau_0$, respectively, thus shorter than that at $\eta = 0.03$. These results are explained by more frequent coalescence between deposited CNPs and CNPs in the gas phase as the particle volume fraction η increases. Thus, abnormal

growth of deposited CNPs is enhanced when the volume fraction η of CNPs in the gas phase increases.

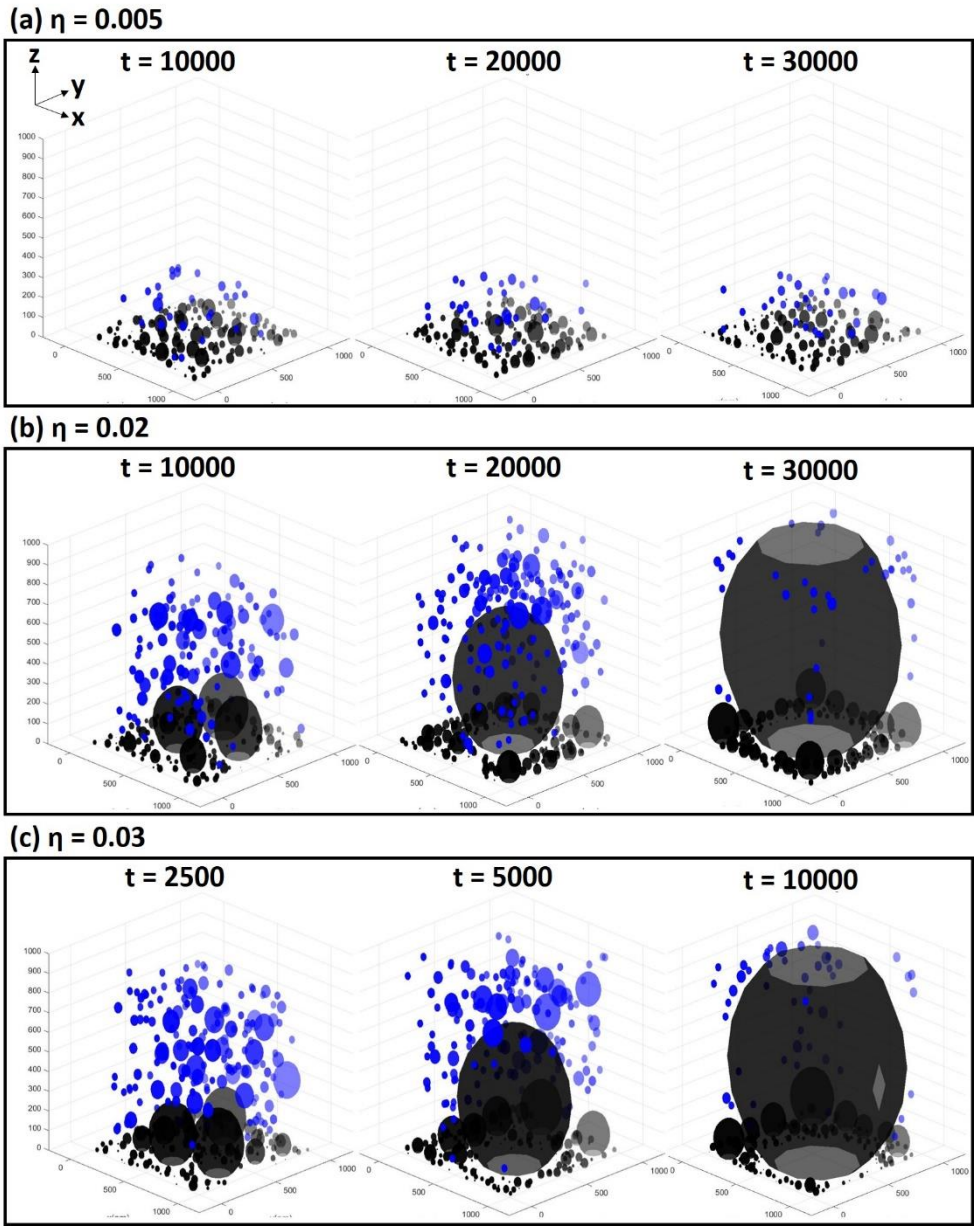

Figure 5.4 kMC simulation results: Snapshots of systems with CNPs in the gas phase and deposited CNPs at different simulation times (τ_0). Three values of the volume fraction η were explored: (a) 0.005, (b) 0.02, and (c) 0.03. The blue and black spheres represent the positions and sizes of CNPs in the gas phase and deposited CNPs, respectively. The initial parameters for simulation were $r_0 = 20\ \text{nm}$, $q_0 = \pm e$, $\gamma_+ = 0.5$, $T = 1223\ \text{K}$, $k_{\text{etch}} = 0.05\ \text{nm}/\tau_0$, and $v_{\text{flow}} = 5\ \text{nm}/\tau_0$. The dimensions of each domain were $1000 \times 1000 \times 1000\ \text{nm}^3$.

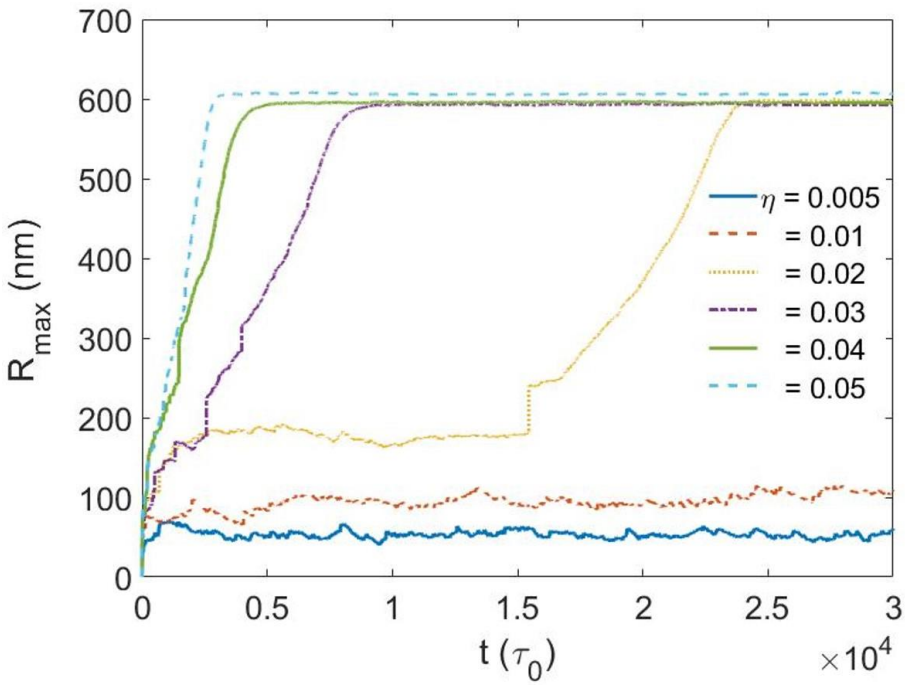

Figure 5.5 The radius $R_{\max}$ of the largest deposited particle as a function of t (τ_0), obtained from the kMC simulation results in Figure 5.4, for $\eta = 0.005 - 0.05$.

5.3.3 Effect of gas flow velocity

Above, we show that the charge sign balance (γ_+) and volume fraction (η) of the CNPs in the gas phase were important in terms of abnormal growth of deposited CNPs. However, γ_+ and η are difficult to experimentally control. Thus, we now consider the drift velocity v_{flow} of CNPs in the gas phase; this can be controlled. We varied v_{flow} at $\gamma_+ = 0.6$ and $\eta = 0.03$ and compared the results to those of Figure 5.2(b) at $v_{\mathrm{flow}} = 5\ \mathrm{nm}/\tau_0$.

Figure 5.6 shows snapshots of kMC simulations at different times for three values of v_{flow} (0, 10, and $15\ \mathrm{nm}/\tau_0$). To explore the details, we plotted the radius R_{max} of the largest deposited CNP over time. Figure 5.7 shows the R_{max} results for each representative $v_{\mathrm{flow}} = 0 - 20\ \mathrm{nm}/\tau_0$. The results at $v_{\mathrm{flow}} = 5\ \mathrm{nm}/\tau_0$ are shown in Figure 5.2(b). Although not shown in Figure 5.6, the data at $v_{\mathrm{flow}} = 20\ \mathrm{nm}/\tau_0$ are shown in Figure 5.7 (for comparison).

At the $v_{\mathrm{flow}} = 0\ \mathrm{nm}/\tau_0$ of Figure 5.6(a), there is no gas flow; CNPs in the gas phase diffuse only via electrostatic interactions. At the R_{max} at $v_{\mathrm{flow}} = 0\ \mathrm{nm}/\tau_0$ of Figure 5.7, the radius of the largest deposited CNP is below 190 nm during the entire simulation, thus similar to what is apparent in Figure 5.2(b) at $v_{\mathrm{flow}} = 5\ \mathrm{nm}/\tau_0$, where abnormal growth of deposited CNPs was inhibited.

At the $v_{\mathrm{flow}} = 10\ \mathrm{nm}/\tau_0$ of Figure 5.6(b), the gas flow velocity is twice that of Figure 5.2(b). Two deposited CNPs with $R = 250\ \mathrm{nm}$ (approximately) are observed at $t = 5000\tau_0$; they steadily grow and coalesce into a single CNP before $t = 7500\tau_0$;. The value of R_{max} at $v_{\mathrm{flow}} = 10\ \mathrm{nm}/\tau_0$ in Figure 5.7 indicates that the coalescence time is $t = 7240\tau_0$, at which time the value of R_{max} drastically increases. After coalescence, the largest deposited CNP grows continuously. At $t \approx 9000\tau_0$, R_{max} attains about $600\ \mathrm{nm}$, thus the maximum radius of the simulation domain.

At the $v_{\mathrm{flow}} = 15\ \mathrm{nm}/\tau_0$ of Figure 5.6(c), the growth rate of deposited CNPs is faster than that at the $v_{\mathrm{flow}} = 10\ \mathrm{nm}/\tau_0$ of Figure 5.6(b). The value of R_{max} in Figure 5.7 shows that the largest deposited CNP at $v_{\mathrm{flow}} = 15\ \mathrm{nm}/\tau_0$ grows faster than that deposited at $v_{\mathrm{flow}} = 10\ \mathrm{nm}/\tau_0$. R_{max} attains about $600\ \mathrm{nm}$ at $t \approx 5000\tau_0$. At the $v_{\mathrm{flow}} = 20\ \mathrm{nm}/\tau_0$ of Figure 5.7, the time taken to attain $R_{\mathrm{max}} \approx 600\ \mathrm{nm}$ is $2500\tau_0$, thus shorter than that at $v_{\mathrm{flow}} = 15\ \mathrm{nm}/\tau_0$.

The values of R_{max} at $v_{\mathrm{flow}} = 0 - 20\ \mathrm{nm}/\tau_0$ in Figure 5.7 clearly show that abnormal growth of deposited CNPs is accelerated by increasing the gas flow velocity v_{flow}. To explore the details, we investigated the CNP distributions in the gas phase. The snapshot taken at $t = 5000\tau_0$ of Figure 5.6(b) of $v_{\mathrm{flow}} = 10\ \mathrm{nm}/\tau_0$ shows a drastic decrease in the number of large CNPs (radii over 100 nm)

in the gas phase compared to that of snapshot taken at the $t = 5000\tau_0$ of Figure 5.2(b) of $v_{\mathrm{flow}} = 5\ \mathrm{nm}/\tau_0$. The simulation showed that increased gas flow reduced the residence times of CNPs in gas by pushing them out of the simulation domain. Thus, a higher v_{flow} inhibits the formation of large CNPs in the gas phase, in turn reducing abnormal growth of deposited CNPs. When large-CNP formation in the gas phase is suppressed, small CNPs newly generated in the gas increase, and more coalesce with larger deposited CNPs. These effects of v_{flow} explain the abnormal growth of deposited CNPs well.

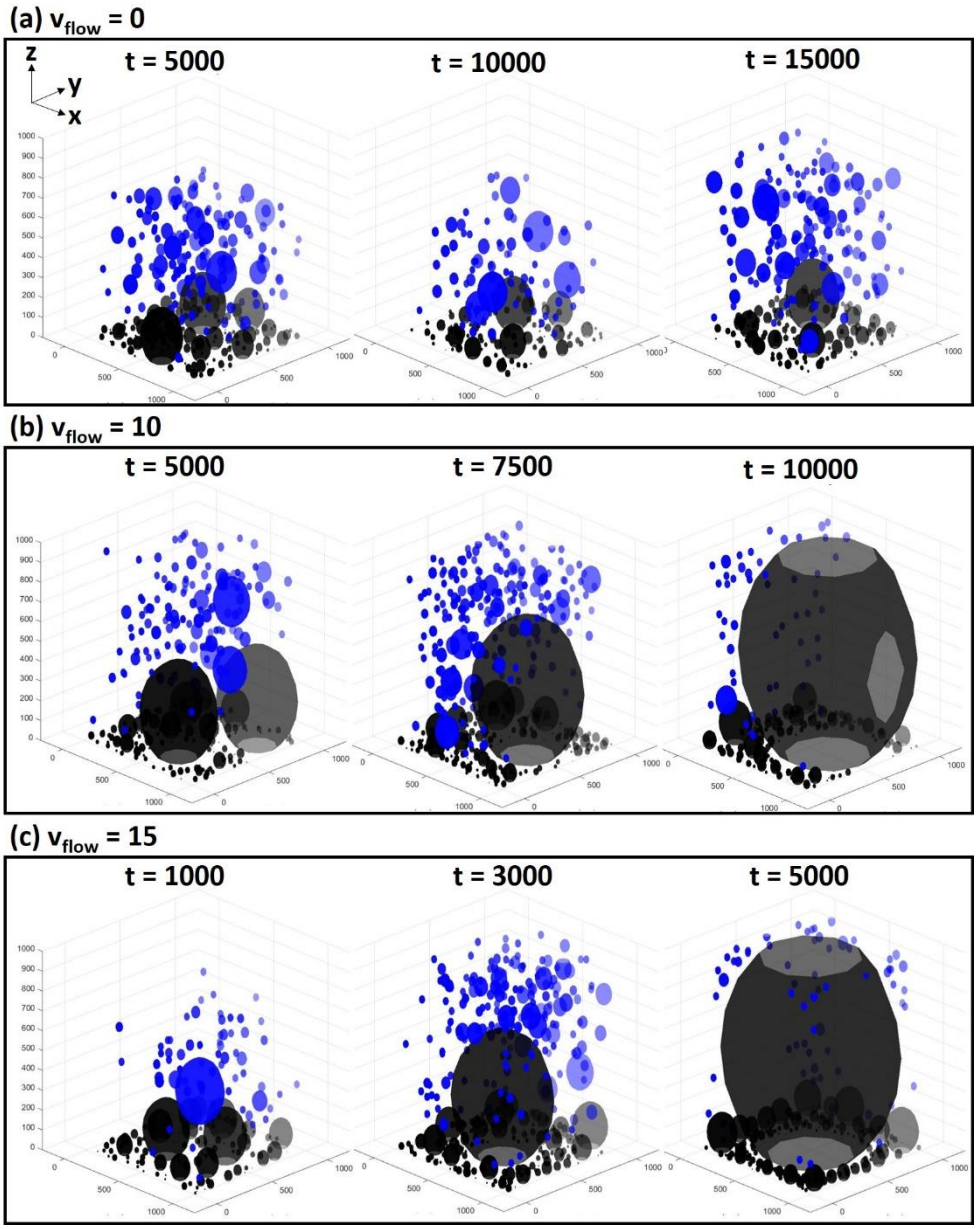

Figure 5.6 kMC simulation results: Snapshots of systems with CNPs in the gas phase and deposited CNPs at different simulation times (τ_0.). Three gas flow velocities v_{flow} were explored: (a) 0 (no flow), (b) 10, and (c) 15 nm/τ_0. The blue and black spheres represent the positions and sizes of CNPs in the gas phase and deposited CNPs, respectively. The initial parameters for simulation were $r_0 = 20\ \text{nm}$, $q_0 = \pm e$, $\gamma_+ = 0.6, \eta = 0.03$, $T = 1223\ \text{K}$, and $k_{\text{etch}} = 0.05\ \text{nm}/\tau_0$. The dimensions of each domain were $1000 \times 1000 \times 1000\ \text{nm}^3$.

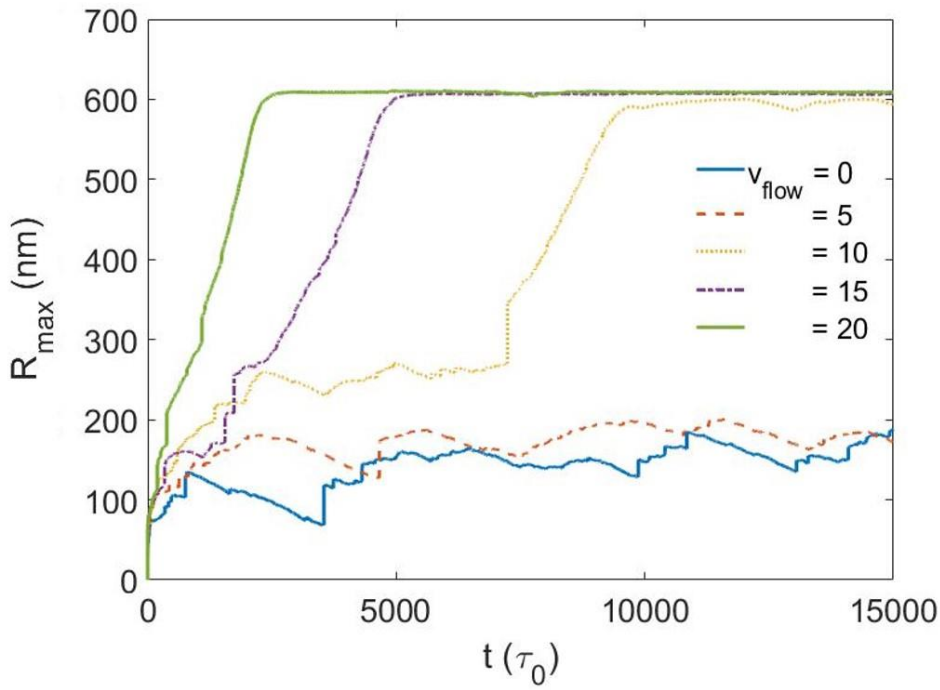

Figure 5.7 The radius $R_{\max}$ of the largest deposited particle as a function of t (τ_0), obtained from the kMC simulation results in Figure 5.6, for $v_{\text{flow}} = 0 - 20\ \text{nm}/\tau_0$.

5.3.4 Characteristic time scale and characteristic feature for CNP growth

We briefly turn to the characteristic time scale, τ_0, of the kMC simulations. Figure 5.6(b) that employs $\gamma_+ = 0.6$, $\eta = 0.03$, and $v_{\text{flow}} = 10\ \text{nm}/\tau_0$ yielded simulation results similar to those of experiments [Figure 5.1(c)] at $t \approx 10000\tau_0$. As the experimental time was $\approx 1000\ \text{s}$ in Figure 5.1(c), the time scale of τ_0 is roughly $0.1\ \text{s}$. Assuming $\tau_0 = 0.1\ \text{s}$, the diffusion coefficient D_0 of unit CNP with radius $r_0 = 20\ \text{nm}$ in the gas phase is calculated as $D_0 = 1.6 \times 10^4\ \text{nm}^2/\text{s}$ from $\tau_0 = 4r_0^2/D_0$. Then, diffusion coefficient of CNP with a radius of $r = 3\ \text{nm}$ is calculated as $D(r = 3\text{nm}) = 1.07 \times 10^5\ \text{nm}^2/\text{s}$ from $D \sim r^{-1}$, which is 5 orders of magnitude larger than its value $D_{\text{exp}} = 3.6\ \text{nm}^2/\text{s}$ obtained from Chapter 4. (see Table 4.1) In other words, it is much closer to the theoretical value $D_{\text{th}} \approx 10^8\ \text{nm}^2/\text{s}$. Considering that the difference between the experimental and theoretical values comes from the surface effect, the simulation models used in Chapter 5 seem to be much less affected by the substrate surface: CNPs in the gas phase relatively far from the substrate surface are mainly dealt with.

The lower panel in Figure 5.1(c) shows vacancies on a few SiN_x units. We suggest that these reflect effects exerted by

surrounding units with abnormally large deposited CNPs. A detailed evaluation is beyond the scope of the present work; we have focused on the abnormal growth of large deposited CNPs on single SiN_x units. Further studies will be revealing.

We also briefly mention the characteristic feature for CNP growth under specific conditions of $\eta = 0.02$ in Figures 5.4(b) and 5.5 and of $v_{\mathrm{flow}} = 10\ \mathrm{nm}/\tau_0$ in Figures 5.6(b) and 5.7. The simulation results under those specific conditions for the abnormal growth of deposited CNPs showed the steady growth of large deposited CNPs with the similar size as seen at $t = 10000$ in Figure 5.4(b) and $t = 5000$ in Figure 5.6(b). Thereafter, the large CNPs coalesced into one large CNP, which continuously grew. It was found that the largest deposited CNP grew even further when R_{max} exceeded a certain critical size. The critical radii were in the ranges of 200−250 nm at $\eta = 0.02$ in Figure 5.5 and 250−350 nm at $v_{\mathrm{flow}} = 10\ \mathrm{nm}/\tau_0$ in Figure 5.7. For detailed information about the critical radius for the abnormal growth of deposited CNPs, more studies will be needed.

5.4. Conclusion

To understand the physics underlying of the abnormal growth of deposited Si particles during CVD, we performed kMC simulations of three-dimensional multi-CNP systems featuring electrostatic interactions. We investigated the growth behaviors of CNPs on substrates. CNPs were generated in the gas and etching proceeded at a constant rate. We discovered three important parameters that affected the growth of deposited CNPs. The first, γ_+, was the ratio of positively CNPs to all CNPs in the gas. When the charge was balanced ($\gamma_+ = 0.5$), abnormal growth of the deposited CNPs was favored; this was not the case when the charge was imbalanced. The second parameter was η, thus the volume fraction of CNPs in the gas phase. When $\eta = 0.02$ or higher, abnormal growth of deposited CNPs was favored given the frequent coalescence between deposited CNPs and CNPs in the gas. The last parameter was v_{flow}, thus the gas flow velocity along the lateral surface. Abnormal growth of deposited CNPs was favored at larger v_{flow}: Faster flow suppressed the formation of large CNPs in the gas, in turn inhibiting abnormal growth of deposited CNPs. The increased supply of small CNPs newly generated in the gas enhanced their coalescence with larger deposited CNPs. In

summary, our kMC simulations based on non-classical crystallization theory (thus the use of CNPs as the building blocks for particle growth) explain the abnormal growth of deposited particles well.

Chapter 6. Effects of substrate electrical conductivity on growth of deposited particles

6.1. Introduction

It has been reported that different deposition behaviors are observed depending on the electrical conductivity of the substrate. As mentioned in Chapter. 1, Figure 1.3 shows that considerably porous and graphitic soot particles grow on an iron substrate while crystalline diamond films grow on the silicon substrate under the equal deposition conditions. [22,31] Figure 1.7 shows the results of deposited Si films on the floating and grounded Si substrates. [23] A dense film with a thickness of ~220nm was deposited on the floating substrate in Figures 1.7(a) and (b) while a porous film with a thickness of ~190nm was deposited on the grounded substrate in Figures 1.7(c) and (d). Similarly, Cheong et al. [82] also compared the deposition behavior of Si between the Si and Fe substrates. They reported that the results of deposited Si films microstructures on Fe and Si substrates. A porous film with a thickness of ~5mm was observed on the Fe substrate while dense film with only ~3 μm was deposited on the Si substrate.

There is a phenomenological tendency that deposition occurs on the conducting area but does not occur on the non-conducting area

in the CVD process. Applying this tendency, selective CVD process is extensively utilized for the formation of films in microelectronics. [83-85] A target metal is controlled to deposit selectively on a specific pattern on the growth surface, typically a metal or a semiconductor, in the presence of a non-growth surface, a dielectric or insulating material. These selective CVD processes have been mainly called selective growth selective epitaxial growth (SEG) [86-88] or selective nucleation-based epitaxy (SENTAXY) [53-55, 89].

Hwang et al. [80] compared the deposition behavior during Si CVD between five different substrates; SiO_2, Si_3N_4 (insulators), Si (semi-conductor), Mo and Pt (conductor). Figure 6.1 shows the deposition behavior of Si on the (a) Mo, conducting substrate, (b) SiO_2, insulator. On the conducting substrates, Si deposited steadily as time elapses as shown in Figure 6.1(a). On the insulator substrates, however, the deposition behavior drastically changed as shown in Figure 6.1(b). After 3 min, Si were rarely seen on the substrate but after 6 min, an appreciable number density (~ 10^9 cm^{-2}) of Si particles was observed. After 12min, most of the Si particles had disappeared and they were hardly seen after 24 min.

As mentioned above, differences in deposition behavior are clearly observed depending on the electrical conductivity of

substrate. It is qualitatively speculated that the electrostatic interaction of CNPs in the gas phase and the substrate is due to this difference, the exact physical mechanism still remains unknown. Thus, it is necessary to investigate the effect of electrostatic interaction on deposition behavior through accurate calculation of electrostatic potential energy between CNPs in the gas phase and substrate.

In this chapter, the electrostatic potential energy between a CNP and three types of substrate was investigated: grounded conductor, floating conductor, and insulator. Then, we performed kinetic Monte Carlo (kMC) simulations similar to that used in Chapter. 5, but the underlying electrostatic potential energy includes between CNPs and substrate as well as among CNPs. We explored the effects of electrical conductivity of substrates to the growth rates of deposited particles and compared the simulation results with the experimental results.

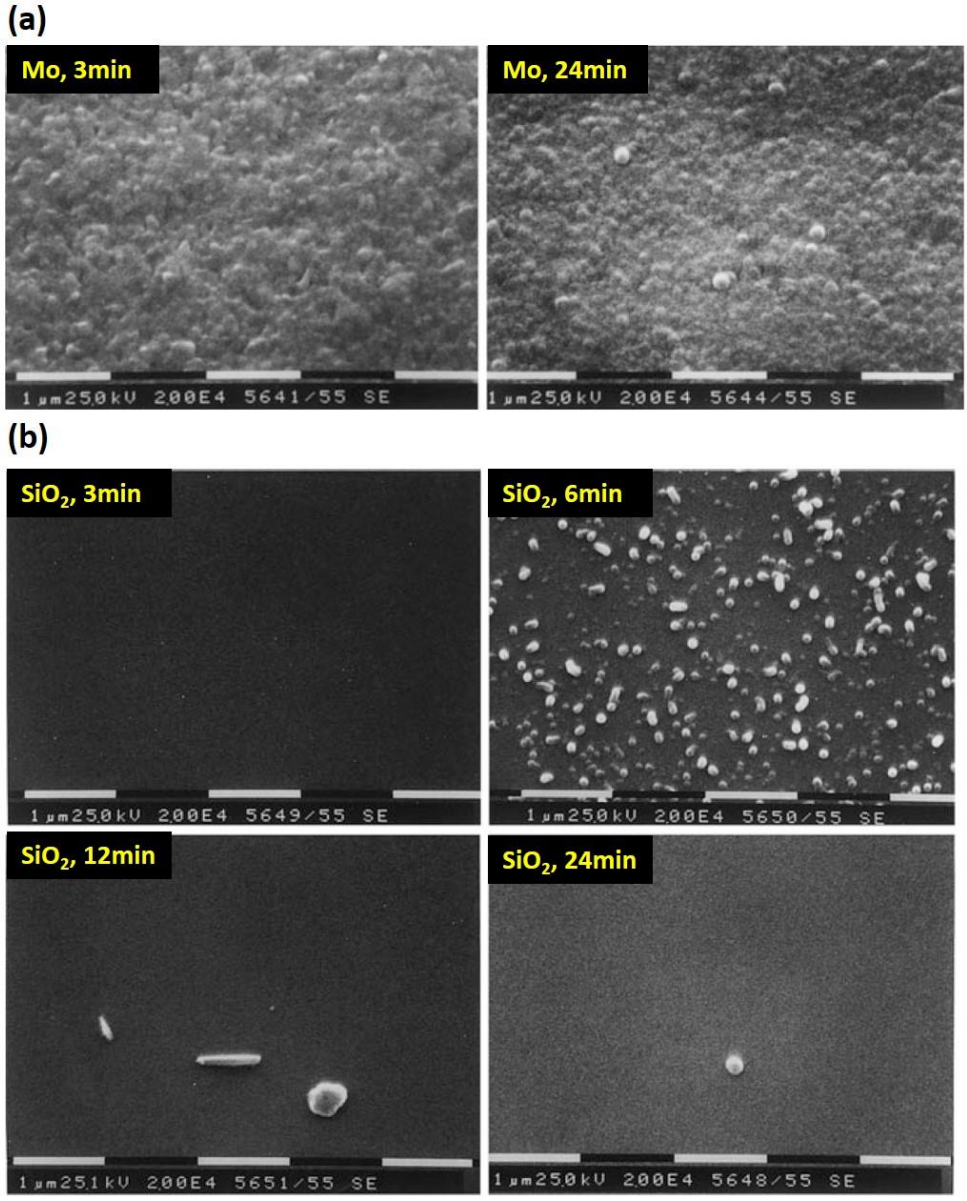

Figure 6.1 Time evolution of deposition behavior of Si on the (a) Mo and (b) SiO_2 substrate with the SiH_4 : HCl : H_2 gas ratio of 1 : 2 : 97 under a reactor pressure of 100 Torr at a substrate temperature of 950 ℃. [80]

6.2. Computational Details

We performed kMC simulations to compare the growth dynamics of many-CNP systems depending on the electrical properties of the substrates. The simulation processes are same with that of Chapter 5.2. However, during the kMC simulations in this chapter, electrostatic potential energy term between CNPs and the substrate is added when the substrate is 1) a grounded conductor and 2) a floating conductor. Note that when the substrate is 3) an insulator, the processes are perfectly same with that of Chapter 5.2.

When substrate is a grounded conductor, the CNPs with charge q in the gas phase lose their charge as soon as they are deposited on the substrate (i.e., the value of q becomes zero). Unlike when the substrate is an insulator, electrostatic potential energy is formed between CNPs in the gas phase and the conductor substrate due to the induced charge. The CNP in the gas phase was modeled as sphere with radius of r and charge of q [see Figure 6.2(a)]. Assuming that the CNPs serve as solid conductors in a continuum, the electrostatic potential energy $W_{induced}$ is given by [90]

$$W_{induced} = \frac{q^2}{2C} \tag{40}$$

where C is the capacitance coefficient between the CNP and the conductive substrate expressed by

$$C = 4\pi\epsilon_0 r \sinh\alpha \sum_{n=1}^{\infty} [\sinh n\alpha]^{-1} \quad (41)$$

Here, a dimensionless parameter α is

$$\alpha = \frac{s+r}{r} \quad (42)$$

where s is the separation distance between the CNP and the substrate as shown in Figure 6.2(a). The values of C was approximated to an accuracy of 10^{-7} via finite summation of the infinite series shown in Equations (41).

When substrate is a floating conductor, the charge is distributed uniformly across the deposited CNPs and the substrate surface [see Figure 6.2(b)]. Thus, the surface charge density σ becomes the same, which is defined as:

$$\sigma = \frac{Q}{A} \quad (43)$$

where Q is the total accumulated by the deposited CNPs and A is the surface area of the substrate and the deposited CNPs. The deposited CNPs with radius of r_i have charge of $q_i = \sigma(4\pi r_i^2)$.

The electric field generated by an infinite flat conductor with a uniform surface charge density σ is $E = \frac{\sigma}{2\epsilon_0}$ in the direction perpendicular to the plane. Note that the substrate is large enough

that it can be assumed to be infinite relative to the size of the CNPs. Then, the small force dF acting on the small area dA with small charge dq of the CNP in Figure 6.2(b) is

$$dF = Edq = E(2\pi r^2 \sigma_p \sin\phi d\phi) \tag{44}$$

where σ_p and ϕ is the surface charge density of the CNP and angle to the direction of the electric field, respectively, as displayed in Figure 6.2(b). The value of σ_p is given by [56]

$$\sigma_p = \frac{q}{4\pi r^2} + 3\epsilon_0 E\cos\phi \tag{45}$$

By integrating equation (44) for ϕ from 0 to π, then the force F acting on the CNP by electric field E from the substrate is expressed by $F = qE = \frac{q\sigma}{2\epsilon_0}$. Note that the value of force is independent on the size of the CNP. Therefore, the electrostatic potential energy $W_{Coulomb}$ can be obtained by integrating the force in the negative direction as follows:

$$\begin{aligned} \Delta W_{Coulomb} &= \int_{s_0}^{s} -Fds = -\frac{q\sigma}{2\epsilon_0}\Delta s \\ W_{Coulomb}(s) &= W_{Coulomb}(s_0) - \frac{q\sigma}{2\epsilon_0}(s - s_0) = -\frac{q\sigma}{2\epsilon_0}(s - s_0) \end{aligned} \tag{46}$$

where s_0 is arbitrary standard separation distance where $W_{Coulomb}(s_0) = 0$ to decide the value of electrostatic potential energy. Considering the substrate is conductive, the potential energy term by induced charge should be also considered.

Therefore, combining equations (40) and (46), the total potential energy is given by

$$W(s) = W_{Coulomb}(s) + W_{induced}(s) = -\frac{q\sigma}{2\epsilon_0}(s - s_0) + \frac{q^2}{2C} \qquad (47)$$

where the capacitance coefficient is given by equations (41) and (42).

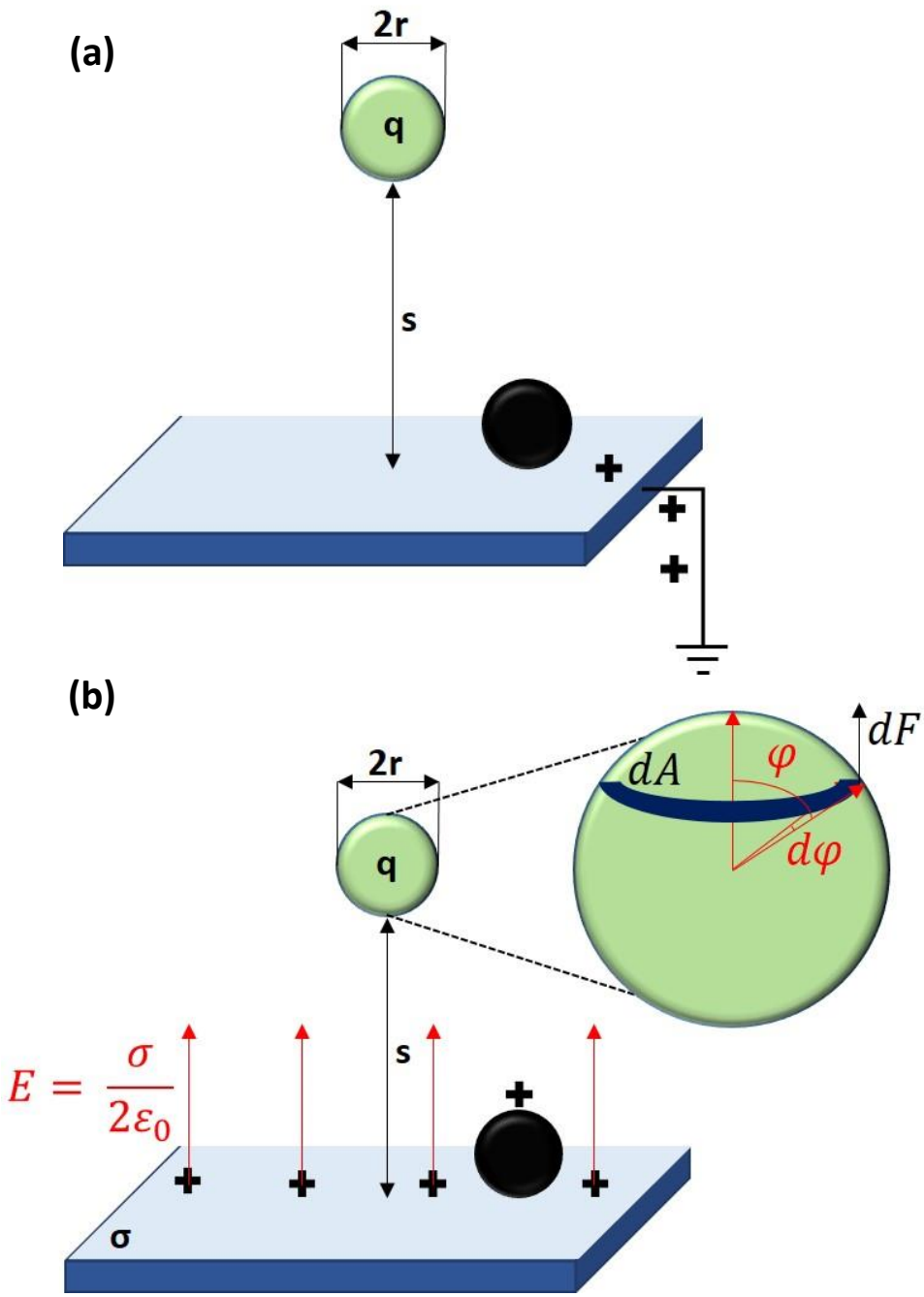

Figure 6.2 A schematic of system with a spherical CNP and substrate. The substrate is (a) grounded conductor (b) floating conductor. The green circle denotes a CNP in the gas phase with a radius r and a charge q. The blue rectangular parallelepiped and black circle denote the substrate and deposited CNP on the substrate, respectively.

6.3. Results and Discussions

6.3.1 Electrostatic potential energy between a CNP and conductive substrate

First, we calculated the electrostatic potential energy between a CNP and grounded conductive substrate. Figure 6.3 shows the W value divided by q^2 as a function of separation distance s between a CNP and a grounded substrate. With increasing s, W increases and the rate of increase decreases. As the radius of CNP r decreases, the increase rate of W increases. Note that this tendency is independent of the sign of the CNPs since the square of charge q^2 is included in the term. These results indicate that the both positively and negatively CNPs are always attractive to the grounded conductive substrate from $F_s = -\frac{dW}{ds}$. The closer to the CNP is to the grounded conductive substrate, the smaller the CNP, and the greater the charge of the CNP, the stronger the attractive interaction.

When the substrate is a floating conductor, the charges are accumulated on the substrate by the deposited CNPs during the CVD processes since there is no path for the charge to escape. Thus, Coulomb electrostatic potential energy between the CNPs and

the charges accumulated on the substrate is added compared to the grounded substrate. Figure 6.4 shows the value of W as a function of s for the system with the CNP with radius $r = 5\,\mathrm{nm}$ and charge $q = +e$ and floating conductive substrate with surface charge density $\sigma = -2 * 10^{-4} - +2 * 10^{-4} e/\mathrm{nm}^2$. The standard separation distance s_0 is defined as 100 nm so $W(s_0 = 100\,\mathrm{nm})$ becomes 0. Note that the value of W is same with that of $r = 5\,\mathrm{nm}$ in Figure 6.3 when $\sigma = 0$, i.e. the substrate is grounded conductor. When $\sigma \leq 0$, the value of W always increases and the increase rate decreases with increasing s and the absolute value of surface charge density, $|\sigma|$. These indicate the positively CNPs always have attractive interaction with the substrate and the interaction becomes stronger as the CNPs get closer to the substrate and more negative charges are accumulated on the floating substrate.

When $\sigma > 0$, the values of W rapidly increases and then slowly decreases with increasing s, which shows similar tendency with the results in Figures. 3.2(b) and 3.3. The gradient of W depends on the transition separation distance s^* defined in Chapter 3.3.1; the interaction between the CNP and the substrate becomes attractive when $s < s^*$ and repulsive when $s > s^*$. At $\sigma = 1 * 10^{-4}, 2 * 10^{-4} e/\mathrm{nm}^2$, the values of s^* are 15, 9.3 nm, respectively, as shown in Figure 6.4. The values of W^*, which is the value of W when $s =$

s^*, are 0.0589, 0.139 eV at $\sigma = 1 * 10^{-4}, 2 * 10^{-4} e/\mathrm{nm}^2$, respectively. With increasing value of σ, the value of s^* decreases and W^* increases, whjch indicates the CNP repels stronger as the value of σ becomes larger. In other words, the more charges of the same sign with the CNP are accumulated on the substrate, the stronger the repulsive interaction.

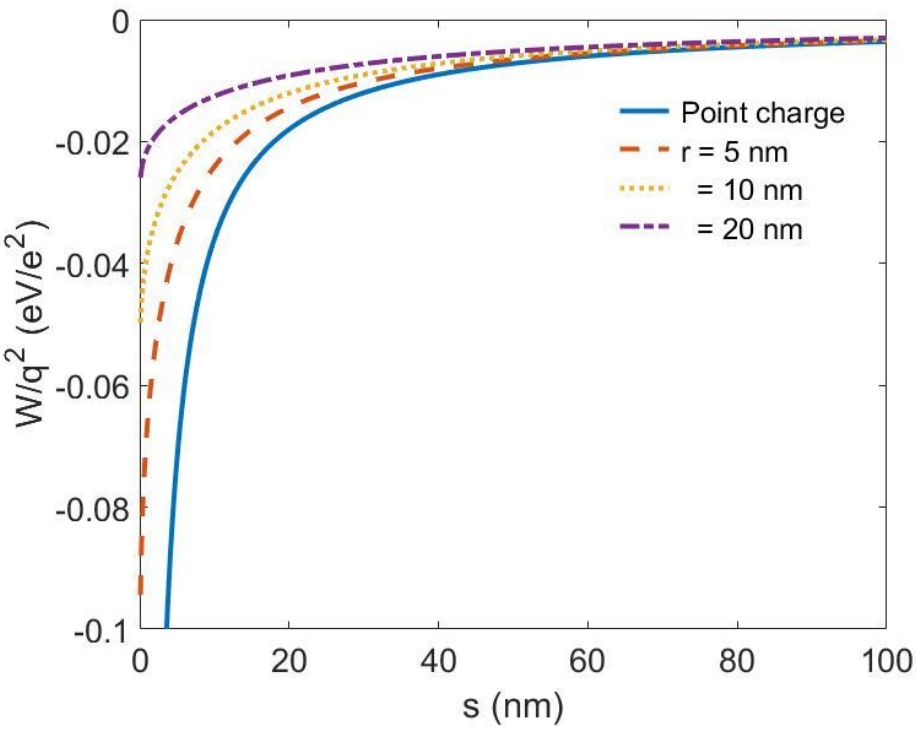

Figure 6.3 W, excluding self-energy of CNP, divided by q^2 as a function of s for the CNP-grounded conductive substrate system. The radius of CNP r varies from 5 nm to 20 nm. For comparison, the value of W for point charge is also plotted.

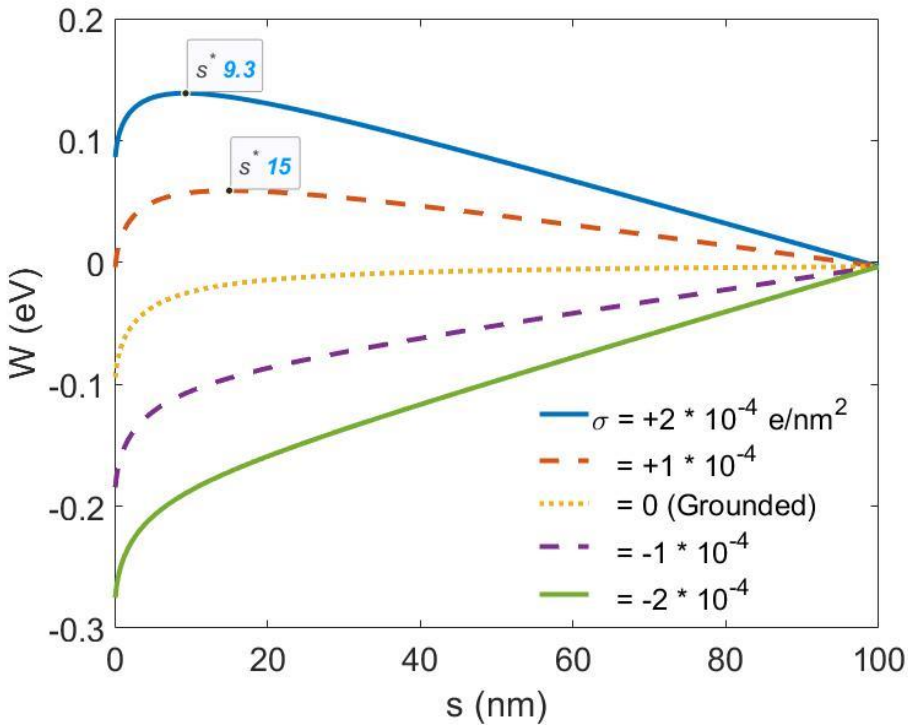

Figure 6.4 W, excluding self-energy of CNP as a function of s for the CNP-floating conductive substrate system ($r = 5\ \text{nm}, q = +e$, $s_0 = 100\ \text{nm}$). The surface charge density of the substrate σ varies from $-2 * 10^{-4} e/\text{nm}^2$ to $+2 * 10^{-4} e/\text{nm}^2$. For the positive σ, the values of transition separation distance s^* are expressed for each σ.

6.3.2 Substrate conductivity effects on growth behaviors and rates of deposited CNPs: non−etching conditions

To investigate the experimental results of the growth behavior and rate of deposited CNPs depending on the conductivity of the substrate, we simulated the system composed of many−CNPs in the gaseous phase by changing the electrical property of the substrate. The simulation parameters $\gamma_+, \eta, k_{\text{etch}}$, and v_{flow} are defined the same as in Chapter. 5 and the value of k_{etch} was set to 0 nm/τ_0 to assume non−etching environment. The values of η and v_{flow} were set to 0.001 and 5 nm/τ_0, respectively.

We first performed kMC simulations of CNPs for three types of substrates by varying the value of γ_+. Figure 6.5, 6.6, and 6.7 show the snapshots of the simulation results for different times when the value of γ_+ is 0.5, 0.7 and 0.9, respectively, for three types of substrates: (a) grounded conductor, (b) floating conductor, and (c) insulator. The red and black spheres represent the CNPs in the gas phase and deposited CNPs on the substrate in the xy−plane, respectively. To explore the details, we plotted the film thickness d obtained by dividing the total volume of the deposited CNPs by the area of the substrate domain $L^2 = (10^3\ \text{nm})^2 = 10^6\ \text{nm}^2$ and the surface charge density σ for the floating conductor substrates.

Figure 6.8(a)−(c) shows the value of d for $\gamma_+ = 0.5, 0.7,$ and 0.9, respectively. It is plotted for three types of the substrates. Figure 6.8(d) shows the σ for $\gamma_+ = 0.5 - 0.9$ for the floating conductive substrate.

At the $\gamma_+ = 0.5$ of Figure 6.5, the numbers of the positively and negatively CNPs in the gas phase are balanced. The deposited CNPs on the grounded conductor grow more slowly than the floating conductor and insulator comparing the results of Figure 6.5(a)−(c). Figure 6.8(a) shows the detailed growth rates of the deposited CNPs. The thickness increase rates at $\gamma_+ = 0.5$ in Figure 6.8(a) indicate a markedly slow growth on the grounded conductive substrate.

In the case that the charge signs of the CNPs in the gas phase are balanced, $\gamma_+ = 0.5$, the coalescence between CNPs often occurs, resulting in large−sized CNPs with small charges (q). Then, when the substrate is grounded conductor [Figure 6.5(a)], the attractive interaction between CNPs in the gas phase and the substrate is weakened as can be seen in Figure 6.3. In addition, since the deposited CNPs lose charge by the grounded substrate, CNPs in the gas phase interact and coalesce with each other rather than with the deposited CNPs.

When the substrate is floating conductor [Figure 6.5(b)], a constant surface charge density σ is distributed throughout the substrate and deposited CNPs and the change of σ value with time is plotted in Figure 6.8(d) at $\gamma_+ = 0.5$. The value of σ fluctuates around 0 before $t = 5000\tau_0$, but after that it stays near zero. This indicates that the charges do not accumulate on the substrate and deposited CNPs. Instead, both positively and negatively CNPs coalesce into the deposited CNPs more actively compared to the grounded conductive substrate by stronger electrostatic attraction. Similarly, when the substrate is insulator [Figure 6.5(c)], CNPs of both signs in the gas phase actively coalesce with the deposited CNPs due to electrostatic interactions by retaining charges even after the deposition. Since the number of positively and negatively CNPs are balanced, the charges of deposited CNPs do not accumulate on them and coalescence can occur actively by electrostatic attraction with both signs of CNPs. A similar topic was discussed in detail in Chapter 5.3.2; the substrate was also assumed to be an insulator.

At the $\gamma_+ = 0.7$ of Figure 6.6, the positively CNPs in the gas phase account for 70% of all CNPs; charge is thus imbalanced. Figure 6.6(a)–(c) and 6.8(b) show that the deposited CNPs grew fastest on the grounded conductor substrate [Figure 6.6(a)], next

on floating conductor substrate [Figure 6.6(b)], and slowest on insulator substrate [Figure 6.6(c)]. These results contrast with the charge-balanced condition $\gamma_+ = 0.5$, the physical cause of which appears to be charge accumulation. Figure 6.8(d) at $\gamma_+ = 0.7$ shows about surface charge density σ of $7 - 8 \times 10^{-4}\, e/\mathrm{nm}^2$ is formed on the substrate and the deposited CNPs when the substrate is a floating conductor. This charge accumulation causes electrostatic repulsion between CNPs in the gas phase and deposited CNPs, which inhibits the growth of the deposited CNPs.

When the substrate is an insulator, charges are locally accumulated only on the deposited CNPs. In the early stages of the deposition, the amount of deposition and charge accumulation is small, so the CNPs in the gas phase are relatively free from electrostatic repulsion. Therefore, the initial growth rate is faster than on the floating conductor substrate. [see $t < 10^4 \tau_0$ in Figure 6.8(b)]. However, as the charge accumulation continues and the amount of deposited CNPs increases, more and more strong electrostatic repulsion with CNPs in the gas phase occurs, and the deposition rate gradually decreases. It can be seen at $t > 10^4 \tau_0$ in Figure 6.8(b) by comparing to that of floating conductive substrate.

At the $\gamma_+ = 0.9$ of Figure 6.7, the positively CNPs in the gas phase account for 90% of all CNPs; charge imbalance is more

severe than that at $\gamma_+ = 0.7$. The tendency of growth rate depending on the substrates is similar with that at $\gamma_+ = 0.7$ as shown in Figure 6.7(a)−(c) and 6.8(b). Figure 6.8(d) at $\gamma_+ = 0.9$ shows σ value gradually increases with time by charge accumulation and it saturates $\sim 3 \times 10^{-3}\, e/\mathrm{nm}^2$ around $t \approx 15000\tau_0$, which indicates more charges accumulate by more severe charge sign imbalance than $\gamma_+ = 0.7$.

To compare the simulation results with the experimental results, we considered the experiment performed by Youn et al. [23] which compared the deposition behavior between floating and grounded substrates. A dense film with a thickness of ~220nm was deposited on the floating silicon substrate [see Figures 1.7(a) and (b)] while a porous film with a thickness of ~190nm was deposited on the grounded silicon substrate [see Figures 1.7(c) and (d)]. This result indicates the growth rate on the floating substrate was faster than that on the grounded substrate. Considering the film on the grounded substrate was porous, the growth rate difference was larger than the ratio of thickness (220/190).

According to the simulation results, the numbers of positively and negatively CNPs should be balanced ($\gamma_+ = 0.5$) for the growth rate on the floating conductor substrate to be faster than on the grounded conductor substrate. Thus, the sign of CNPs in the gas

phase in the experiment appears to be balanced. When the N_2 flow is 1000 sccm in Figure 1.5, the number concentrations of positively and negatively CNPs are similar, which is also consistent with the simulation results.

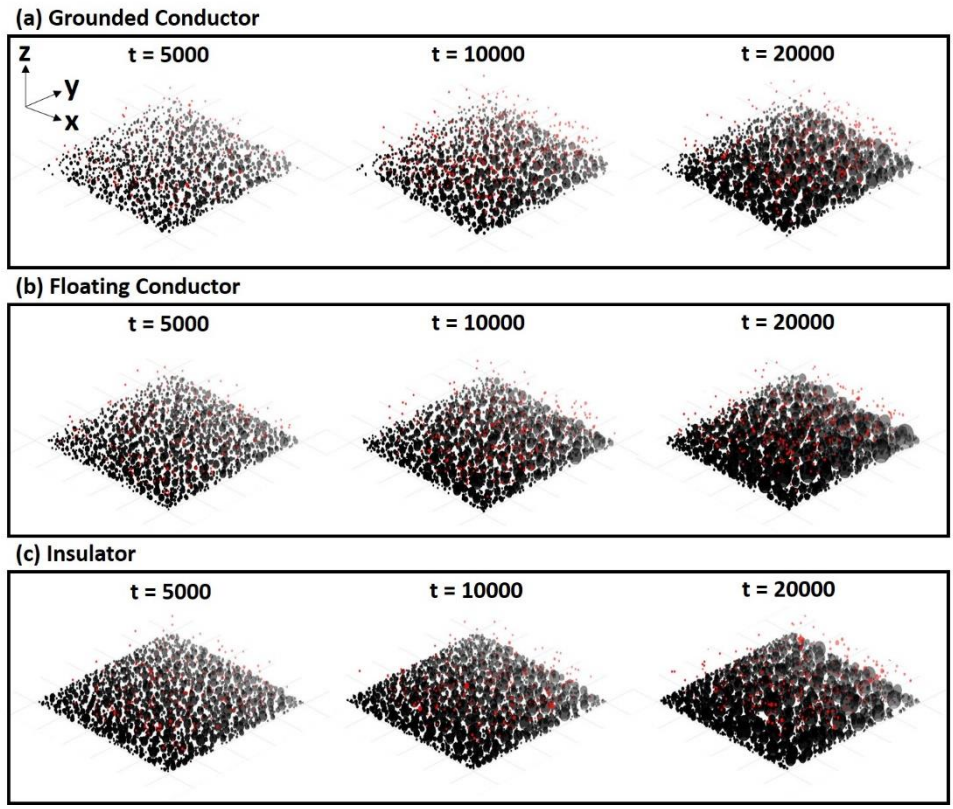

Figure 6.5 kMC simulation results: Snapshots of systems with CNPs in the gas phase and deposited CNPs at different simulation times (τ_0). Three types of the substrates were explored: (a) grounded conductor, (b) floating conductor, and (c) insulator. Red and black spheres represent the positions and sizes of CNPs in the gas phase and deposited CNPs, respectively. The initial parameters for simulation were $r_0 = 5\,\mathrm{nm}$, $q_0 = \pm e$, $\gamma_+ = 0.5$, $\eta = 0.001$, $T = 773\,\mathrm{K}$, $k_{\mathrm{etch}} = 0\,\mathrm{nm}/\tau_0$, and $v_{\mathrm{flow}} = 5\,\mathrm{nm}/\tau_0$. The dimensions of each displayed domain were $1000 \times 1000 \times 200\,\mathrm{nm}^3$.

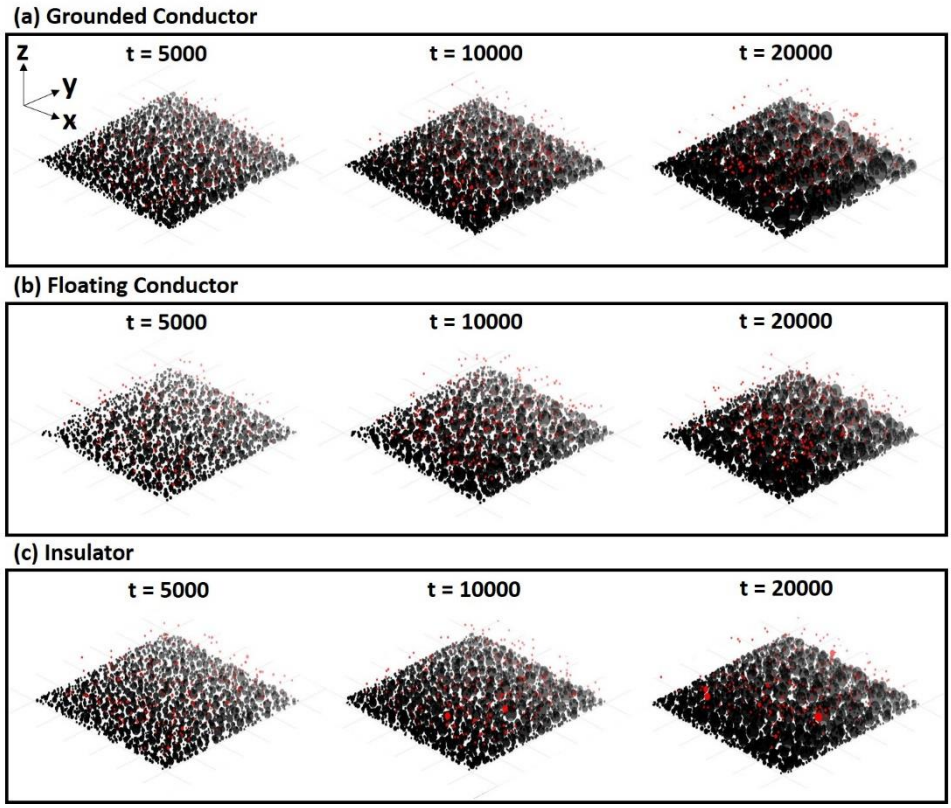

Figure 6.6 kMC simulation results: Snapshots of systems with CNPs in the gas phase and deposited CNPs at different simulation times (τ_0). Three types of the substrates were explored: (a) grounded conductor, (b) floating conductor, and (c) insulator. The simulation parameters are same with those of Figure 6.5 except for $\gamma_+ = 0.7$.

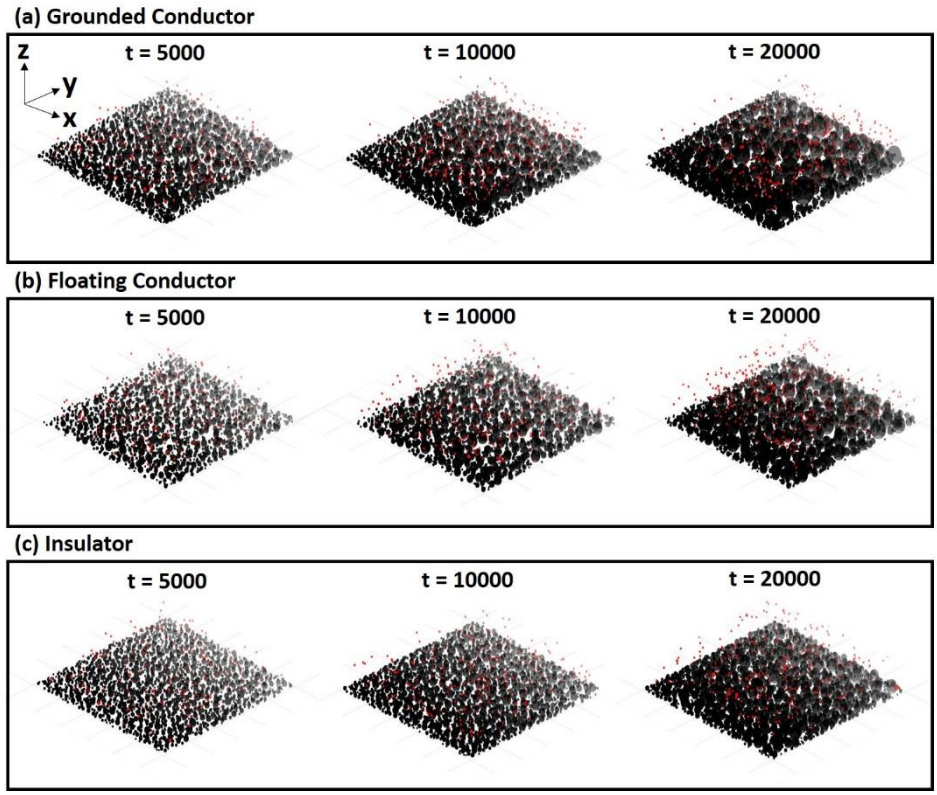

Figure 6.7 kMC simulation results: Snapshots of systems with CNPs in the gas phase and deposited CNPs at different simulation times (τ_0). Three types of the substrates were explored: (a) grounded conductor, (b) floating conductor, and (c) insulator. The simulation parameters are same with those of Figure 6.5 except for $\gamma_+ = 0.9$.

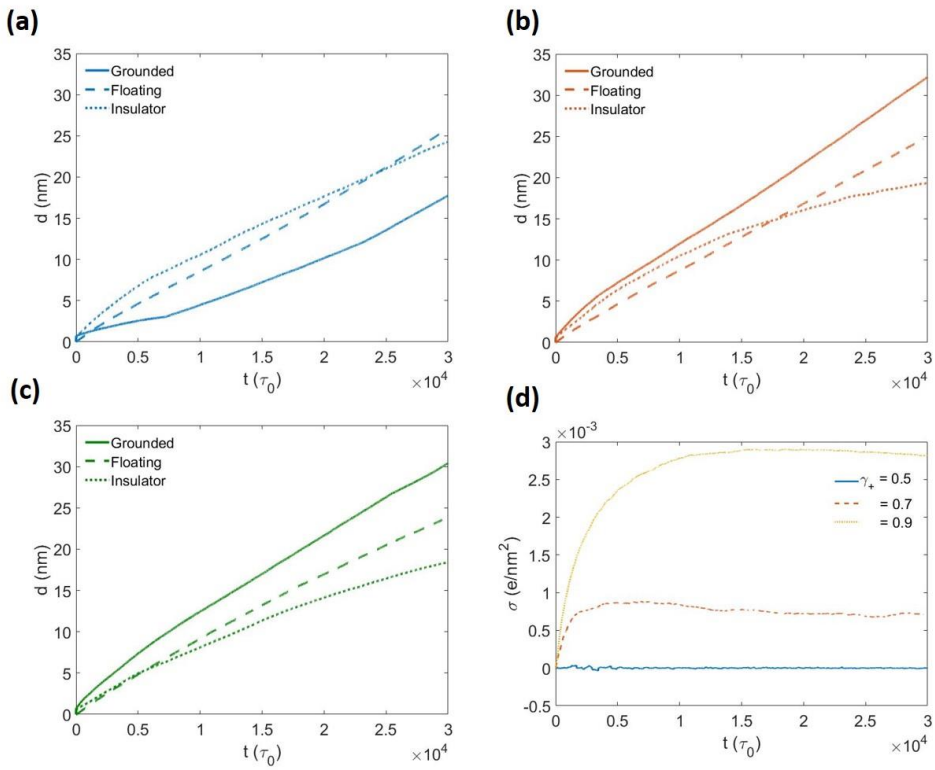

Figure 6.8 The film thickness d as a function of t (τ_0), as indicated by the kMC simulation results of (a) Figure 6.5 ($\gamma_+ = 0.5$), (b) Figure 6.6 ($\gamma_+ = 0.7$), and (c) Figure 6.7 ($\gamma_+ = 0.9$). The solid, dashed and dotted line denotes the thickness on the grounded conductor, floating conductor, and insulator substrate, respectively. (d) The surface charge density σ of the floating substrate for $\gamma_+ = 0.5 - 0.9$.

6.3.3 Substrate conductivity effects on growth behaviors and rates of deposited CNPs: etching conditions

We next investigated the growth behaviors and rated of deposited CNPs when the ambient atmosphere is the etching condition. In Chapter 5, the value of k_{etch} was assumed to be constant to consider the atomic etching CNPs. However, since small CNPs < 5 nm were mainly dealt with in this chapter in contrast to particles of ~ 20 nm or larger in Chapter 5, the Gibbs−Thompson effect was considered [91,92]. The Gibbs−Thompson effect is a phenomenon in which the etching (dissolution in solutions) rate of CNPs is accelerated by surface energy. The etching activation energy $\Delta\mu_{\mathrm{etch}}^{\mathrm{particle}}$ of the particles with radius r is given by

$$\Delta\mu_{\mathrm{etch}}^{\mathrm{particle}}(r) = \Delta\mu_{\mathrm{etch}}^{\mathrm{flat}} - \frac{2\gamma V_m}{r} \qquad (48)$$

where $\Delta\mu_{\mathrm{etch}}^{\mathrm{flat}}$, γ, and V_m are the activation energy of the flat interface where $r = \infty$, the surface energy, and molar volume, respectively. Through the activation energy barrier, the relation between etching rate constant of particle $k_{\mathrm{etch}}^{\mathrm{particle}}$ and that of flat interface $k_{\mathrm{etch}}^{\mathrm{flat}}$ is expressed by

$$k_{\mathrm{etch}}^{\mathrm{particle}}(r) = B\exp\left(-\frac{\Delta\mu_{\mathrm{etch}}^{\mathrm{particle}}(r)}{RT}\right) = k_{\mathrm{etch}}^{\mathrm{flat}}\exp\left(-\frac{2\gamma V_m}{rRT}\right) \qquad (49)$$

where B, R, and T are constant with the same dimension as the rate constant, ideal gas constant, and temperature, respectively.

Atomic etching flux J_{etch} from particle toward to the gas (solution) is given by

$$J_{\text{etch}} = -4\pi r^2 k_{\text{etch}}^{\text{particle}}(r) = -4\pi r^2 k_{\text{etch}}^{\text{flat}} \exp\left(-\frac{2\gamma V_m}{rRT}\right)$$
$$J_{\text{etch}} = \frac{dV}{dt} = (4\pi r^2)\frac{dr}{dt} \tag{50}$$

Therefore, the change in radius with time is expressed from equation (50) as follows:

$$\frac{dr}{dt} = -k_{\text{etch}}^{\text{particle}}(r) = -k_{\text{etch}}^{\text{flat}} \exp\left(-\frac{2\gamma V_m}{rRT}\right) \tag{51}$$

Using the surface energy $\gamma = 1.23\,J/m^2$ of {111} Si [93], molar volume $V_m = 1.206 \times 10^{-5}\,m^3/\text{mol}$ of Si [94], and temperature of our simulation $T = 773\,\text{K}$, Figure 6.9 shows the etching rate of the particle $dr/dt = -k_{\text{etch}}^{\text{particle}}(r)$ as a function of the radius of the particle r when $k_{\text{etch}}^{\text{flat}} = 0.01\,\text{nm}/\tau_0$. It can be seen that the smaller the particle, the faster the etching rate. Especially when the particles are smaller than 5 nm, it can be inferred that they will disappear quickly due to the rapid etching rate.

We simulated the system composed of many-CNPs in the gaseous phase for three types of the substrate. The simulation parameters $\eta, k_{\text{etch}}^{\text{flat}}$, and v_{flow} was set to 0.01, 0.01 nm/τ_0 and 5 nm/τ_0, respectively.

Figure 6.10, 6.11, and 6.12 show the snapshots of the simulation results for different times when the value of γ_+ is 0.5, 0.7 and 0.9, respectively, for three types of substrates: (a) grounded conductor, (b) floating conductor, and (c) insulator. To explore the details, we plotted the film thickness d evaluated by the same method in Chapter 6.3.2 and the surface charge density σ for the floating conductor substrates. Figure 6.13(a)－(c) shows the value of d for $\gamma_+ = 0.5, 0.7,$ and 0.9, respectively, and it is plotted for three types of the substrates. Figure 6.13(d) shows the σ for $\gamma_+ = 0.5 - 0.9$ for the floating conductive substrate.

When $\gamma_+ = 0.5$ (Figure 6.10), the numbers of the positively and negatively CNPs in the gas phase are balanced. The deposited CNPs on the floating conductor and insulator grow more faster than the grounded conductor as shown in Figure 6.10(a)－(c). The growth rates at $\gamma_+ = 0.5$ in Figure 6.13(a) indicate a markedly slow growth on the grounded conductive substrate. These results are attributable to the similar causes to those in the case of non－etching conditions.

When $\gamma_+ = 0.7$ (Figures 6.11), the numbers of the positively and negatively CNPs in the gas phase are imbalanced. In the initial stage the growth rate on the floating conductor ($t < 1500\tau_0$) and insulator ($t < 1000\tau_0$) was faster than that on the grounded

substrate. After the initial stage, the deposited CNPs were etched away instead of growing, and the thickness converges to 2 nm on floating conductor, and 1 nm on insulator. These results are attributable to the like−charge attraction in the initial stage, and repulsive interaction after that between deposited CNPs and CNPs in the gas phase.

When $\gamma_+ = 0.9$ (Figures 6.12), the charge imbalance becomes more severe than when $\gamma_+ = 0.7$. Unlike the case of $\gamma_+ = 0.7$, the deposited CNPs grow rapidly only on the insulator in the initial stage and stop growing quickly ($t \approx 200\tau_0$) on the floating conductor (d ~ 1 nm). After $t = 1000\tau_0$, the deposited CNPs were etched away and the thickness decreases to 2 nm on insulator. The deposited CNPs on the grounded conductor grow steadily and the growth rate is faster than that when $\gamma_+ = 0.7$. The cause seems to be that the attraction with the conductor substrate becomes stronger as the charge imbalance intensifies, the size of the CNPs in the gas phase becomes smaller or the charge amount increases.

According to the simulation results, it is when the numbers of positively and negatively CNPs are imbalanced ($\gamma_+ \neq 0.5$) that the simulation and experimental results show similar tendencies. That is, while CNPs are steadily deposited on the grounded conductor substrate [see Figures 6.1(a), 6.11(a), and 6.12(a)], CNPs are

deposited initially on the insulator substrate and then etched away over time [see Figures 6.1(b), 6.11(c), and 6.12(c)]. Thus, the sign of CNPs in the gas phase in the experiment appears to be imbalanced. However, in the simulation results in Figures 6.13(b) and (c), the initial growth rate on the insulator substrate is faster than that on the grounded conductor substrate, which is contrary to the experimental results in Figure 6.1. This is analyzed to be caused by the underestimation of the attraction between the CNPs in the gas phase and the grounded conductor substrate during the simulation processes. To get the simulation results closer to the experimental results, we suggest the following three considerations: 1. Considering interfacial energy effect of substrate material; 2. Increasing the gap d of CNP generation in the gas phase from the substrate; 3. Increasing the unit charge of CNPs q.

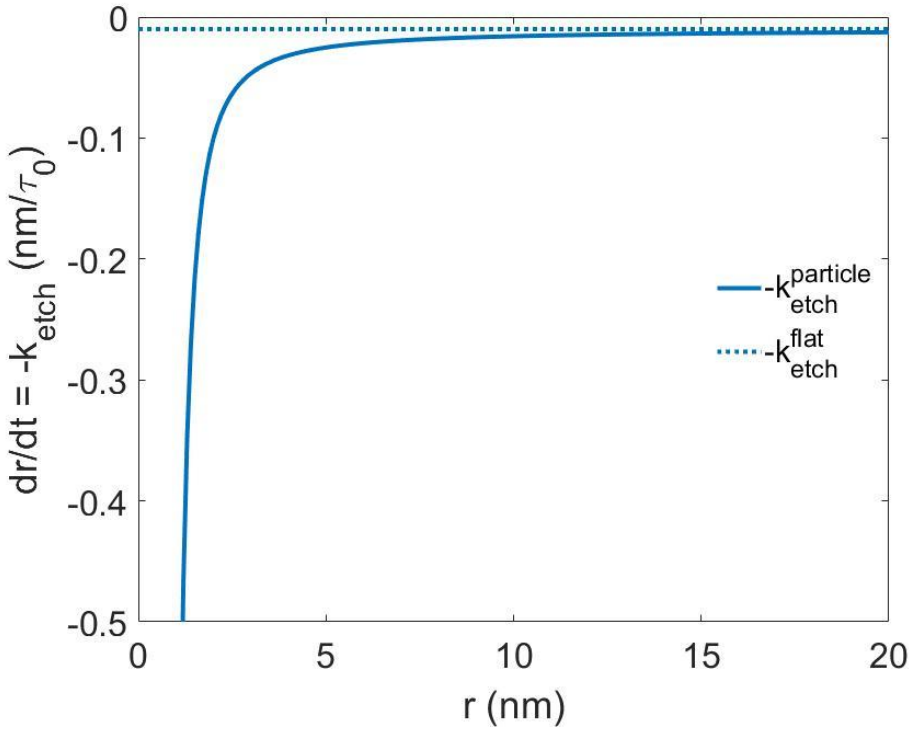

Figure 6.9 Etching rate of particle as a function of its radius r from Equation (51) using $\gamma = 1.23\,J/m^2$, $V_m = 1.206 \times 10^{-5}\,m^3/\text{mol}$ and $T = 773$ K.

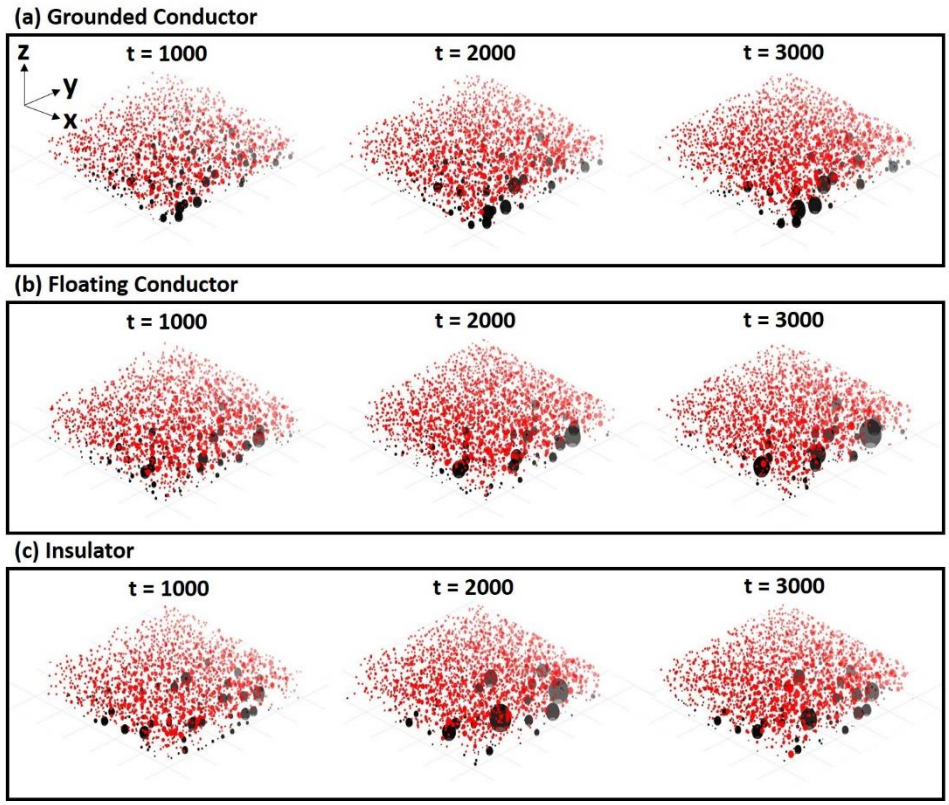

Figure 6.10 kMC simulation results: Snapshots of systems with CNPs in the gas phase and deposited CNPs at different simulation times (τ_0). Three types of the substrates were explored: (a) grounded conductor, (b) floating conductor, and (c) insulator. Red and black spheres represent the positions and sizes of CNPs in the gas phase and deposited CNPs, respectively. The initial parameters for simulation were $r_0 = 5\,\text{nm}$, $q_0 = \pm e$, $\gamma_+ = 0.5$, $\eta = 0.01$, $T = 773\,\text{K}$, $k_{\text{etch}}^{\text{flat}} = 0.01\,\text{nm}/\tau_0$, and $v_{\text{flow}} = 5\,\text{nm}/\tau_0$. The dimensions of each displayed domain were $1000 \times 1000 \times 200\,\text{nm}^3$.

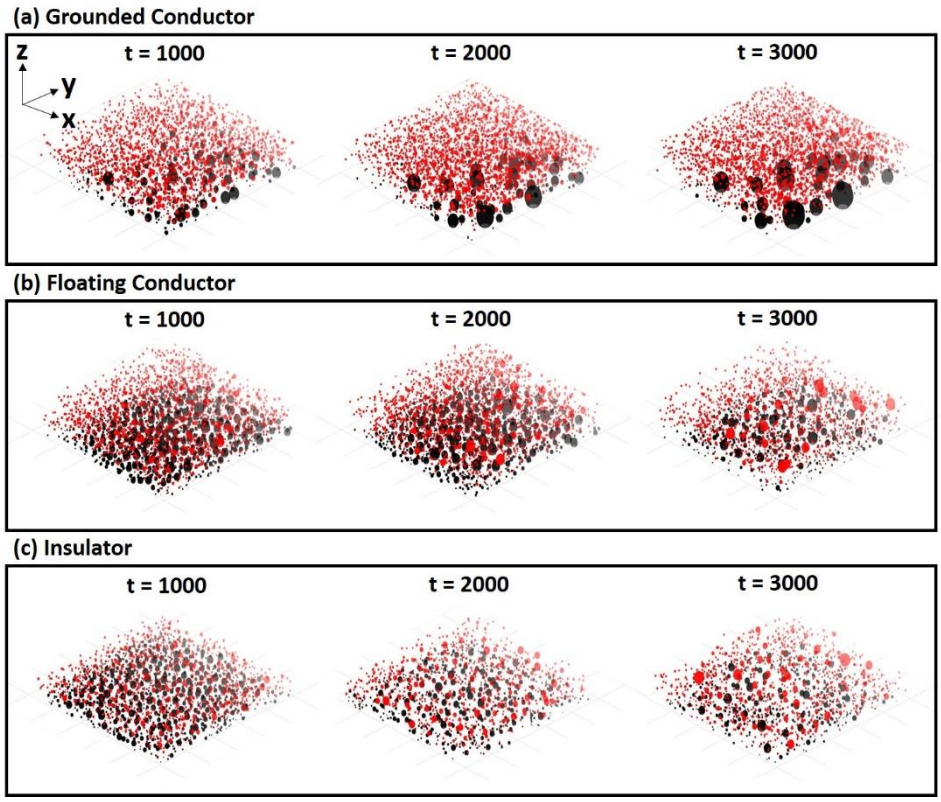

Figure 6.11 kMC simulation results: Snapshots of systems with CNPs in the gas phase and deposited CNPs at different simulation times (τ_0). Three types of the substrates were explored: (a) grounded conductor, (b) floating conductor, and (c) insulator. The simulation parameters are same with those of Figure 6.10 except for $\gamma_+ = 0.7$.

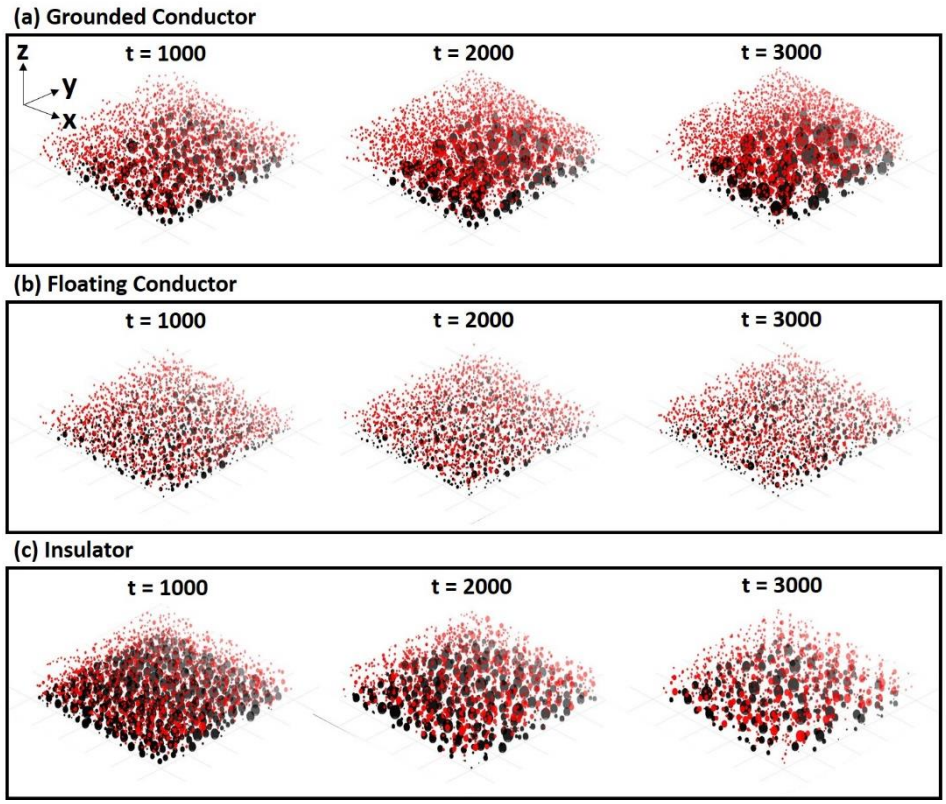

Figure 6.12 kMC simulation results: Snapshots of systems with CNPs in the gas phase and deposited CNPs at different simulation times (τ_0). Three types of the substrates were explored: (a) grounded conductor, (b) floating conductor, and (c) insulator. The simulation parameters are same with those of Figure 6.10 except for $\gamma_+ = 0.9$.

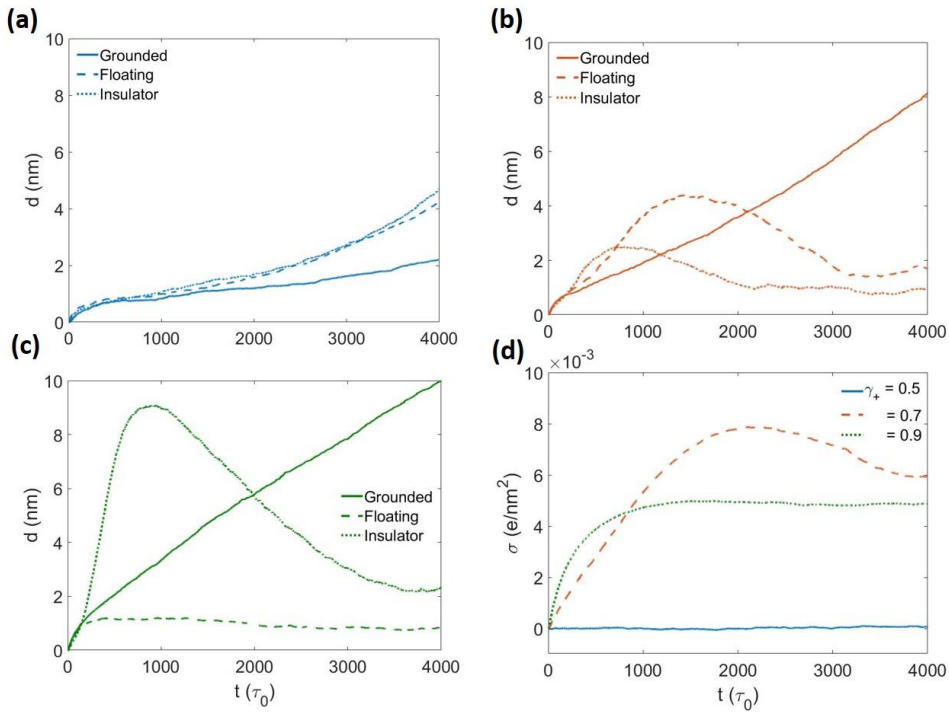

Figure 6.13 The film thickness d as a function of t (τ_0), as indicated by the kMC simulation results of (a) Figure 6.10 ($\gamma_+ = 0.5$), (b) Figure 6.11 ($\gamma_+ = 0.7$), and (c) Figure 6.12 ($\gamma_+ = 0.9$). The solid, dashed and dotted line denotes the thickness on the grounded conductor, floating conductor, and insulator substrate, respectively. (d) The surface charge density σ of the floating substrate for $\gamma_+ = 0.5 - 0.9$.

6.4. Conclusion

Using kMC simulations, the growth behaviors and rates of deposited CNPs were investigated by varying the electrical property of the substrates: grounded conductor, floating conductor and insulator. When the CNPs are balanced, $\gamma_+ = 0.5$, the results of the kMC simulation showed that the growth rates were accelerated when the substrate is floating conductor or insulator compared to the grounded conductor. When the CNPs are imbalanced, $\gamma_+ = 0.7$, and 0.9, the long-term growth rate on the grounded substrate was the fastest. On the floating conductor and the insulator substrate, the growth was restricted by charge accumulation after a certain period of time where growth proceeded. Especially, although the growth rate on the insulator substrate was faster than that on the grounded conductor in initial stage by strong like-charge attraction, the deposited CNPs were etched away by repelling with the CNPs in the gas phase after charge accumulation. The simulation results correspond to the experimental results and hypothesis: 1. The growth rate was faster on the floating substrate than grounded substrate when the CNPs are balanced and in non-etching condition; 2. The CNPs are selectively deposited on the grounded

conductor substrate rather than on the insulator substrate when the CNPs are in etching atmosphere.

Chapter 7. Effects of electrostatic interaction on anisotropic growth of nanowire

7.1. Introduction

In the previous results, Hwang et al. [95] grew Si nanowires without any catalytic metals and in a reducing atmosphere, using the CVD reactor where the gas ratio condition for the growth was SiH_4 : HCl : H_2 = 3 : 1 : 96 with a reactor pressure of 10 Torr and a substrate temperature of 950 ℃. Figure 7.1 shows the evolution of microstructures after 3 min on (a) Mo, (b) Si, (c) SiO_2, and (d) Si_3N_4 substrates. Figure 7.1(a) shows a silicon film was deposited on the Mo substrate which is a conductor. However, on the Si substrate nanowires started to form as shown in Figure 7.1(b), and considerable amounts of nanowires grew on SiO_2 and Si_3N_4 substrates as can be seen in Figure 7.1(c) and (d), respectively.

Similarly, as mentioned in Chapter 1, Youn et al. [23] also reported that Si nanowires were deposited on the floating substrate whereas Si film was deposited on the conductor substrate when flow rate of N_2 is 500 sccm. [see Figure 1.6]. Besides, the growth of nanowires without catalytic metals was observed and reported in many studies. [96-99]

The proposed nanowire growth mechanisms include the vapor-

liquid-solid (VLS) [39] and oxide-assisted growth (OAG) [40] mechanisms. However, since either catalytic metal or seed of silicon oxide should exist for the suggested mechanisms, other nanowire growth mechanisms clearly exist considering the experimental results.

Considering the results of nanowire growth only on a floating substrate and the generation of the CNPs in the gas phase, [23,95] the electrostatic interaction between CNPs in the gas phase and the deposited nanowires composed of CNPs should affect the anisotropic growth of the Si nanowires. Youn et al. [23] and Hwang [21, pp.177-179] qualitatively explained the electrostatic interaction effects: When a positively CNP approaches a positively-charged nanowire in the radial (side) direction, the electrostatic interaction would be repulsive. On the other hand, when it approaches in the axial (tip) direction, the interaction would be attractive. Thus, the small CNPs would be selectively deposited in the axial-tip direction, leading to extensive anisotropic growth of nanowires.

Nevertheless, quantitative analysis is still needed to analyze the effects of the electrostatic interaction on the anisotropic growth of nanowires. For this, the electrostatic potential energy of CNP-charged nanowire system was calculated through FEM in this chapter. We explored how the electrostatic interactions affect the anisotropic

growth of the nanowires by CNPs in the gas phase and investigate the underlying physical mechanism.

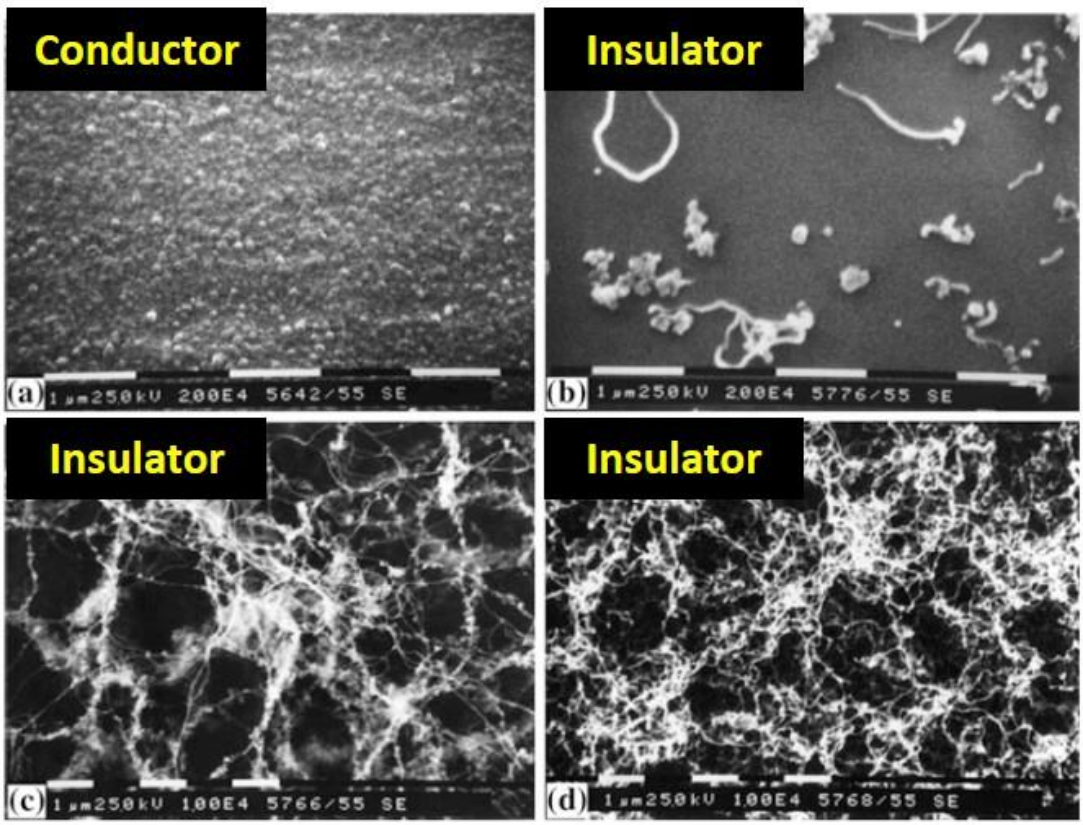

Figure 7.1 Microstructures evolution on (a) Mo, (b) Si, (c) SiO_2, (d) Si3N4 substrates after 3 min deposition under 10 Torr of reactor pressure and 950 ℃ of temperature substrate with a gas ratio of SiH_4 : HCl : H_2 = 3 : 1 : 96. [95]

7.2. Computational Details

FEM described in detail in Chapter. 3.2.2 was used to solve the Poisson's equation expressed in Equations (9) and (10) for calculating the electrostatic potential energy W and surface charge density.

The charged nanowire was modelled as rod with hemispherical tips of radius r and length $L = 2rN$ from tip to tip where N is the number of CNPs constituting the charged nanowire. The CNP was modelled as sphere with radius of r [see Figure 7.2]. Note that the radii of the charged nanowire tip and the CNP are same. They were considered solid conductors of continuum matter. We used a spherical infinite element domain scheme with a finite radius of R_∞, implemented in COMSOL. The CNP and the charged nanowire were placed in a vacuum with a relative permittivity of 1. A fine mesh of approximately 180,000 tetrahedral quadratic Lagrange elements was used. The elements of the boundaries of rod and sphere were manually adjusted for higher accuracy, while the other elements were automatically generated with the 'fine' mesh setting in COMSOL. The outer surface of the infinite element domain was set to ground, and the surface charges of the charged nanowire and CNP were set to Q and q, respectively. At first, the xy−plane was divided into $5 \times 5\ \mathrm{nm}^2$

square meshes, CNPs were placed at each vertex, and the electrostatic energy was plotted to observe the overall energy distribution. Next, we varied the separation distance s between the surfaces of the charged nanowire and CNP in the side [Figure 7.2(a)] and tip [Figure 7.2(b)] directions to calculate the potential energy and surface charge density of the system.

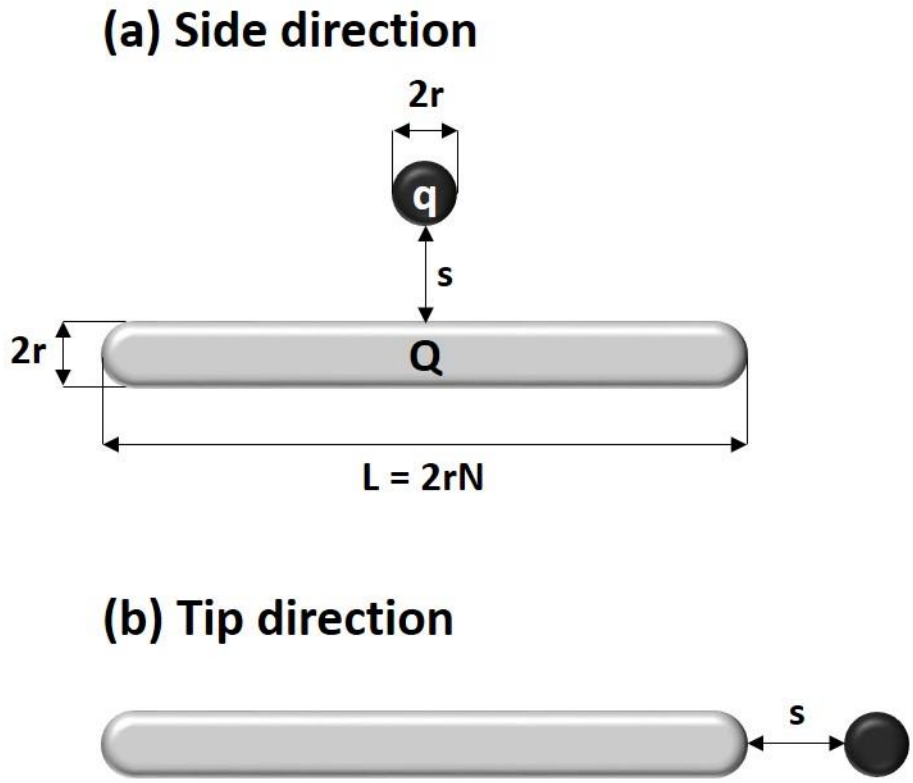

Figure 7.2 A system of a charged nanowire and a CNP. The separation distance s is varied in (a) the side direction and (b) the tip direction of the charged nanowire.

7.3. Results and Discussions

First, we calculated the electrostatic potential energy W by dividing the xy−plane into $5 \times 5\ \mathrm{nm}^2$ square meshes and placing the CNPs with $q = +e, r = 10\ \mathrm{nm}$ at each vertex. Here, the charged nanowire with $Q = +5e, N = 30, r = 10\ \mathrm{nm}$ was fixed at the origin. Figure 7.3 shows the value of W using color bar where red is high energy and blue is low energy. Comparing the energy barriers in side (red color in Figure 7.3, 0.3536 eV) and tip (green color in Figure 7.3, 0.3373 eV) directions, it can be seen that a significantly smaller potential energy barrier exists in the tip direction.

To explore the energy barrier difference between the tip and side directions in more detail, we calculated values of W as a function of separation distance s in side and tip directions, excluding self−energy of the charged nanowire and the CNP, in Figure 7.4 as a representative example. The calculation parameters $r, N, Q,$ and q were $3\ \mathrm{nm}$, 10, $+5e$, and (a) $+e$, (b) $-e$, respectively.

When they have same sign of charges, the electrostatic interaction is always repulsive: W, excluding self−energy, decreases as separation distance s increases as shown in Figure 7.4(a). Comparing the energy gradient of each direction, approaching in the tip direction has a weaker repulsive interaction

than approaching in the side direction when a CNP approaches the charged nanowire.

Conversely, when they have opposite charges, the electrostatic interaction is always attractive: W, excluding self-energy, increases as separation distance s increases as shown in Figure 7.4(b). Approaching in the side direction has a stronger attractive interaction than approaching in the sip direction.

From the results, when they have the same sign of charge, the CNPs favor deposition at the tip of the charged nanowires, resulting in one-dimensional growth or anisotropic growth. On the other hand, when they have opposite charges, the CNPs are more likely to deposit on the side of the charged nanowire, which hinders anisotropic growth. Therefore, for the nanowire to grow anisotropically by electrostatic interaction, the charge sign of the CNPs should be imbalanced, so interactions between the charged nanowires and CNPs with the same sign mainly exist.

To establish a criterion for the energy barrier difference, the probability $P \sim \exp(-\Delta W/k_{\mathrm{B}}T)$ to overcome the potential energy barrier ΔW from the Arrhenius equation was considered. In this study, the energy barrier is considered as $\Delta W = W_f - W_i = W_{max} - W(s = 100\ \mathrm{nm})$ where W_{max} is the largest energy value at $s < 100\ \mathrm{nm}$, and $W(s = 100\ \mathrm{nm})$ is the energy value when $s = 100\ \mathrm{nm}$

[see Figure 7.4(a)]. Then, the ratio of probability to overcome the energy barrier in each direction is expressed by $\frac{P_{\mathrm{tip}}}{P_{\mathrm{side}}} \sim \exp[(\Delta W_{\mathrm{side}} - \Delta W_{\mathrm{tip}})/k_{\mathrm{B}}T]$, and the numerator inside the exponential term $(\Delta W_{\mathrm{side}} - \Delta W_{\mathrm{tip}})$, the energy barrier difference, was used as a measure to evaluate the anisotropic growth of charged nanowires.

For the anisotropic growth of the charged nanowires, energy barrier difference $(\Delta W_{\mathrm{side}} - \Delta W_{\mathrm{tip}})$ determine the direction of growth where the greater the difference, the greater the probability of growing in the tip direction. To understand the characteristic of $(\Delta W_{\mathrm{side}} - \Delta W_{\mathrm{tip}})$, we examined the value of W/q^2 as a function of s for different Q/q and N values. Figure 7.5(a) and (b) compare the value of W/q^2 for different Q/q (1−50) and different N values (5−50), respectively. Note that for same value of Q/q, the value of W/q^2 was same and plotted in Figure 7.5. For that reason, $[(\Delta W_{\mathrm{side}} - \Delta W_{\mathrm{tip}})/q^2]$ was evaluated, which allowed us to consider a wider range of conditions.

The value of $[(\Delta W_{\mathrm{side}} - \Delta W_{\mathrm{tip}})/q^2]$ increases as the value of Q/q increases as shown in Figure 7.5(a). At Q/q values of 1, 5, 10, 25, and 50, the value of $[(\Delta W_{\mathrm{side}} - \Delta W_{\mathrm{tip}})/q^2$ are 0.021, 0.111, 0.236, 0.662, and 1.302 eV/e^2, respectively, when $r = 3\ \mathrm{nm}$ and $N = 10$. This indicates that for any fixed value of q (charge of CNP) the

higher the value of Q (charge of charged nanowire) the higher the probability of anisotropic growth.

The value of $[(\Delta W_{\text{side}} - \Delta W_{\text{tip}})/q^2]$ decreases as the value of N increases as shown in Figure 7.5(b). At N values of 5, 10, 25, and 50, the value of $[(\Delta W_{\text{side}} - \Delta W_{\text{tip}})/q^2]$ are 0.1533, 0.111, 0.057, and 0.034 eV/e^2, respectively, when $r = 3\,\text{nm}$ and $Q/q = 5$, which indicates that longer lengths of charged nanowires are detrimental to its anisotropic growth.

In order to explore the tendency of the energy barrier difference $[(\Delta W_{\text{side}} - \Delta W_{\text{tip}})/q^2]$ depending on the value of Q/q and N under more conditions, the value of $[(\Delta W_{\text{side}} - \Delta W_{\text{tip}})/q^2]$ was plotted three-dimensionally as multivariate function of Q/q and N with its fitting surface in Figure 7.6. The results in Figure 7.6 shows the energy barrier difference values increase with increasing value of charge ratio Q/q corresponding with the results of Figure 7.5. In the case of N, there exists appropriate value of nanowire length N that maximizes the energy barrier difference. Note that when N is 1, the nanowire becomes spherical and isotropic, which cancels the energy barrier difference.

Assuming a situation where charged nanowires grow, the gradual growth of the charged nanowire is an increase in the N value regardless of the degree of balance of the CNP sign. As

shown in Figure 7.6, comparing the growth paths when the CNP sign ratio is balanced and imbalanced, it appears that the electrostatic energy barrier physically induces the anisotropic growth of nanowires in the imbalanced CNP sign ratio by charge accumulation on the charged nanowires. The balanced CNP sign ratio does not appear to physically contribute to the anisotropic growth of the charged nanowires at all due to no charge accumulation.

To further understand the physical origin of the electrostatic interaction between charged nanowire and CNP, we investigated the surface charged redistribution of them, which is induced by their mutual polarization, by calculating their surface charged density. We obtained the induced charge density σ_{ind} associated with the surface charge redistribution. (For related details, see Chapter 3.3.2.)

Figures 7.7 (a) and (b) show the results calculated with $r = 3\,\mathrm{nm},\ s = 5\,\mathrm{nm},\ q = +e,\ N = 10,\ Q = +10e$ in (a) side; (b) tip direction, respectively. For comparison, Figures 7.7 (c) – (f) show the calculated surface charge density under the same conditions as Figures (a) and (b) expect for (c) and (d) $Q = +5e;$ (e) and (f) $N = 50$. Here, Figures 7.7 (c) and (e) show when the CNP is near the side surface of the charged nanowire, and Figures 7.7 (d) and

(f) show when it is near the tip surface of the charged nanowire. In the color scale of Figure 7.7, the reddest and bluest colors represent the most positive and negative values of σ_{ind}, respectively.

Figure 7.7(a) and (b) unveil the physical origin of the energy barrier difference. When the CNP is near the side surface of the charged nanowire [Figure 7.7(a)], the negative charges are induced on the surface area of the CNP and charged nanowire adjacent to each other, which will induce their repulsive interaction. The positive charges are induced on the opposite surface of the CNP and both tips of the charge nanowire. When the CNP is near the tip surface of the charged nanowire [Figure 7.7(b)], the charge density distribution on the CNP is similar with that of Figure 7.7(a). In the case of the charged nanowire, the positive charges are induced on the both tips, but weaker positive charges on the adjacent tip to the CNP are induced than the opposite one. The opposite charges on their adjacent surface area induce their attractive interaction. The results in Figures 7.7(a) and (b) well explain why ΔW_{side} is larger than ΔW_{tip} when they have like charge.

When the value of Q decreases to $+5e$ and the CNP is near the side surface [Figure 7.7(c)], the induced negative charges on their surface area of the CNP and charged nanowire adjacent to each

other are weaker compared with those in Figure 7.7(a), which makes weaker repulsive interaction. When the CNP is near the tip surface [Figure 7.7(d)], weak negative charges are induced on the tip surface adjacent to the CNP, which induces repulsive interaction between the CNP and the charged nanowire. The results in Figures 7.7(a)−(d) correspond with the results in Figures 7.5(a) and 7.6 where the value of $[(\Delta W_{\text{side}} - \Delta W_{\text{tip}})/q^2]$ increases with increasing value of Q/q.

When the value of N increases to 50 and the CNP is near the side surface [Figure 7.7(e)], the charges on the CNP are hardly induced while the negative charges are still charged on the side surface area. This indicates the repulsive interaction between them is significantly weaker than that in Figure 7.7(a). When the CNP is near the tip surface, the CNP and the charged nanowire have weak repulsive interaction as shown in Figure 7.7(f). Considering the induced charge on the CNP is very weak regardless of its position, the energy barrier difference should be small. These results well explain the results in Figures 7.5(a) and 7.6 where the value of $[(\Delta W_{\text{side}} - \Delta W_{\text{tip}})/q^2]$ decreases with increasing value of N.

To confirm the correlation between nanostructure and charge ratio of the CNPs, the experimentally measured number concentration of CNPs was investigated with the deposited

structures. Table 7.1 shows that the charge ratio γ_+ of all CNPs and CNPs smaller than 30 nm by experimentally observed using DMA−FCE system shown in Figure 1.4. Values of γ_+ greater than 0.7 or less than 0.3 are indicated in bold as a criterion for charge imbalance. Considering the possibility that larger CNPs could have more charges, the value of γ_+ are displayed in two ways, the number ratio and the volume ratio of the CNPs with the materials and observed nanostructures. The value of d means the diameter for nanowires, nanosheets, CNTs and particles, the thickness for films, and the size for hexagons. In order for nanowires to grow in CNP units, the diameter of the CNP should be similar to or smaller than that of the nanowire. Kim et al. [35] reported that the nanowires were not deposited but the particles were deposited when CNPs smaller than 30 nm were absent and the size of deposited particles was similar with the diameter of the highest number concentration. Thus, assuming that the maximum size of CNP involved in nanowire growth is 30 nm, the charge ratio of CNPs smaller than 30 nm were also investigated as shown in Table 7.1.

When Si nanowires were deposited on the floating substrate by Youn et al. [39], the values of γ_+ for the CNPs smaller than 30 nm

were 0.89 and 0.88 for the number and volume, respectively, which corresponds to the calculation results. For other Si nanowires deposition results by Kim et al. [35], however, the values of γ_+ for the CNPs smaller than 30 nm were ranged from 0.16 to 0.62. In this case, there are γ_+ values around 0.5 where charge is balanced in 6 out of 8 cases, so it seems that a factor other than electrostatic interaction affects it. For GaN, [38] ZnO nanowires, [33] CNT and Carbon nanofiber deposition, [34] most of the values of γ_+ for the CNPs smaller than 30 nm were greater than 0.7 and less than 0.3, which is consistent with the calculation results.

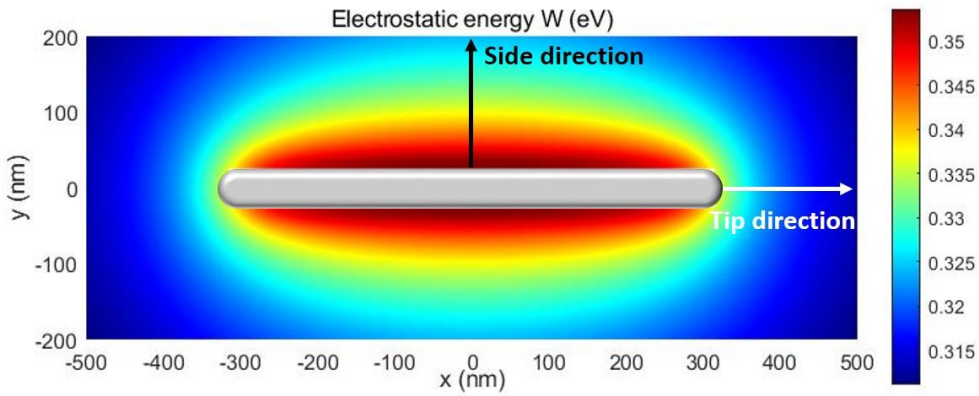

Figure 7.3 Contour of electrostatic potential energy W when the center of charged nanowire with $Q = +5e, N = 30, r = 10\ \mathrm{nm}$ is fixed at the origin. The color at each position means the W value of the system when the CNP with $q = +e, r = 10\ \mathrm{nm}$ is located there.

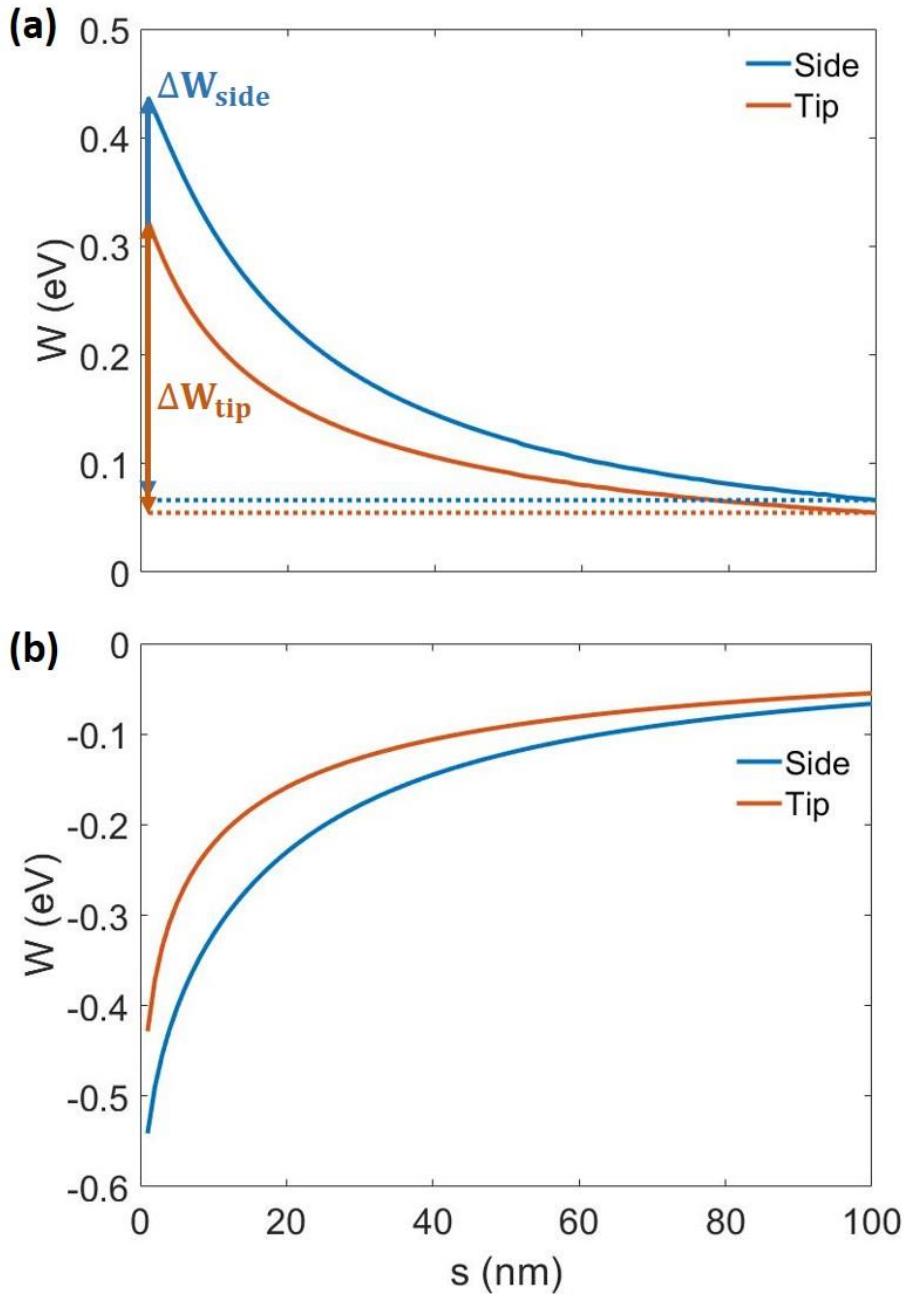

Figure 7.4 W, excluding self−energy, as a function of s in the side and tip directions for the charge nanowire and CNP system, with $r = 3\,\text{nm},\ N = 10, Q = +5e,$ and (a) $q = +e$; (b) $q = -e$.

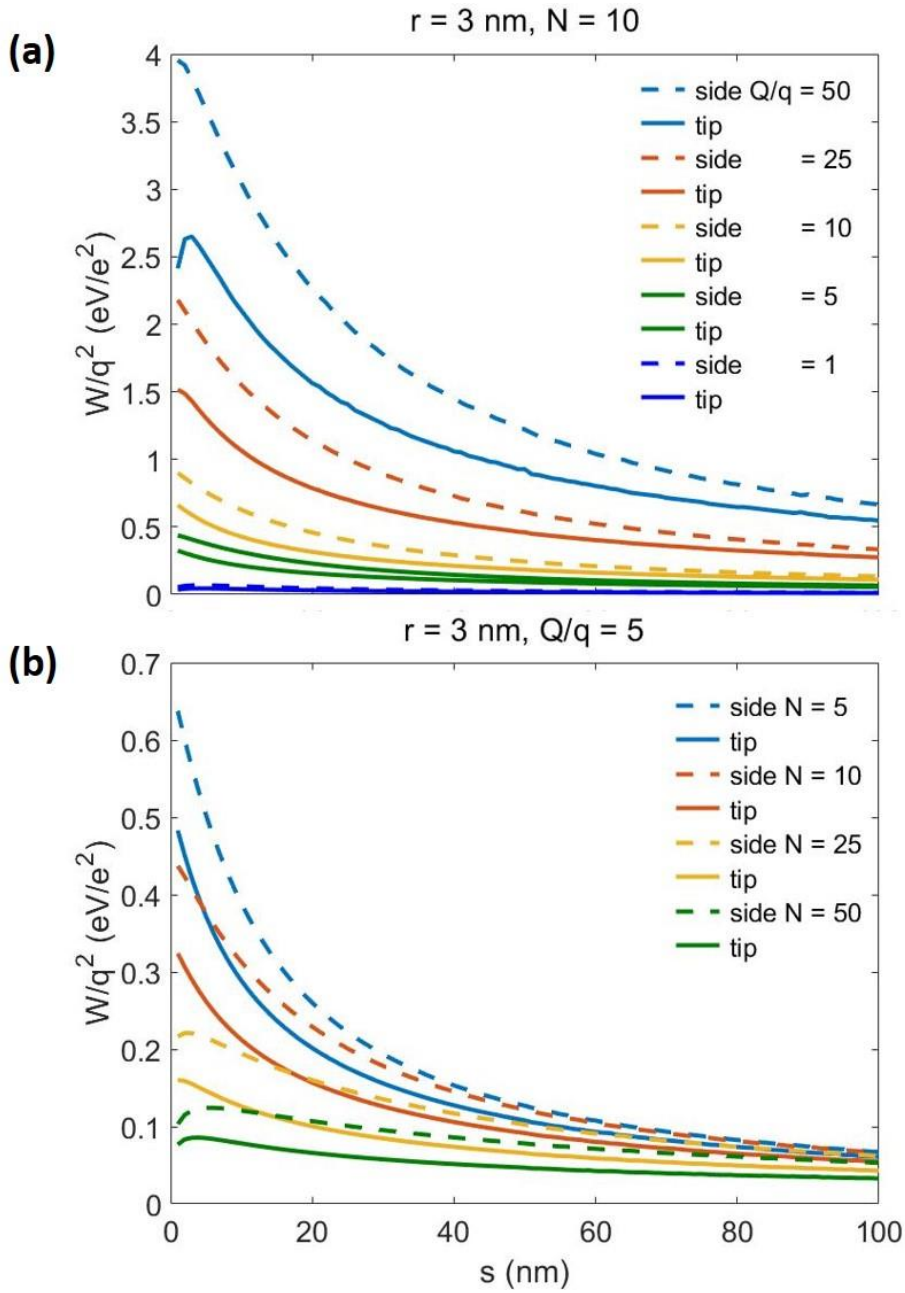

Figure 7.5 W, excluding self−energy, divided by q^2 as a function of s in the side (dashed lines) and tip (solid lines) directions for the charged nanowire and CNP system ($r = 3$ nm). (a) $N = 10$, $Q/q : 1 - 50$; (b) $Q/q = 5$, $N : 5 - 50$.

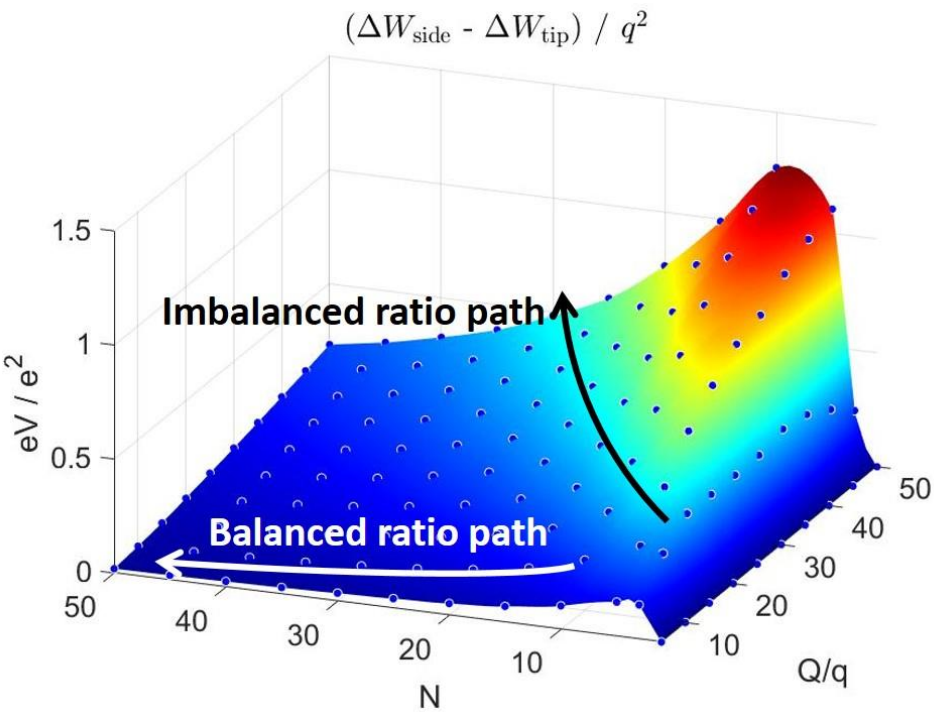

Figure 7.6 $(\Delta W_{\text{side}} - \Delta W_{\text{tip}})/q^2$ as multivariate function of Q/q and N for the charged nanowire and CNP system ($r = 3$ nm). The blue dots represent the calculated values and the surface to which the values are fitted is displayed using piecewise cubic interpolation.

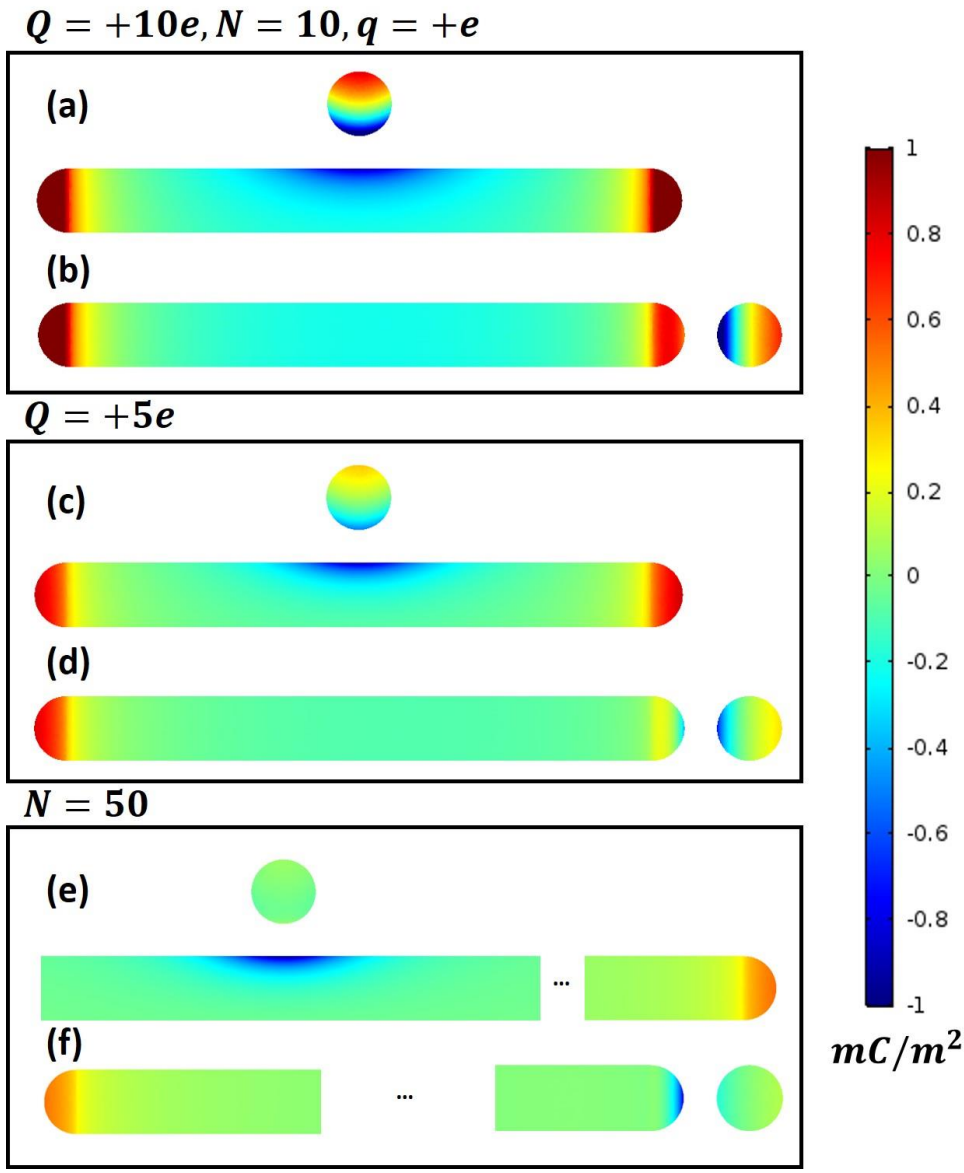

Figure 7.7 Induced surface charge densities of the charged nanowire and CNP system ($r = 3$ nm, $s = 5$ nm, $q = +e$, (a)−(b) $Q = +10e$, $N = 10$; (c)−(d) $Q = +5e, N = 10$; (e)−(f) $Q = +10e, N = 50$. The CNP is positioned at (a), (c), (e) side direction; (b), (d), (f) tip direction of the charged nanowire.

Table 7.1 The charge ratio γ_+ of all CNPs and CNPs smaller than 30 nm by experimentally observed using DMA−FCE system. The value of γ_+ is displayed in two ways, the number ratio and the volume ratio of the CNPs with the materials and observed nanostructures.

Materials	Structures	d (nm)	γ_+ (total)		γ_+ (r<30 nm)		Ref.
			Num	Vol	Num	Vol	
Si	Film	190 - 220	.54	.56	.53	.52	[23]
	Nanowire	~10 - 30	.56	.60	**.11**	**.12**	
	Particles	~50	.54	.57	Not observed		[35]
		~110	.53	.54			
	Nanowire	~50	.57	.53	**.16**	**.20**	
		~50	.52	.51	.54	.56	
		~50	.55	.58	.39	.40	
		~24	.57	.62	.56	.59	
		~35	.54	.55	.55	.56	
		~61	.63	.59	**.17**	**.19**	
		~65	.54	.53	.52	.54	
		~40	.57	.58	.62	.62	
GaN	Nanowire	~20 - 30	**.02**	**.00**	**.10**	**.12**	[38]
	Hexagon	~1000	.50	.55	Not observed		
		~560	.24	.32			
ZnO	Nanowire	~100	**.30**	.36	**.30**	.36	[33]
		~100	**.30**	.32	**.27**	**.28**	
	Nanosheets	~100	**.10**	**.15**	**.10**	**.15**	
		~100	.42	.58	.42	.58	
		~100	**.10**	**.16**	**.10**	**.16**	
	Rugged Structure	−	.50	.40	.50	.40	
C	CNT	~20	.52	.33	.52	.33	[34]
		~60	**.79**	**.78**	**.88**	**.89**	
		~130	.52	.52	.53	.52	
		~210	**.85**	**.86**	**.85**	**.86**	
		~290	**.86**	**.80**	**.96**	**.97**	
		~300	.34	**.30**	.39	.35	
		−	**.85**	**.85**	**.87**	**.88**	
	Nanofiber	−	**.82**	**.71**	**.86**	**.84**	

7.4. Conclusion

Using FEM, the electrostatic potential energy was calculated for the CNP–charged nanowire systems and how it affected to the anisotropic growth of the charged nanowires under the CNP–existing system was investigated. The calculation results showed that the electrostatic interaction favors the anisotropic growth when the CNP in the gas phase and deposited charged nanowire have like–charge: CNPs approaching in the tip direction have weaker repulsive interaction than those approaching in the side direction. When they have opposite charge, the electrostatic interaction adversely affects the anisotropic growth by CNPs approaching in the side direction having stronger attractive interaction than those approaching in the tip direction. Comparing the energy barrier difference $\Delta W_{\mathrm{side}} - \Delta W_{\mathrm{tip}}$ when CNP approaches to the charge nanowire in each direction, higher charge ratios of charged nanowire to CNP Q/q tend to favor anisotropic growth. In the case of nanowire length, there exists appropriate value of nanowire length that maximizes the energy barrier difference. For electrostatic potential energy to physically affect the anisotropic growth of nanowires by CNPs, the sign ratio of CNPs should be imbalanced.

Bibliography

[1]P. Hartman, "Crystal growth: an introduction," 1973.

[2]J. Van Der Eerden, "Handbook of crystal growth vol. 1a: Bulk fundamentals, growth thermodynamics and kinetics ed DTJ Hurle," 1994.

[3]J. J. De Yoreo and P. G. Vekilov, "Principles of crystal nucleation and growth," *Rev. Mineral. Geochem.*, vol. 54, no. 1, pp. 57–93, 2003.

[4]N.–M. Hwang and D.–Y. Kim, "Charged clusters in thin film growth," *Int. Mater. Rev.*, vol. 49, no. 3–4, pp. 171–190, 2004.

[5]H. Cöelfen and M. Antonietti, "Mesocrystals and nonclassical crystallization," 2008.

[6]Q. Zhang, S.–J. Liu, and S.–H. Yu, "Recent advances in oriented attachment growth and synthesis of functional materials: concept, evidence, mechanism, and future," *J. Mater. Chem.*, vol. 19, no. 2, pp. 191–207, 2009.

[7]D. Gebauer and H. Cölfen, "Prenucleation clusters and non–classical nucleation," *Nano Today*, vol. 6, no. 6, pp. 564–584, 2011.

[8]H.–G. Liao, L. Cui, S. Whitelam, and H. c, "Real–time imaging of Pt_3Fe nanorod growth in solution," *Science*, vol. 336, no. 6084, pp. 1011–1014, 2012.

[9]Z. Tang, N. A. Kotov, and M. Giersig, "Spontaneous organization of single CdTe nanoparticles into luminescent nanowires," *Science*, vol. 297, no. 5579, pp. 237–240, 2002.

[10]J. M. Yuk, M. Jeong, S. Y. Kim, H. K. Seo, J. Kim, and J. Y. Lee, "In situ atomic imaging of coalescence of Au nanoparticles on graphene: rotation and grain boundary migration," *Chem. Commun.*, vol. 49, no. 98, pp. 11 479–11 481, 2013.

[11]E. Sutter, P. Sutter, A. V. Tkachenko, R. Krahne, J. De Graaf, M. Arciniegas, and L. Manna, "In situ microscopy of

the self-assembly of branched nanocrystals in solution," *Nat. Commun.*, vol. 7, no. 1, pp. 1-7, 2016.

[12]E. R. Leite and C. Ribeiro, "Crystallization and growth of colloidal nanocrystals," 2011.

[13]M. Niederberger and H. Cölfen, "Oriented attachment and mesocrystals: non-classical crystallization mechanisms based on nanoparticle assembly," *Phys. Chem. Chem. Phys.*, vol. 8, no. 28, pp. 3271-3287, 2006.

[14]V. K. Ivanov, P. P. Fedorov, A. Y. Baranchikov, and V. V. Osiko, "Oriented attachment of particles: 100 years of investigations of non-classical crystal growth," *Russ. Chem. Rev.*, vol. 83, no. 12, p. 1204, 2014.

[15]B. Jin, Z. Liu, and R. Tang, "Recent experimental explorations of non-classical nucleation," *CrystEngComm*, vol. 22, no. 24, pp. 4057-4073, 2020.

[16]H. Pan and R. Tang, "Towards an understanding of crystallization by attachment," *Crystals*, vol. 10, no. 6, p. 463, 2020.

[17]T. Yoshida, "Vapour phase deposition of cubic boron nitride," *Diamond Relat. Mater.*, vol. 5, no. 3-5, pp. 501-507, 1996.

[18]P. R. i Cabarrocas, "Plasma enhanced chemical vapor deposition of amorphous, polymorphous and microcrystalline silicon films," *J. Non-Cryst. Solids*, vol. 266, pp. 31-37, 2000.

[19]C. Zhang, L. M. Anovitz, J. P. Patterson, A. M. Rakowski, S. Le, X. Lu, X. Nie, M. Zong, F. Dong, A. F. Ogata *et al.*, "Crystallization via nonclassical pathways volume 1: Nucleation, assembly, observation & application," 2020.

[20]X. Zhang, V. P. Christine, and W. Lijun, "Crystallization via nonclassical pathways volume 2: Aggregation, biomineralization, imaging & application," 2021.

[21]N. M. Hwang, "Non-classical crystallization of thin films and nanostructures in CVD and PVD processes," 2016.

[22]N.-M. Hwang and D.-K. Lee, "Charged nanoparticles in thin film and nanostructure growth by chemical vapour deposition," *J. Phys. D: Appl. Phys.*, vol. 43, no. 48, p. 483001, 2010.

[23]W.-K. Youn, S.-S. Lee, J.-Y. Lee, C.-S. Kim, N.-M. Hwang, and S. Iijima, "Comparison of the deposition behavior of charged silicon nanoparticles between floating and grounded substrates," *J. Phys. Chem. C*, vol. 118, no. 22, pp. 11 946-11 953, 2014.

[24]J.-S. Jung and N.-M. Hwang, "Non-classical crystallization of thin films and nanostructures in CVD process," *Chemical Vapor Deposition: Recent Advances and Applications in Optical, Solar Cells and Solid State Devices*, p. 23, 2016.

[25]J.-S. Jung, S.-H. Lee, D.-S. Kim, K.-S. Kim, S.-W. Park, and N.-M. Hwang, "Non-classical crystallization of silicon thin films during hot wire chemical vapor deposition," *J. Cryst. Growth*, vol. 458, pp. 8-15, 2017.

[26]S.-H. Park, J.-W. Park, S.-M. Yang, K.-H. Kim, and N.-M. Hwang, "Effect of electric bias on the deposition behavior of ZnO nanostructures in the chemical vapor deposition process," *J. Phys. Chem. C*, vol. 119, no. 44, pp. 25 047-25 052, 2015.

[27]D.-S. Kim and N.-M. Hwang, "Synthesis of nanostructures using charged nanoparticles spontaneously generated in the gas phase during chemical vapor deposition," *J. Phys. D: Appl. Phys.*, vol. 51, no. 46, p. 463002, 2018.

[28]S.-W. Park, G.-S. Jang, K.-S. Kim, and N.-M. Hwang, "Comparison of plasma effect on dewetting kinetics of Sn films between grounded and floating substrates," *Electron. Mater. Lett.*, vol. 16, no. 1, pp. 72-80, 2020.

[29]D. Kim, D. Y. Kim, J. H. Kwon, K.-S. Kim, and N.-M. Hwang, "Generation of charged SiC nanoparticles during HWCVD process," *Electron. Mater. Lett.*, vol. 16, no. 5, pp. 498-505, 2020.

[30]Y. Lee, H. N. Han, W. Kim, and N. M. Hwang, "Effect of bipolar charging of SiH_4 on the growth rate and crystallinity

of silicon films grown in the atmospheric pressure chemical vapor deposition process," *Electron. Mater. Lett.*, vol. 16, no. 4, pp. 385-395, 2020.

[31]N. M. Hwang, J. H. Hahn, and D. Y. Yoon, "Charged cluster model in the low pressure synthesis of diamond," *J. Cryst. Growth*, vol. 162, no. 1-2, pp. 55-68, 1996.

[32]J.-M. Huh, D.-Y. Yoon, D.-Y. Kim, and N.-M. Hwang, "Effect of substrate materials in the low-pressure synthesis of diamond: approach by theory of charged clusters," *International Journal of Materials Research*, vol. 96, no. 3, pp. 225-232, 2022.

[33]C.-S. Kim, Y.-B. Chung, W.-K. Youn, and N.-M. Hwang, "Generation of charged nanoparticles during synthesis of ZnO nanowires by carbothermal reduction," *Aerosol Sci. Technol.*, vol. 43, no. 2, pp. 120-125, 2009.

[34]C.-S. Kim, Y.-B. Chung, W.-K. Youn, and N.-M. Hwang, "Generation of charged nanoparticles during the synthesis of carbon nanotubes by chemical vapor deposition," *Carbon*, vol. 47, no. 10, pp. 2511-2518, 2009.

[35]C.-S. Kim, I.-J. Kwak, K.-J. Choi, J.-G. Park, and N.-M. Hwang, "Generation of charged nanoparticles during the synthesis of silicon nanowires by chemical vapor deposition," *J. Phys. Chem. C*, vol. 114, no. 8, pp. 3390-3395, 2010.

[36]W.-K. Youn, C.-S. Kim, and N.-M. Hwang, "Effect of the carrier gas flow rate on the microstructure evolution and the generation of the charged nanoparticles during silicon chemical vapor deposition," *J. Nanosci. Nanotechnol.*, vol. 13, no. 10, pp. 7127-7130, 2013.

[37]C.-S. Kim, W.-K. Youn, D.-K. Lee, K.-S. Seol, and N.-M. Hwang, "Low-temperature deposition of crystalline silicon nitride nanoparticles by hot-wire chemical vapor deposition," *Journal of crystal growth*, vol. 311, no. 15, pp. 3938-3942, 2009.

[38]S.-S. Lee, C.-S. Kim, and N.-M. Hwang, "Generation of charged nanoparticles during the synthesis of GaN nanostructures by atmospheric-pressure chemical vapor

deposition," *Aerosol Science and Technology*, vol. 46, no. 10, pp. 1100–1108, 2012.

[39]a. R. Wagner and s. W. Ellis, "Vapor–liquid–solid mechanism of single crystal growth," *Applied physics letters*, vol. 4, no. 5, pp. 89–90, 1964.

[40]R.–Q. Zhang, Y. Lifshitz, and S.–T. Lee, "Oxide–assisted growth of semiconducting nanowires," *Advanced Materials*, vol. 15, no. 7–8, pp. 635–640, 2003.

[41]J. H. Park, J. W. Yang, M. G. Byun, N. M. Hwang, J. Park, and B. D. Yu, "Charging effects on the vibrational properties of Au and Au_2 on MgO (100)," *Current Applied Physics*, vol. 36, pp. 34–42, 2022.

[42]M. G. Byun, J. W. Yang, J. H. Park, N. M. Hwang, J. Park, and B. D. Yu, "Effects of electrostatic interaction on the formation of a particle depletion zone by charged nanoparticles during the chemical vapor deposition of Si processes," *Cryst. Growth Des.*, vol. 22, no. 4, pp. 2490–2498, 2022.

[43]S. Lee, J. Lee, and N.–M. Hwang, "Yttrium oxyfluoride coating deposited with a $Y_5O_4F_7/YF_3$ suspension by suspension plasma spraying under atmospheric pressure," *Journal of Thermal Spray Technology*, vol. 31, no. 5, pp. 1508–1520, 2022.

[44]M. G. Byun, J. H. Park, J. W. Yang, N. M. Hwang, J. Park, and B. D. Yu, "The effects of electrostatic interactions on abnormal growth of particles deposited by charged nanoparticles during chemical vapor deposition of silicon," *Electronic Materials Letters*, pp. 1–11, 2022.

[45]S. Lee, J. H. Park, C. G. Park, D.–Y. Jeong, and N.–M. Hwang, "Generation of positively charged nanoparticles by fracto–emission and their deposition into films during aerosol deposition," *Applied Surface Science*, vol. 593, p. 153466, 2022.

[46]B. Yao, Y. Chan, and N. Wang, "Formation of ZnO nanostructures by a simple way of thermal evaporation," *Applied physics letters*, vol. 81, no. 4, pp. 757–759, 2002.

[47]X. Y. Kong and Z. L. Wang, "Polar-surface dominated ZnO nanobelts and the electrostatic energy induced nanohelixes, nanosprings, and nanospirals," *Appl. Phys. Lett.*, vol. 84, no. 6, pp. 975-977, 2004.

[48]X. Y. Kong, Y. Ding, R. Yang, and Z. L. Wang, "Single-crystal nanorings formed by epitaxial self-coiling of polar nanobelts," *Science*, vol. 303, no. 5662, pp. 1348-1351, 2004.

[49]B. A. Korgel, "Self-assembled nanocoils," *Science*, vol. 303, no. 5662, pp. 1308-1309, 2004.

[50]Z. L. Wang, X. Kong, and J. Zuo, "Induced growth of asymmetric nanocantilever arrays on polar surfaces," *Physical Review Letters*, vol. 91, no. 18, p. 185502, 2003.

[51]Z. L. Wang, "Novel nanostructures and nanodevices of ZnO." Elsevier, 2006, pp. 339-370.

[52]Z. L. Wang, "Zinc oxide nanostructures: growth, properties and applications," *J. Phys.: Condens. Matter*, vol. 16, no. 25, p. R829, 2004.

[53]H. Kumomi and T. Yonehara, "Coarsening phenomenon of Si clusters on artificial nucleation sites," *Appl. Phys. Lett.*, vol. 54, no. 26, pp. 2648-2650, 1989.

[54]H. Kumomi, T. Yonehara, Y. Nishigaki, and N. Sato, "Selective nucleation based epitaxy (SENTAXY): investigation of initial nucleation stages," *Appl. Surf. Sci.*, vol. 41, pp. 638-642, 1990.

[55]H. Kumomi and T. Yonehara, "Coarsening phenomenon of Si clusters," *Mater. Res. Soc. Symp. Proc.*, vol. 202, 1990.

[56]J. D. Jackson, "Classical electrodynamics," 2007.

[57]J. Lekner, "Electrostatics of two charged conducting spheres," *Proc. Math. Phys. Eng. Sci.*, vol. 468, no. 2145, pp. 2829-2848, 2012.

[58]J. N. Reddy, *Introduction to the finite element method*. McGraw-Hill Education, 2019.

[59]P. K. Jha, V. Kuzovkov, B. A. Grzybowski, and M. O. De La Cruz, "Dynamic self-assembly of photo-switchable

nanoparticles," *Soft Matter*, vol. 8, no. 1, pp. 227–234, 2012.

[60]R. J. Glauber, "Time–dependent statistics of the Ising model," *J. Math. Phys.*, vol. 4, no. 2, pp. 294–307, 1963.

[61]J. C. Maxwell, *A treatise on electricity and magnetism*. Oxford: Clarendon Press, 1873, vol. 1.

[62]K. Kolikov, D. Ivanov, G. Krastev, Y. Epitropov, and S. Bozhkov, "Electrostatic interaction between two conducting spheres," *Journal of Electrostatics*, vol. 70, no. 1, pp. 91–96, 2012.

[63]P. T. Metzger and J. E. Lane, "Electric potential due to a system of conducting spheres," *arXiv preprint arXiv:0906.1617*, 2009.

[64]COMSOL Multiphysics® v. 5.3., "AC/DC Module User's Guide," 2017.

[65]R. Zhang, P. K. Jha, and M. O. De La Cruz, "Non–equilibrium ionic assemblies of oppositely charged nanoparticles," *Soft Matter*, vol. 9, no. 20, pp. 5042–5051, 2013.

[66]N. Metropolis, A. W. Rosenbluth, M. N. Rosenbluth, A. H. Teller, and E. Teller, "Equation of state calculations by fast computing machines," *J. Chem. Phys.*, vol. 21, no. 6, pp. 1087–1092, 1953.

[67]*MATLAB version 9.11.0.1809720 (R2021b) Update 1*, The Mathworks, Inc., Natick, Massachusetts, 2021.

[68]F. Pedregosa, G. Varoquaux, A. Gramfort, V. Michel, B. Thirion, O. Grisel, M. Blondel, P. Prettenhofer, R. Weiss, V. Dubourg *et al.*, "Scikit–learn: Machine learning in python," *the Journal of machine Learning research*, vol. 12, pp. 2825–2830, 2011.

[69]W. B. Russel, W. Russel, D. A. Saville, and W. R. Schowalter, *Colloidal dispersions*. Cambridge university press, 1991.

[70]M. J. Assael, A. Kalyva, S. Monogenidou, M. L. Huber, R. A. Perkins, D. G. Friend, and E. F. May, "Reference values and reference correlations for the thermal conductivity and

viscosity of fluids," *Journal of physical and chemical reference data*, vol. 47, no. 2, p. 021501, 2018.

[71]J. Rumble, "CRC handbook of chemistry and physics. 102nd edition 2021-2022," 2021.

[72]T. J. Woehl and T. Prozorov, "The mechanisms for nanoparticle surface diffusion and chain self-assembly determined from real-time nanoscale kinetics in liquid," *The Journal of Physical Chemistry C*, vol. 119, no. 36, pp. 21 261-21 269, 2015.

[73]J. Lu, Z. Aabdin, N. D. Loh, D. Bhattacharya, and U. Mirsaidov, "Nanoparticle dynamics in a nanodroplet," *Nano letters*, vol. 14, no. 4, pp. 2111-2115, 2014.

[74]A. Verch, M. Pfaff, and N. de Jonge, "Exceptionally slow movement of gold nanoparticles at a solid/liquid interface investigated by scanning transmission electron microscopy," *Langmuir*, vol. 31, no. 25, pp. 6956-6964, 2015.

[75]H. Zheng, S. A. Claridge, A. M. Minor, A. P. Alivisatos, and U. Dahmen, "Nanocrystal diffusion in a liquid thin film observed by in situ transmission electron microscopy," *Nano letters*, vol. 9, no. 6, pp. 2460-2465, 2009.

[76]T. J. Woehl, C. Park, J. E. Evans, I. Arslan, W. D. Ristenpart, and N. D. Browning, "Direct observation of aggregative nanoparticle growth: Kinetic modeling of the size distribution and growth rate," *Nano letters*, vol. 14, no. 1, pp. 373-378, 2014.

[77]J. M. Yuk, J. Park, P. Ercius, K. Kim, D. J. Hellebusch, M. F. Crommie, J. Y. Lee, A. Zettl, and A. P. Alivisatos, "High-resolution EM of colloidal nanocrystal growth using graphene liquid cells," *Science*, vol. 336, no. 6077, pp. 61-64, 2012.

[78]N.-S. Cheng, "Formula for the viscosity of a glycerol-water mixture," *Industrial & engineering chemistry research*, vol. 47, no. 9, pp. 3285-3288, 2008.

[79]C. A. Schneider, W. S. Rasband, and K. W. Eliceiri, "NIH image to ImageJ: 25 years of image analysis," *Nat. Methods*, vol. 9, no. 7, pp. 671-675, 2012.

[80]N. M. Hwang, "Deposition and simultaneous etching of Si in the chemical vapor deposition (CVD) process: approach by the charged cluster model," *J. Cryst. Growth*, vol. 205, no. 1–2, pp. 59–63, 1999.

[81]K. Singh, A. Raghav, P. K. Jha, and S. Satapathi, "Effect of size and charge asymmetry on aggregation kinetics of oppositely charged nanoparticles," *Sci. Rep.*, vol. 9, no. 1, pp. 1–8, 2019.

[82]W. S. Cheong, D. Y. Yoon, D.-Y. Kim, and N. M. Hwang, "Effect of substrates on morphological evolution of a film in the silicon CVD process: approach by charged cluster model," *Journal of crystal growth*, vol. 218, no. 1, pp. 27–32, 2000.

[83]T. T. Kodas and M. J. Hampden-Smith, *The chemistry of metal CVD*. John Wiley & Sons, 2008.

[84]M. J. Hampden-Smith and T. T. Kodas, "Chemical vapor deposition of metals: Part 1. an overview of CVD processes," *Chemical Vapor Deposition*, vol. 1, no. 1, pp. 8–23, 1995.

[85]M. J. Hampden-Smith and T. T. Kodas, "Chemical vapor deposition of metals: Part 2. overview of selective CVD of metals," *Chemical Vapor Deposition*, vol. 1, no. 2, pp. 39–48, 1995.

[86]J. Fitch, D. Denning, and D. Beard, "The pattern dependence of selectivity in low pressure selective epitaxial silicon growth," *Journal of electronic materials*, vol. 21, pp. 455–462, 1992.

[87]J. Fitch, "Selectivity mechanisms in low pressure selective epitaxial silicon growth," *Journal of The Electrochemical Society*, vol. 141, no. 4, p. 1046, 1994.

[88]M. Goulding, "The selective epitaxial growth of silicon," *Materials Science and Engineering: B*, vol. 17, no. 1–3, pp. 47–67, 1993.

[89]H. K. H. Kumomi and T. Y. T. Yonehara, "Selective nucleation-based epitaxy (SENTAXY): A novel approach for thin film formation," *Japanese journal of applied physics*, vol. 36, no. 3S, p. 1383, 1997.

[90]J. M. Crowley, "Simple expressions for force and capacitance for a conductive sphere near a conductive wall," in *Proceedings of the ESA Annual Meeting on Electrostatics*, 2008, pp. 17–19.

[91]N. T. Thanh, N. Maclean, and S. Mahiddine, "Mechanisms of nucleation and growth of nanoparticles in solution," *Chemical reviews*, vol. 114, no. 15, pp. 7610–7630, 2014.

[92]D. V. Talapin, A. L. Rogach, M. Haase, and H. Weller, "Evolution of an ensemble of nanoparticles in a colloidal solution: theoretical study," *The Journal of Physical Chemistry B*, vol. 105, no. 49, pp. 12 278–12 285, 2001.

[93]R. Jaccodine, "Surface energy of germanium and silicon," *Journal of the electrochemical society*, vol. 110, no. 6, p. 524, 1963.

[94]K. Fujii, M. Tanaka, Y. Nezu, K. Nakayama, H. Fujimoto, P. De Bie vre, and S. Valkiers, "Determination of the Avogadro constant by accurate measurement of the molar volume of a silicon crystal," *Metrologia*, vol. 36, no. 5, p. 455, 1999.

[95]N. M. Hwang, W. S. Cheong, D. Y. Yoon, and D.–Y. Kim, "Growth of silicon nanowires by chemical vapor deposition: approach by charged cluster model," *Journal of crystal growth*, vol. 218, no. 1, pp. 33–39, 2000.

[96]S. Lee, N. Wang, and C. Lee, "Semiconductor nanowires: synthesis, structure and properties," *Materials Science and Engineering: A*, vol. 286, no. 1, pp. 16–23, 2000.

[97]W.–S. Shi, H.–Y. Peng, Y.–F. Zheng, N. Wang, N.–G. Shang, Z.–W. Pan, C.–S. Lee, and S.–T. Lee, "Synthesis of large areas of highly oriented, very long silicon nanowires," *Advanced Materials*, vol. 12, no. 18, pp. 1343–1345, 2000.

[98]S. Jin, Q. Li, and C. Lee, "Direct growth of amorphous silicon oxide nanowires and crystalline silicon nanowires from silicon wafer," *physica status solidi (a)*, vol. 188, no. 2, pp. R1–R2, 2001.

[99]S. Feng, D. Yu, H. Zhang, Z. Bai, and Y. Ding, "The growth mechanism of silicon nanowires and their quantum confinement effect," *Journal of Crystal Growth*, vol. 209, no. 2–3, pp. 513–517, 2000.

Abstract in Korean

하전된 나노입자로 이루어진 비고전적 결정성장 계의 역학을 연구하기 위해 하전된 나노입자 간의 정전기적 퍼텐셜 에너지를 계산하고, 계산된 에너지를 바탕으로 kinetic Monte Carlo (kMC) 시뮬레이션을 수행하였다. 퍼텐셜 에너지 계산을 위한 방법으로 수치 계산법과 해석적 방법이 모두 사용되었다. 수치 계산은 유한요소법 (FEM) 을, 해석적 방법은 도체 계의 정전 용량 계수를 사용하였다.

첫번째로, 실리콘의 화학 증착법 (CVD) 과정 중 생긴 현상 중, 큰 입자 주위에 입자가 전혀 관찰되지 않는 입자 고갈 영역이 생기는 현상에 대해 연구하였다. 에너지 계산결과로부터 큰 입자와 작은 입자가 같은 부호의 하전을 가진채로 서로 근접해 있으면 인접한 표면에 생기는 반대 부호의 유도 전하로 인해 인력이 작용한다는 것이 확인되었다. kMC 시뮬레이션 결과로부터 이러한 인력으로 인해 큰 입자 주변에 상대적으로 작은 고갈 영역이 생기고, 이를 통해 큰 입자에 전하가 축적되는 것이 확인되었다. 축적된 전하는 작은 입자와 큰 입자 사이의 반발력을 형성하고 이로 인해 입자 고갈 영역이 점진적으로 확장되었다. 양으로 하전된 나노입자와 음으로 하전된 나노입자의 개수 불균형이 입자 고갈 영역 형성에 영향을 미치는 것으로 확인되었다.

두번째로, 또 다른 특이한 미세구조 중 하나로써, 실리콘의 화학 증착법 중 실리콘 입자의 비정상적 성장 현상을 시뮬레이션을 통해

수치적으로 연구하였다. kMC 시뮬레이션 결과는 하전된 나노입자의 전하 부호가 균형을 이루는 조건에서 양과 음으로 하전된 나노입자 모두의 정전기적 인력으로 인해 증착 입자의 비정상적 성장이 발생함을 보여주었다. 증착 입자가 성장하는 동안 기상에 존재하는 입자의 충분한 개수 밀도 역시 비정상 성장에 중요한 요인인 것으로 밝혀졌다. 증착 과정 중 기체 유속 역시 증착 입자의 성장에 영향을 주는데, 빠른 기체 유속은 약간 불균형한 전하 부호에서도 비정상적 성장을 유도하는 결과를 보여주었다.

세번째로, 기판의 전기적 성질에 따라 증착 입자의 성장 거동과 속도를 연구하였다. 기판의 종류는 접지된 도체, 플로팅 도체, 그리고 절연체 세 가지 경우가 고려되었다. 하전된 나노입자의 부호가 균형을 이룰 때, 접지된 도체 기판에 비해 플로팅 도체 및 절연체 기판 위에서 성장속도가 가속되는 결과를 보여주었다. 하전된 나노입자의 부호가 불균형할 때는, 접지된 도체 기판위에서 장기적인 성장 속도는 가장 빨랐다. 플리팅 도체 및 절연체 기판 위에서는 성장이 어느정도 진행된 이후에, 전하 축적에 의해 성장이 제한되었다. 에칭 조건에서는, 증착된 입자가 전하 축적 후 기상의 입자와 반발하여 오히려 에칭되었다.

마지막으로, 유한요소법을 이용하여 하전된 나노입자와 하전된 나노와이어 계의 정전기 퍼텐셜 에너지를 계산하고, 이 에너지가 하전된 나노입자가 존재하는 계에서 어떻게 하전된 나노와이어의 비등방적 성장에 영향을 미치는지에 대해 연구하였다. 계산결과로부터 기상의 입자와 증착된 나노와이어가 같은 부호의 전하를 가지고 있을 때,

비등방적 성장에 유리한 것으로 나타났다. 이는 나노와이어의 팁 방향으로 접근하는 입자가 측면 방향으로 접근하는 입자보다 반발력이 약한 것에서 기인한다. 각 방향에서 입자가 나노와이어의 접근할 때 에너지 장벽 차이를 비교했을 때, 나노와이어가 짧을수록, 그리고 나노와이어와 입자의 전하량 비율이 클수록, 비등방적 성장에 유리하게 작용하는 경향이 나타났다. 정전기적 상호작용에 의해 하전된 나노와이어가 비등방적 성장을 하기 위해서는 하전된 나노입자의 전하 부호가 불균형해 동일한 부호를 가질 때의 정전기적 상호작용이 주로 존재해야 하는 것으로 나타났다.

종합적으로, 기상의 하전된 나노입자가 박막 성장의 기본 단위가 되는 비고전적 결정성장에서 박막의 미세구조를 결정하는데 가장 중요한 요인은 하전된 나노입자의 전하 부호 비율인 것으로 나타났다.